Solidification in laser powder deposition of Ti-Nb alloys

by

Vahid Fallah

A thesis

presented to the University of Waterloo

in fulfillment of the

thesis requirement for the degree of

Doctor of Philosophy

in

Mechanical Engineering

Waterloo, Ontario, Canada, 2011

Author's Declaration

I hereby declare that I am the sole author of this thesis. This is a true copy of the thesis, including any required final revisions, as accepted by my examiners.

I understand that my thesis may be made electronically available to the public.

Abstract

The size and morphology of the dendrite growth patterns are simulated for laser powder deposition of Ti-Nb alloys under steady-state and transient growth conditions. A phase field model using an adaptive grid technique was employed to simulate the steady-state growth of dendrites on rather small domains, in which fixed local solidification conditions are present. For simulation of dendrite growth patterns at transient conditions, a cellular automaton model was used along with a virtual front tracking technique on larger domains, containing various initial orientations of the solid-liquid (SL) interface. To obtain the required input thermal data, i.e., the temporal distribution of temperature, a finite element analysis was performed along with a novel numerical approach for the real-time addition of new deposition material in each time step, thus building the deposition geometry momentarily. Using the output of the thermal model, the motion and morphology of the SL interface was determined through tracking the isotherm of the solidification temperature.

First, in this study, the appropriate set of processing parameters was found through an optimization process using a new concept, laser supplied energy E_s, which combines the effects of the energy and powder density in the process. With the developed analytical/experimental procedure, crack and pore-free coatings of Ti-Nb with continuous beads were produced by examining the effects of a few sets of processing parameters, including laser power, laser scan velocity, laser beam diameter and powder feed rate. The results of the thermal model for the optimized set of parameters matched with the thermocouple temperature measurements with only ~5% deviation. The thermal model was able to predict realistic profiles for the temporal development of deposition geometry, thus predicting meaningful morphologies of the SL interface. The model output was easily treated for extraction of local processing parameters, such as the temperature gradient and solidification velocity. These data are very useful when simulating the dendrite growth patterns at steady-state conditions in directional solidification of selected regions in the microstructure. In order to define transient growth conditions, the simulated distribution of temperature can be also directly fed into the microstructure model at each solution time step.

Phase field simulations of steady-state growth of dendrites during directional solidification showed a remarkable agreement with the experimental observations for the local dendrite arm spacing across the microstructure. Also qualitatively agreeing with the experiment, the simulated dendrite spacing exhibited a minimum around the mid-height region of the microstructure, which is explained by the counter effect of the temperature gradient and solidification velocity along the height of the sample. On a large domain containing different initial orientations of the SL interface, cellular automaton simulations for transient growth patterns of dendrites could reproduce most qualitative features observed in the microstructure. The dendrite arm spacing gradually decreased from the top of the microstructure. The competition was won by the dendrites growing in areas with higher cooling rates, i.e., in the regions closer to the top of the microstructure. The secondary arms of the primary dendrites, which are initially inclined on the vertical axis, grew extensively only along the overall growth direction and eventually became primary arms in some cases.

Keywords: Solidification; Finite Element Method; Phase Field Modeling; Dendrite Growth; Laser Powder Deposition.

Acknowledgements

I would like to acknowledge the financial support from the Natural Sciences and Engineering Research Council of Canada (NSERC), Ministry of Research and Innovation (MRI) and Industrial Tooling Solutions (ITS).

I'm grateful to my advisors, professors Amir Khajepour and Stephen Corbin, who encouraged me during the research. The project would not have been done without their knowledge, tolerance and insight.

I'm indebted to professor Nikolas Provatas and his research group in McMaster university for providing me their valuable knowledge of the phase field modelling, access to their numerical codes and powerful processors.

Table of Contents

List of figures

List of tables

Nomenclature

t	Time, s
T	Temperature, K
c	Composition, wt.%
λ_1	Primary dendrite arm spacing, m
ΔT_0	Alloy freezing range, K
V_s	Solidification velocity, m s^{-1}
G	Temperature gradient, K m^{-1}
P_L	Laser power, W
V	Laser scan speed, m s^{-1}
D	Laser beam diameter, m
F	Powder feed rate, g s^{-1}
E	Laser specific energy, J m^{-2}
ψ	Powder density, g m^{-2}
E_s	Laser supplied energy, J
H_c	Clad height, m
S	Surface tension number
γ	Surface tension, J m^{-2}
q	Laser absorbed power density, W m^{-2}
μ_l	Melt-pool viscosity, g s^{-1} m^{-1}
k_t	Thermal conductivity, W m^{-1} k^{-1}
c_p	Specific heat capacity, J g^{-1} K^{-1}
Q_l	Generated power, W m^{-3}
ρ	Density, g m^{-3}
T_0	Ambient temperature, K
T_m	Melting temperature, K
ε_R	Emissivity
h	Heat convection coefficient, W m^{-2} k^{-1}
σ_R	Stefan-Boltzman constant, W m^{-2} k^{-4}
β	Absorption factor
I	Laser power intensity, W m^{-2}
r_L	Laser beam radius, m
$t_\mathrm{activation}$	the time of addition of deposited material into the system, s
L_f	Latent heat of fusion, J m^{-3}
c_p^*	Modified specific heat capacity, J g^{-1} K^{-1}
C	Powder catchment efficiency

$S_{\mathrm{powder}}^{\mathrm{melt}}$	Intersectional area of the melt pool and powder stream, m^2
n_l	Number of layers of elements to be activated in each time-step
Δh	Deposition height in each time-step, m
l_{el}	Element side length, m
Δt	Solution time step, s
R	Dendrite tip radius, m
G_c	The solute concentration gradient in the liquid at the dendrite tip, wt.% m^{-1}
Γ	Gibbs-Thomson parameter, K m
m_l	Liquidus slope, K/wt.%
D_l	Diffusion coefficient in the liquid, m^2 s^{-1}
D_s	Diffusion coefficient in the solid, m^2 s^{-1}
C_l^*	Solute concentration in the liquid at the dendrite tip, wt.%
θ	The angle of interface normal and the laser scanning direction, deg
φ	The angle of interface normal and the dendrite axis, deg
c_0	Alloy bulk chemical composition, wt.%
D_0	Proportionality constant for diffusion in liquid alloy, m^2 s^{-1}
Q	Activation energy of solute diffusion in liquid alloy, cal $mole^{-1}$
R_g	Gas constant, cal $mole^{-1}$ K^{-1}
k	Equilibrium partition coefficient
$D_{\mathrm{BB}}^{\mathrm{l}}$	Self-diffusion coefficient of the solvent B, m^2 s^{-1}
d_{B}	Atomic diameter of the solvent B, m
d_{A}	Atomic diameter of the solute A, m
D_0^{BB}	Proportionality constant of the liquid solvent B, m^2 s^{-1}
Q^{l}	Self diffusion activation energy of solute B, cal $mole^{-1}$
k_0	Atomic valence
$E_1(P)$	The exponential integral function
λ_{s}	The wavelength of the solid/liquid interface, m
P	Peclet number
P_c	Solutal peclet number
P_t	Thermal peclet number
$\mathrm{Iv}(P)$	Ivantsov's function
Ω	Supersaturation in the liquid ahead of the solid/liquid interface
T_{t}	The dendrite tip temperature, K
ΔT	Total undercooling at the dendrite tip, K
ΔT_{c}	Solutal undercooling, K
ΔT_R	Curvature undercooling, K

ΔT_{k}	Kinetic undercooling, K
ΔT_{t}	Thermal undercooling, K
α	Thermal diffusivity, $\mathrm{m}^2\ \mathrm{s}^{-1}$
$c_{\mathrm{l}}[z]$	The liquid composition profile at the dendrite tip, wt.%
$T[z]$	The equilibrium melting temperature at the dendrite tip, K
$T_{\mathrm{q}}[z]$	The local liquid temperature at the dendrite tip, K
$\Delta T[z]$	The local undercooling ahead of the dendrite tip, K
z	The axis along the dendrite arm, m
R_e	Size of equiaxed grains, m
$\emptyset_e$	The extended volume of equiaxed grains, m^3
$\emptyset$	The actual volume of equiaxed grains, m^3
$V_{\mathrm{e}}[z]$	Growth velocity of equiaxed grains, $\mathrm{m\ s}^{-1}$
z_n	Location of nucleation undercooling in the liquid ahead of dendrite tip, m
N_0	Density of heterogeneous nucleation sites for equiaxed grains, m^{-3}
ΔT_{n}	Nucleation undercooling, K
a_0	Inter-atomic distance, m
$\phi(\vec{x})$	Solid-liquid order parameter field
ΔF	The complete energy functional of a dilute binary alloy, J
H	Nucleation barrier, $\mathrm{J\ m}^{-3}$
W_ϕ	Length scale of solid-liquid boundary, or interface width, m
W_c	Length scale of compositional boundary, m
$f(\phi, c, T)$	Bulk free energy density of the alloy, $\mathrm{J\ m}^{-3}$
$g(\phi)$	Interpolation function for nucleation barrier
Ω_{v}	Molar volume of the alloy, $\mathrm{m}^3\ \mathrm{mole}^{-1}$
s_L	Entropy of liquid, $\mathrm{J\ K}^{-1}\ \mathrm{m}^{-3}$
ϵ_L	Internal energy of the liquid, $\mathrm{J\ m}^{-3}$
ϵ_S	Internal energy of the solid, $\mathrm{J\ m}^{-3}$
$f^A(T_m)$	Free energy of species A, $\mathrm{J\ m}^{-3}$
$\bar{f}_{AB}^{mix}(\phi, c, T)$	Mixing energy of A and B elements, $\mathrm{J\ m}^{-3}$
M	Mobility constant related to the atomic rearrangement
τ	Time scale related to the atomic rearrangement from disordered to ordered, s
$\eta(\vec{x}, t)$	A stochastic noise term
$A(\theta)$	A function representing the anisotropy of interface width and time scale
ϵ_4	Four-fold anisotropy amplitude
l_T	Thermal length of the alloy, m
V_p	Pulling velocity in a directional solidification field, $\mathrm{m\ s}^{-1}$

d_0	Solutal capillary length, m
κ	Curvature, m^{-1}
μ_k	Atomic mobility at the interface
$\hat{\lambda}$	Inverse nucleation barrier
$\Delta\bar{x}$	Dimensionless grid size
$\Delta\bar{t}$	Dimensionless time step
$\phi_{initial}$	Initial order parameter field
$\widetilde{U}$	Supersaturation in the liquid
$\bar{c}$	Dimensionless concentration
$\bar{c}_{initial}$	Initial dimensionless concentration field
$\bar{t}$	Dimensionless time
SL interface	Solid/Liquid interface
σ^*	Stability parameter
T_l^{eq}	Equilibrium liquidus temperature at the initial composition, K
c_l^*	Liquid composition at the dendrite tip, K
c_s^*	Solid composition at the dendrite tip, K
$f(\varphi, \theta)$	A function for anisotropy of the surface tension
ε	Amplitude of the anisotropy of the surface tension
V_n	Interface normal velocity, m s^{-1}
$\vec{\mathbf{n}}$	Interface normal vector
t_{total}	Total solidification time, s
nt	Number of iterations for the numerical schemes
Π	Potential parameter for a uniform composition field, wt.%
a	Grid size in uniform square mesh, m
$\bar{\kappa}$	Mean interface curvature
$\Delta\vec{T}$	Variation of unit tangent vector
$\vec{T}$	Unit tangent vector
Δs	Variation along a curve
$\mathrm{D}_{\vec{T}}$	Directional derivative of the tangent vector
f_s	Fraction of solid
f_l	Fraction of liquid
c_l	Composition of liquid
c_s	Composition of solid
Δf_s	Solid fraction increment in on time step
η	Noise amplitude for the solid fraction

Chapter 1:

Introduction

Modelling of solidification microstructures in laser powder deposition requires the understanding of different aspects of the physical phenomena occurring during the process, which are affected by both the processing and material parameters. The controlling parameters of the process, such as the laser power, laser scan speed and laser beam diameter determine the transient thermal state of the system for a given set of powder and substrate materials. The resultant temporal distribution of temperature in the system sets the boundary conditions of solute diffusion, which in turn controls the growth patterns of microstructural features. This is practically valid since the rate of heat diffusion in the metal alloy systems is normally several orders of magnitude larger than that of the solute diffusion [1, 2]. On the other hand, the macroscopic quality of the deposited materials is also highly influenced by the processing parameters. In this study, the experimental design of laser powder deposition of Ti-Nb alloys is first investigated for best macroscopic quality, such as visually sound deposition (i.e., pore and crack-free coatings). A finite element thermal model is developed along with an explicit numerical scheme to describe the evolving geometry of the deposited material, incorporating the real-time addition of material into the simulation domain. The transient distribution of temperature obtained from the thermal model is explicitly used as the initial and boundary conditions in each simulation time-step for a microstructure model. The directional growth patterns of dendrites at steady-state conditions are simulated for local processing conditions obtained from the thermal model. For this purpose, the evolution of dendrite arrays are modelled using the phase field (PF) method for rather small simulation domains, within which the assumption of fixed solidification conditions holds valid. A cellular automaton (CA) technique integrated with a virtual front tracking method is employed for simulation of dendrite growth patterns at transient conditions on larger domains, for a variety of initial growth orientations.

Presented below is a detailed literature review of experimental and numerical investigations on different physical aspects of the laser powder deposition process.

1.1 Laser powder deposition (LPD)

Laser powder deposition (LPD) is a cost-effective and near-net shape rapid prototyping process to directly manufacture fully-dense and complex 3D components. The cost-effectiveness of such processes becomes highly important when dealing with high-cost materials such as Ti alloys, and also hard materials for which post-machining is difficult. So far, several LPD processes have been commercialized, including directed-light fabrication (DLF) [3], laser additive manufacturing (LAM or Lasform) [4] and laser-engineered net shaping (LENS) [5]. This technique is widely used for deposition of thin protective layers of novel alloy materials on components operating in severe conditions [6-8] and also for fabrication and repair of complex 3D parts [9, 10]. The general machining techniques and the related computer-aided design requirements have become well-established during the development of these processes. However, the microstructural development and the effect of the metallurgical factors in laser deposition processes requires further study for a wider range of alloy systems and processing conditions.

1.2 Ti-Nb powder deposition

Titanium and its alloys are proper choices for many components in aerospace and, more recently, in biomedical applications. However, the final components made of these alloys can be very expensive due to the high cost of the raw materials, processing and machining difficulties combined with high buy-to-fly ratios, that exceed 20:1 [4, 11].

Using powder deposition techniques to fabricate Ti-based parts, not only the final production cost and time but also the material usage can be significantly reduced. These benefits become extremely important when making components for biomedical applications such as orthopedic and trauma surgery, where prostheses must be individually shaped [12]. Though Ti-6Al-4V and TiNi alloys are widely used as surgical implant materials, studies have shown that the release of Al, V and Ni ions from these alloys inside the human body might cause long term health problems [13]. Ti-Nb alloys have been recently investigated to substitute for TiNi and Ti-6Al-4V in many biomedical applications due to their similar mechanical properties and better corrosion behaviour in human body environments [13-15]. However, since Ti-Nb alloys are more expensive than the other two alloys, a complete replacement may not be the best solution where only a modification of the surface composition is required. One approach to improve the biocompatibility of Ti-6Al-4V parts is the modification of the surface chemical composition by substituting Nb for Al and V, while realizing the benefits of the relatively lower cost Ti-6Al-4V as the bulk material.

To date, laser deposition of Ti-based powders or wires has been studied by several investigators [4, 11, 12, 15-17]. However, most of these studies have focused on the experimentally-based process optimization, microstructure evolution and mechanical properties of laser-formed products of only Ti-6Al-4V. Laser powder deposition of Ti-Nb alloys was first successfully investigated by Fallah et al. [6] to create a protective layer on the surface of mild steel samples. They found a strictly narrow range of processing parameters within which the formation of brittle intermetallics at the substrate-clad interface can be prevented. Due to the complexity of solid-state phase transformations in the Ti-Nb-Fe system, process optimization and simulation of microstructural development in this study are performed only for the laser powder deposition of Ti-Nb alloys on Ti-6Al-4V alloy where the clad material is composed of only Ti and Nb.

1.3 Thermal modelling

In laser powder deposition (LPD), solidification and solid state transformations upon heating and cooling deeply affect the final properties of the deposited materials. However, control of the physical phenomena involved is extremely difficult and sometimes impossible exclusively by means of experimental analyses. To help with the process optimization, several research groups have adopted numerical methods to monitor the process output along with the experimental investigations [9, 18-23].

One of the most challenging problems in simulation of the LPD process is the dynamic incorporation of the additive material into the numerical algorithm. An innovative approach recently used by a number of investigators [9, 18-21] involves deposition of additive material through activation of a new set of elements in each time step of the finite element solution. In most of these investigations [9, 18-20], the deposited tracks are considered with a pre-defined rectangular shape. The height and width of these structures are analytically determined from the process parameters, such as the powder feed rate and laser scan velocity. Peyre et al [21] used a numerical approach to estimate the final clad width for each individual layer within a layered structure. They developed a steady state finite element simulation of laser irradiation on a flat surface to numerically determine the melt pool width. This was followed by an analytical calculation of the average clad height over the cells within the estimated melt pool boundaries. Apart from the simplifications made by assuming the final clad shape in all aforementioned models, the simulation domains were discretized with coarse mesh sizes and led to poor estimations of the geometry of the melt-pool during the deposition process.

In an attempt to predict the deposition geometry without assuming a particular shape, Alimardani et al [22] developed a decoupled approach in which the heat transfer governing equations were solved separately for the substrate and clad materials. With this method, although using a decoupled scheme, the authors have shown good agreement between the predicted and measured final clad geometry and temperature distributions. In another novel approach introduced by Qi et al [23], the geometrical development of the single-track depositions was simulated through tracking the liquid/gas free surface during the process. The transport equations were solved for the temperature and fluid velocity using a control volume finite difference method in a coupled manner. This model is able to predict the instantaneous morphology of the melt free surface with an inclined geometry, thus providing a more realistic simulation of the geometrical characteristics of the final clad structure. However, the level-set function defined for tracking the liquid free surface was solved with an explicit finite difference scheme which imposes serious limitations on the maximum time increment in each solution step. Considering also the massive calculations required for the solution of transport equations for both the temperature and fluid velocity, the overall simulation time may be extremely long for finely meshed 3D structures.

Despite all the contributions and valuable results of these previous models, their application is strictly limited when predicting the geometrical and morphological development of the melt-pool during the process. Simplifying assumptions made for the final clad shape and geometry lead to formation of unrealistically flat melt surface morphologies and introduce a significant computational error in applying the heat input boundary conditions underneath the moving laser beam [23]. The accumulation of errors over the solution process results in considerable deviations in the predicted temperature distributions and geometrical features of the melt-pool from the experimental observations. Moreover, the microstructural development in LPD depends upon the local solidification conditions within the melt-pool, such as the temperature gradient and solidification velocity [24]. Fine mesh sizes are required within the melt pool zone for precise extraction of these variables along the estimated solid/liquid interface. The required massive computational load seriously limits the applicable overall size of the model and the minimum allowable time increment for the solution procedure.

So far, very little attention has been given to the precise estimation of the geometrical development of the melt pool during the laser material deposition process. In this study, the thermal distribution in LPD process is modelled in a rather simple but realistic 3D fashion which allows reasonably fine discretization of the solution domain.

1.4 Microstructure modelling

Ti-Nb alloys under laser powder deposition conditions are solidified under high thermal gradients and high velocities, which produces a complex array of columnar dendrites where microsegregation of the alloying element occurs. The segregation pattern can be characterized by primary dendrites parallel to and secondary dendrites perpendicular to the <100> directions closest to the macroscopic solidification direction, i.e., the direction opposite to that of heat extraction. It is shown that these features have significant effects on the mechanical properties of the solidified structures [1, 25]. Also, in the case of directionally solidified alloys, the extent of microsegregation can greatly influence the subsequent thermo-mechanical and/or heat treatment processes [26]. To improve the properties of the solidified parts, not only the formation of solidification defects has to be controlled but also a fundamental knowledge of the growth of dendritic morphologies during solidification is required.

Over the past three decades or so, significant progress has been made in understanding dendritic growth from both experimental and theoretical studies. Many theoretical approaches have been developed to determine the morphology and calculate the size of dendrites. Initially, analytical models were proposed for the primary dendrite tip spacing which assumes the dendrites to be ideally spaced, i.e., considering only an averaged interaction between the dendrites [2, 27]. Most of the theoretical treatments give the following simple functional form for the primary dendrite arm spacing:

$$\lambda_1 = A \Delta {T_0}^{0.25} {V_\mathrm{s}}^{-0.25} G^{-0.5} \tag{1}$$

where G is the temperature gradient, V_s is the growth velocity, ΔT_0 is the freezing range of the alloy and A is a constant representing the thermophysical properties of the alloy. This function simply relates the processing variables and thermophysical properties of the alloy with the primary dendrite spacing. However, experimental studies have shown that under transient growth conditions, such as variable growth velocity and temperature gradient in space and time, the dendrite structure that develops depends on the effectiveness of different selection mechanisms including dendrite branching and competitive growth [28, 29]. During the growth of a dendritic array the solute fields of neighbouring dendrites interact since the solute is rejected by each growing dendrite. This feature establishes a small range of stable dendrite spacings while dendrite branching and overgrowth mechanisms are also active. Therefore, based on this concept, the above simple formula does not hold valid. To solve the problem, the earliest numerical models were proposed for the steady state and transient growth of a cellular/dendritic array in binary alloys capable of predicting the dendrite spacing and tip undercooling [30, 31]. These early models were developed based on a pre-defined shape of the dendrite tip, i.e., the parabolic of revolution taken from the analytical solutions, and also assuming ideally spaced primary dendrite arms. More recent models such as phase-field methods (PF) and cellular automaton (CA), however, do not assume the analytical solution for steady-state tip velocity of a parabolic shape, but develop the solution for an arbitrary geometry that evolves during the process. Therefore, the time dependency is incorporated in these solutions.

1.4.1 Latest methods

Two major methods, the cellular automaton (CA) [32-37] and phase field method (PF) [38-46], are capable of realistic simulation of micro-scale dendritic growth, reproducing most of the features observed experimentally thus transforming the computer into a dynamic microscope. Hereafter in this section, the general principles of these methods will be reviewed followed by an overall evaluation of their effectiveness for various applications and purposes.

1.4.1.1 *Phase field methods (PF)*

PF is an elegant and integrated simulation technique that solves two parabolic partial differential equations. One describes the concentration or temperature field and the other one governs the evolution of the order parameter field describing the type of phase present in the system, i.e., solid or liquid. The solution of the order parameter field is affected by the evolution of the solute or temperature field, depending on the process controlling the solidification, described by the second equation. The form of the phase field and conservation equations is derived from the principles of thermodynamics, i.e., using an entropy or energy formulation. The kinetics of dendritic growth is simulated in this technique. Since the shape of solid/liquid (SL) interface is determined through the phase field, no explicit tracking of interface is required. Therefore, PF models are readily able to handle the complex topological changes of dendritic growth in two or three dimensions.

PF simulations accurately reproduce the morphology and size of developing dendrites and capture most of the phenomena associated with dendrite formation (e.g. the equilibrium shape and kinetics of the dendrite tip, preferred growth direction, coarsening, coalescence, branching, etc.) [38, 41, 42, 47-49]. PF methods have been applied successfully to the solidification of pure metals [43, 44] and alloys [38, 45, 46, 48, 50], simulating very realistic dendritic growth patterns [46]. They have also quantitatively validated that the growth kinetics of the dendrite tip which agrees well with the results of microscopic solvability theory [43]. However, in this technique, the change of the phase field variable has to be spread over several mesh points during the numerical solution of equations. This transition layer has a finite thickness that separates the solid and liquid phases. Molecular dynamics studies show that this thickness should extend over only a few atomic dimensions [51]. Therefore, to capture the interface, this method normally requires very fine grids leading to high computational costs. Recently, Karma [52] and Echebarria et al [41] introduced a modification, so-called "antitrapping" solute current, in the phase field formulation. This phenomenological solute current counterbalances the physical, albeit artificially large, solute trapping effect generated when a mesoscopic interface thickness is used to simulate interface evolution on experimental length and time scales. This modification enables one to assume interface widths larger than values with a real physical meaning, thus allowing coarser mesh grids at low solidification rates. Moreover, the use of effective adaptive grid techniques [45, 49] has greatly improved the computational speed of PF simulations by several orders of magnitude. With this method, Greenwood et al. [53] simulated cellular and dendritic growth in directional solidification of dilute binary alloys. The simulated primary dendrite arm spacing as a function of pulling velocity for various thermal gradients and alloy compositions was found to agree well with the experimental observations.

1.4.1.2 *CA methods*

There are two main types of CA models developed for dendritic growth: those based on the analytical solution of dendrite growth and those based on the numerical solution of transport equations including the boundary conditions at the SL interface. The models based on the analytical solution of dendrite growth [34, 54] solves the heat and diffusion equations on a simulation domain and the corresponding values of composition and temperature at each mesh point are then used to calculate the local undercooling, which in turn determines a unique velocity of the SL interface based on the analytical model of steady-state dendrite tip growth [55]. A basic assumption of these models is that any point on the dendrite SL interface moves exactly along the same functional dependency as that of a steady-state tip. Moreover, in these models, the concept of marginal stability is used to uniquely define the dendrite tip radius. This way, the value of the stability parameter is determined to be around 0.02, which is constant only at steady-state and for an isotropic material [56, 57].

In the CA models based on the complete solution of the transport equations [32, 33, 35, 36], the solution involves the boundary conditions at the SL interface which defines the problem of dendritic growth, i.e., local equilibrium and conservation of heat/solute. They do not assume the analytical solution for the steady-state dendrite tip velocity of a parabolic shape, but an arbitrary geometry evolves during the process for which the solution for the interface velocity is developed. The time dependency is incorporated in this solution and the conservation equations are solved independently for each phase and then linked together by the partition coefficient at the interface. The most significant problem with the CA models is the artificial anisotropy introduced in the computations by the mesh of squared cells. In the early stages of the development of the CA technique, this anisotropy was used to simulate the preferential atomic attachment [33]. However, this artificial anisotropy became evident and problematic when models tried to simulate several grains or dendrites growing at different orientations on the same mesh. As the overall effect, the growth of dendrites was forced to align with the axes of the mesh, independently of the initial orientation or the corrections introduced in the SL surface tension for the preferential growth direction. Even for the dendrites growing along the axis, this anisotropy resulted in very elongated tips and meaningless kinetics [35]. Several attempts have been made To solve this problem including corrections to the growth direction [34, 54], adjustments to the increase of solid fraction [32] and virtual tracking of the SL interface [37, 58].

The most recent and reliable approach developed by Sanchez et al. [37] uses a virtual tracking method to capture new interface cells during solidification in a low peclet regime, i.e., at low growth rates. They claimed that with some other modifications made in the calculation of the interface curvature, growth velocity and the solid fraction increment, this approach nearly eliminates the artificial mesh anisotropy. However, from the results presented in their work [37, 58] and in another recent study based on the same method [59], it is observed that the dendrite growth is simulated only at very low solidification rates analogous to those of the conventional casting. So far, no proof has been presented that the artificial mesh anisotropy has been eliminated in simulations of microstructures developed under transient conditions with very high cooling rates typical of processes such as fast localized welding processes and laser powder deposition.

Moreover, the assumption of local solute conservation at the SL interface is actually equivalent to the concept of steady-state growth which is characterized by equilibrium diffusion of the rejected solute away from the SL interface. It, however, ignores the fact that during the initial unstable growth stage the rejected solute is greater than can be transported away from the SL interface by only diffusion. Therefore, at this stage, the condition of solute balance cannot be satisfied. In addition, when the dendrite tip has reached steady state growth, the rest of the SL interface positions behind the tip might undergo unstable growth, so that thermal or other statistical fluctuations can be amplified by the locally enriched solute perturbations leading to generation of side branching. Consequently, while the CA models based on the solute conservation at the SL interface are shown to be reasonably accurate in simulation of growth kinetics at steady-state, they do not accurately calculate growth velocity of all interface points when unstable growth occurs [58]. This problem can be signified when simulating dendrite growth at highly transient conditions such as those in high-speed laser powder deposition, where no steady-state growth can be realistically assumed at any stage of the solidification process.

1.4.1.3 *PF vs. CA*

So far, it can be concluded that the only advantage of the CA methods over the PF models is the lower computational cost required for qualitative-based analysis in the low peclet regime, i.e., at low solidification rates. If the CA models are required to be accurate and quantitative, CA techniques utilizing virtual front tracking have to be used on very fine grids, which may be even more computationally intensive than PF models [60, 61]. Moreover, none of the modifications made to remove the effect of artificial mesh anisotropy in CA models has been validated at high cooling rates typical of rapid and localized welding and laser powder deposition processes. Even if they do, the output of CA models can never be as accurate as those of the PF models. It should also be noted that the assumption of solute conservation at the SL interface in the CA models is not meaningful when the dendritic growth is not at steady-state. This has to be seriously considered when simulating solidification microstructures at highly transient conditions in welding and laser deposition processes.

1.4.2 Microstructure in deposition processes using concentrated heat sources

Several investigations [32, 62-65] have been done recently to simulate the dendrite morphologies developed in welding and powder deposition processes using highly concentrated heat sources. None of these studies have considered the extremely transient conditions [66] that exist in the solidifying melt during these processes. Instead, they assume fixed conditions, i.e., constant cooling rate, throughout the entire process and the simulation domain. Yin and Felicelli [63] used a simple and unrealistic thermal model based on a prescribed geometry for the deposited material in laser powder deposition in order to predict the temperature distribution and cooling rate within the molten pool. The results of this thermal model were then fed into the microstructure model developed based on a rather simple version of the CA method, already shown to exhibit artificial mesh anisotropy [35]. Moreover, no actual interface morphology is considered for the initial solid seed in the simulation domain but a rather simple layer solid on the simulation boundaries. Also, the final simulated dendrite morphologies are not qualitatively validated with the experimental observations. The same sort of simplifications have been made in the simulations of Zhan et al. for microstructures in a tungsten-inert-gas (TIG) welding process [64] leading to unrealistic overall patterns of dendrite morphologies. Tan et al. [65] developed a combined CA-PF method which uses PF simulations for calculation of only growth kinetics, and a basic CA technique, i.e., with simple capturing rules, to track the SL interface. This method is applied for a few constant local conditions in the laser welding process, producing arrays of dendrite arms typical of simple directional solidification.

So far, for deposition and welding processes using concentrated sources of heat, no comprehensive study has been done incorporating the temperature history obtained from a realistically designed thermal model. Moreover, the employed techniques for microstructure simulation have been used with many simplifications. They do not include the definition of real transient boundary conditions, the incorporation of transient thermal conditions, the actual morphology of the initial SL interface in the simulation domains, and the simplifying assumptions made in the CA techniques for tracking the SL interface. These assumptions have altogether led to the simulation of unrealistic dendrite growth patterns, lacking many qualitative features which could have been produced in truly competitive growth conditions and with physically meaningful numerical schemes for advancing the SL interface.

1.5 Summary

Ti-Nb alloys are new choices of material for many biomedical and aerospace applications [13-15]. Although an expensive material for some applications, they can be deposited in thin layers on different materials using a laser powder deposition technique. This helps to realise their novel properties while being used in small amounts in order to create protective layers on cheaper substrates. So far, laser powder deposition of Ti-Nb alloys has not been investigated experimentally nor numerically.

To date, the published numerical analyses of the transient thermal conditions in laser powder deposition [9, 18-21, 23, 67], or in any other kind of localized fast welding process with additive material, have not offered a realistic solution of the transient temperature distribution considering the temporal development of the deposited geometry during the process. Highly simplified assumptions, such as predefined rectangular shapes for the deposited material and decoupled solution of heat transfer equations for the deposited material and the substrate, have not allowed them to obtain generally accurate results or to predict a realistic melt-pool morphology. The later is significant when simulating the solidification microstructures using the local processing parameters, i.e., the solidification velocity and temperature gradient estimated from the thermal model. An accurately predicted melt-pool morphology is also a key feature to be utilized when considering transient growth conditions in microstructure simulation. One of the aims of the present study is to obtain the realistic melt-pool morphologies using an integrated thermal model capable of predicting the temporal temperature distribution, which will be also used in the microstructure model to simulate the dendrite growth patterns under transient conditions.

Very little attention has been given so far to model the directional solidification microstructures in the deposition processes using concentrated moving heat sources . All these studies [32, 62-65] have considered only local fixed processing conditions, i.e., constant temperature gradient and solidification velocity or only a constant cooling rate throughout the simulation time and space. The aforementioned solidification conditions are taken from very simple and generally unrealistic thermal models, such as those using simplifications described in the previous paragraph. Moreover, no dendrite growth patterns based on the transient thermal conditions have been developed. The microstructure modelling in this study will be performed based on the thermal conditions obtained using an integrated thermal model developed based on more realistic assumptions. This enables us to employ accurately predicted solid/liquid interface morphologies and also gives us the opportunity to build a numerical scheme for simulation of solidification morphologies under transient growth conditions.

Most of the recent studies on the simulation of solidification morphologies in deposition processes using concentrated heat sources have used basic versions of CA methods, i.e., without virtual tracking of the SL interface. CA methods are believed to be much faster than PF models, but also much less quantitatively reliable. However, it has been also reported that the speed will not be much different from PF models if CA methods are used with virtual front tracking on fine grid sizes. Thus, the results of past studies have been presented on a qualitative basis even for steady-state growth conditions. They would have been even more inaccurate for transient growth conditions. PF models are however reported to be reliable and accurate even for transient growth conditions. Amoorezaie et. al [49] and Gurevich et al. [68] studied the simulation of directional solidification microstructures in casting using a PF model. They have shown a remarkable agreement between the experimental observations and the PF model results under highly transient growth conditions in the areas near the mold wall. In the present study, an integrated PF model using an adaptive grid technique will be used to simulate both the steady-state and transient growth of dendrites. A CA method equipped with virtual front tracking will be also used for transient growth of dendrites on large simulation domains representing approximately the entire extent of the SL interface morphology during the process.

Chapter 2:

Ti-Nb deposition and experimental design

In this study, a high-quality optical beam of a fiber laser with minimal optical losses [69, 70] is used for the deposition of Ti-45wt.%Nb from the elemental blend of Ti and Nb powders on a Ti-6Al-4V substrate in order to produce a compositionally modified surface layer with improved biocompatibility. Furthermore, a process optimization procedure is carried out on the effect of combined parameters in laser processing on the macro- and micro-characteristics of the claddings.

2.1 Materials and apparatus

A 3 mm thick Ti-6Al-4V plate with a nominal composition of alloying elements of 6 wt.%Al and 4 wt.%V was used as the substrate. A premixed powder of 55 wt.% titanium and 45 wt.% niobium both with a particle size range of 5.6-44 μm was used for the deposition. The powders were received in oxygen-free storage containers from the manufacturers (i.e. H.C. Starck GmbH for Nb and Sulzer Metco Co. for Ti) and exposed to air only during mixing. The powder mixture was injected onto the substrate surface using a powder feeder (Sulzer Metco: 9MP-CL) equipped with a lateral nozzle at an angle of 55° with respect to the horizontal axis. Argon gas with a flow rate of 3×10^{-5} m^3/s was used as the conveying media for the powder mixture and also as the shielding gas for the deposition zone. A fiber laser manufactured by IPG Photonics Corporation with a nominal power of 1.1 kW was used to deposit the injected powder as illustrated in the schematic experimental design shown in Fig. 1. The laser head and the feeding nozzle are stationary while the substrate moves underneath them during the deposition process.

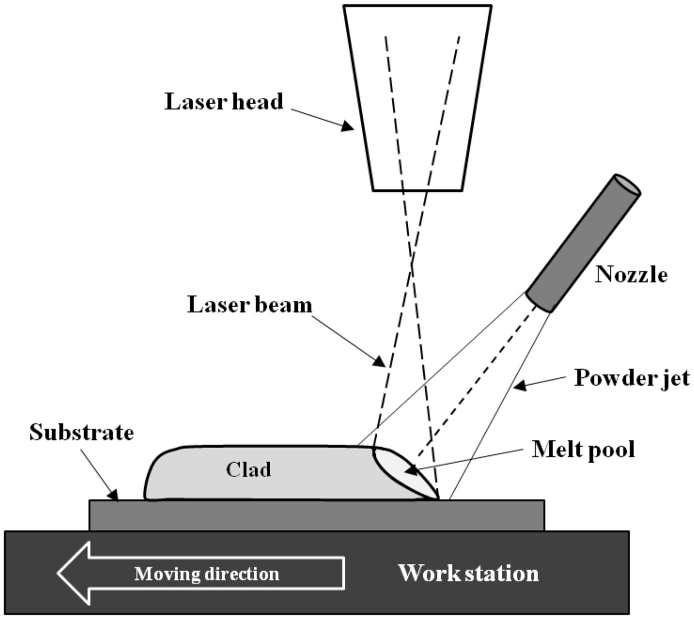

Fig. 1 Schematic of the experimental setup for the laser-assisted deposition.

Cross-sectional specimens were cut from the claddings for scanning electron microscopy and chemical composition measurements using a JEOL:JSM-6460 SEM microscope equipped with an Oxford Instruments INCA X-ray chemical analysis instrument. Prior to microscopy, the specimens were ground with SiC sandpaper up to 1200 mesh and polished with 1 µm and 0.3 µm alumina slurries.

2.2 Process design and evaluation

Controllable parameters in laser material processing include the laser power, laser scan speed, laser beam diameter and powder feed rate. All these parameters affect the clad quality and its geometrical characteristics, although not entirely independent of each other. For instance, an increase in the laser scan speed causes a reduction not only in the amount of supplied energy but also in the rate of feeding the powder onto the unit area of the substrate. Therefore, it may be difficult to investigate the effect of an individual parameter on the clad characteristics. Steen [71] proposed a combined parameter, laser specific energy, E (J/mm^2), to represent the provided energy density in the process:

$$E = P_{\mathrm{L}}/(VD) \qquad (2)$$

where P_{L} is the laser power (W), V is the laser scan speed (mm/s) and D is the laser beam diameter (mm). The product VD is representative of the effective area of the substrate in contact with both the laser beam and the powder stream during the process. Another important concept used by Wu et al. [72] and Zhou et al. [73] is the powder density ψ defined as the amount of powder fed to a unit area scanned by the laser beam.

$$\psi = F/(VD) \tag{3}$$

where F (g/s) is the powder feed rate.

It has been shown that the general clad quality and geometry are controlled by the combined parameters E and ψ [72, 73]. These two parameters may be dealt with differently in order to adjust each processing parameter for critically acceptable clad quality. Wu et al. [72] showed that in order to deposit claddings with predefined critical properties, threshold values of the combined parameters must be determined through interpolation. In this method, the laser specific energy and the powder density values are adjusted through interpolation of the laser power and the powder feed rate in order to reach the predetermined critical state of the claddings. Following this approach, Wu et al. [72] and Zhou et al. [73] showed that the critical values of laser specific energy and powder density are linearly related to each other. In other words, the corresponding diagram exhibits a constant slope with the dimension of J/g, indicating the amount of energy supplied per unit mass of the powder being fed hereafter called the laser supplied energy, E_s. A change in the laser power or the powder feed rate causes a change in the slope of the E-ψ diagram thereby altering the amount of E_s. However, it can be mathematically shown that a change in the laser scan speed or the beam diameter alone does not affect the slope of the E-ψ diagram. E_s should not be much below or above a definite value depending upon the type of the powder and the substrate material being used. This amount of energy is required to heat up, melt and metallurgically attach (i.e. by diffusion) the injected material to the substrate. The critical value of E_s defines a line in the E-ψ diagram through positions where critical values of the laser specific energy and the powder density were obtained by previous investigators [72, 73]. In this way, a more direct approach towards the critical $E - \psi$ relationship can be developed by changing only the laser power P_L or the powder feed rate F between different series of experiments (in each one of which the only variable is the laser scan speed, referring Table 1), in order to gradually increase the laser supplied energy up to the critical value.

The approach adopted in the current study is expected to provide an easier route to navigate through the individual processing parameters by adjusting the two combined parameters E and ψ. The concept of laser supplied energy is then employed to provide an estimation of the proper parameters and also to introduce an easier approach towards the critical values of the combined parameters. The parameter E_s (J/g) is defined as follows:

$$E_s = (P_L/F) \tag{4}$$

and also,

$$E = E_s \psi \tag{5}$$

Equation (4) indicates that the laser power and powder feed rate values determine E_s value thus manipulating the critical values of E and ψ and the general quality of the claddings. It also indicates that altering only the laser scan speed or the laser beam diameter does not affect the E_s value. In this study, therefore, process optimization is carried out by adjustment of the two individual processing parameters, P_L and F, within a predetermined laser scan speed range while setting a fixed laser beam diameter. The laser beam diameter is set to 2 mm which is slightly smaller than the applicable powder stream diameter. Different sets of applied processing parameters and the visual characteristics of the final claddings are listed in Table 1. For each of the series denoted as 'a' to 'd', nine experiments were done in spanning the range of laser scan speeds from 300 to 700 mm/min (equivalent to 5-11.67 mm/s) with 50 mm/min increments.

Table 1 Utilized processing parameters in laser cladding of the Ti-Nb powder mixture on the Ti-6Al-4V plate.

Series #	Laser power, P_L (W)	Powder feed rate, F (g/s)	Laser beam diameter, D (mm)	Laser scan speed, V (mm/s)	Laser specific energy, E (J/mm2)	Powder density, ψ (g/mm2)	Laser supplied energy, E_s (J/g)	Final clad visual characteristics
a	600	0.100	2	5-11.67	60-26	0.0100-0.0043	~6000	Almost no clad
b	900	0.100	2	5-11.67	90-39	0.0100-0.0043	~9000	Unmelted Nb + Macro-pores
c	1100	0.100	2	5-11.67	110-47	0.0100-0.0043	~11000	✓ Continuous bead
d	1100	0.133	2	5-11.67	110-47	0.0133-0.0057	~8300	Unmelted Nb + Macro-pores

2.2.1 Process results

The visual characteristics of the Ti-Nb claddings obtained using different sets of parameters are listed in Table 1. Using the 'a' series of parameters, no claddings were formed due to insufficient laser energy. In the 'b' series of parameters, in order to increase the E_s value, only the laser power was increased. This led to the formation of claddings which contained a considerable fraction of unmelted Nb particles on the surface and macroscopic pores. Raising the laser power to 1100 W in the 'c' series of experiments, eventually resulted in the formation of claddings that adhered to the substrate with continuous beads free of any visible unmelted particles and macro-porosity. Therefore, the corresponding E_s value of ~11000 J/g represents the critical amount of heat required for deposition of Ti-Nb elemental powder blend. The last set of claddings were made using the 'd' series of parameters chosen to represent an E_s value close to that of the ‘b’ series (i.e. by increasing both the laser power and the powder feed rate). Expectedly, as indicated in Table 1, the results were similar to those obtained during the ‘b’ series.

Table 2 Geometrical characteristics and chemical composition of Ti-Nb clad sections made by the ‘c’ series of parameters.

#	Clad height (mm)	Clad width (mm)	Clad bulk composition (wt.%)				Near surface composition (wt.%)				Clad dilution (wt.%)
			Nb	Al	V	Ti	Nb	Al	V	Ti	
c1	0.98	2.82	36.32	1.08	≤ 1	Balance	36.23	1.14	≤ 1	Balance	8.68
c2	0.89	2.87	32.80	1.42	≤ 1	Balance	32.92	1.40	≤ 1	Balance	12.20
c3	0.83	2.86	31.71	1.78	≤ 1	Balance	31.64	1.94	≤ 1	Balance	13.29
c4	0.65	2.84	31.03	1.90	≤ 1	Balance	31.46	2.14	≤ 1	Balance	13.97
c5	0.60	2.71	30.50	2.51	≤ 1	Balance	30.20	2.07	≤ 1	Balance	14.50
c6	0.51	2.78	29.27	2.27	≤ 1	Balance	29.06	2.40	≤ 1	Balance	15.78
c7	0.42	2.35	26.01	2.81	≤ 1	Balance	23.83	2.84	≤ 1	Balance	18.99
c8	0.38	2.45	23.96	3.06	≤ 1	Balance	23.33	3.47	≤ 1	Balance	21.04
c9	0.34	2.39	23.17	3.78	≤ 1	Balance	26.19	3.46	≤ 1	Balance	21.83

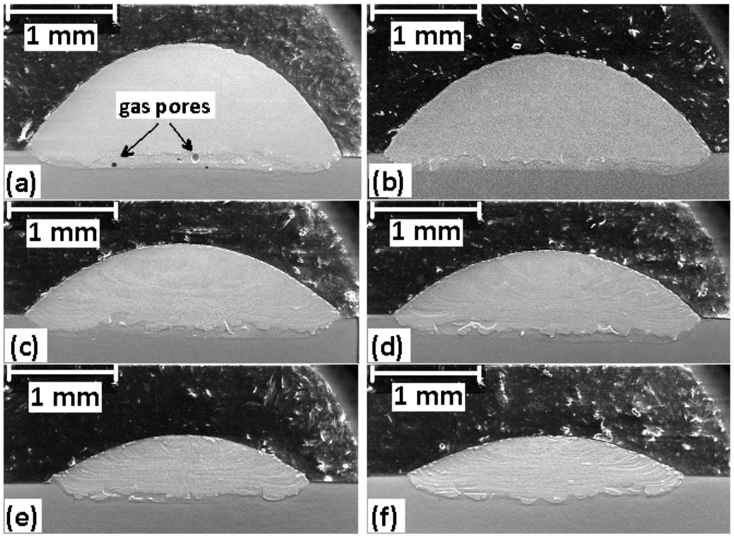

Fig.2 SEM images showing the cross-sectional view of selected claddings made by the ‘c’ series of parameters; a) *c1*, b) *c2*, c) *c4*, d) *c5*, e) *c7*, f) *c9* [74].

Fig.2 shows SEM images of the clad sections made by the ‘c’ series of parameters. Geometrical characteristics and chemical composition of these clad sections are given in Table 2. As can be seen in Fig.2(a), a few gas pores in sample ***c1*** appear in the form of dark round spots near the clad/substrate interface. The results indicate an increase in scan speed (i.e. from ***c1*** to ***c9***) raises the degree of dilution and decreases clad height.

2.2.2 Process optimization

Fig.3 shows how the clad visual soundness is correlated to the E_s value which is the slope of the E-ψ curves for each set of parameters. The proposed optimization procedure involves the alteration of only the laser power or the powder feed rate until the pre-defined critical state is reached. For example, for a given value of powder feed rate, a narrow range of laser power values can be found within which continuous beads are made at various scan speeds and beam diameters.

The gas porosity was observed only in sample ***c1*** which is most likely due to the entrapment of gas between the clad material and the substrate. They also found that the gas can be released more easily at higher laser scan speeds where the powder density is lower.

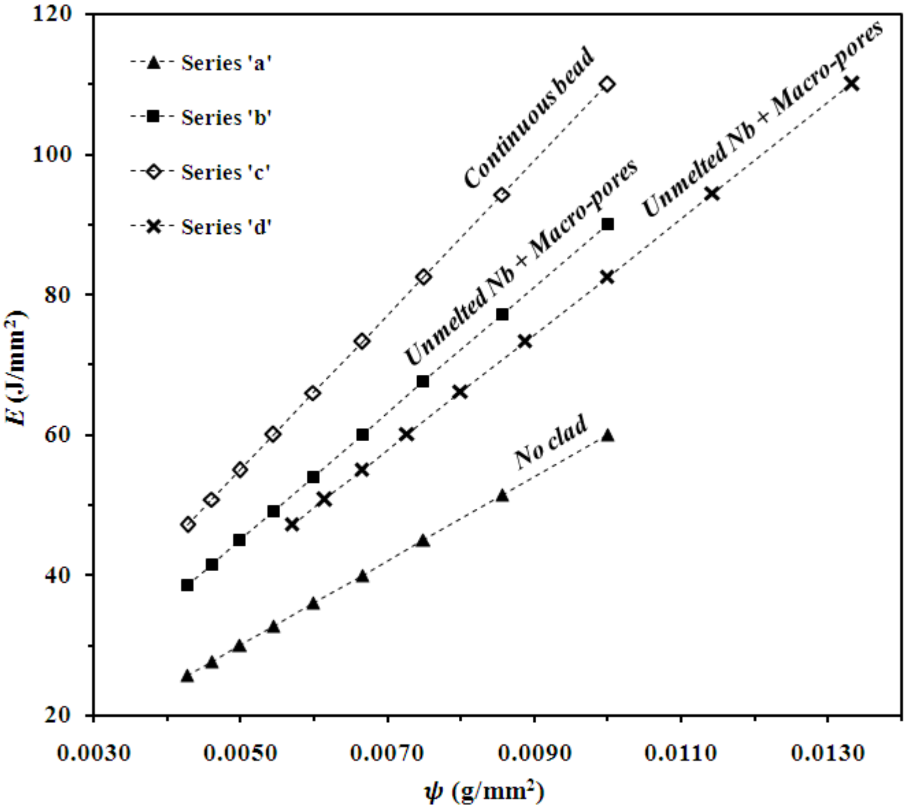

Fig.3 The E-ψ relationship for different sets of parameters [74].

The measured values of the clad width, given in Table 2, are close to but slightly greater than the laser beam diameter (i.e. ~2 mm). The clad height decreases, as shown in Fig.4, from sample ***c1*** to sample ***c9*** due to the reduction in the powder density. Also found by Wu et al. [72] and Zhou et al. [73], the clad height follows a rather linear relationship with the powder density. E-ψ relationship is approximated from Fig.4 for the Ti-Nb claddings, as below:

$$H = 120\psi - 0.152 \ \text{(mm)} \tag{6}$$

Also using equation (5), the critical state of Ti-Nb claddings can be achieved with the following equation:

$$E = 11000\psi \ (\text{J/mm}^2) \tag{7}$$

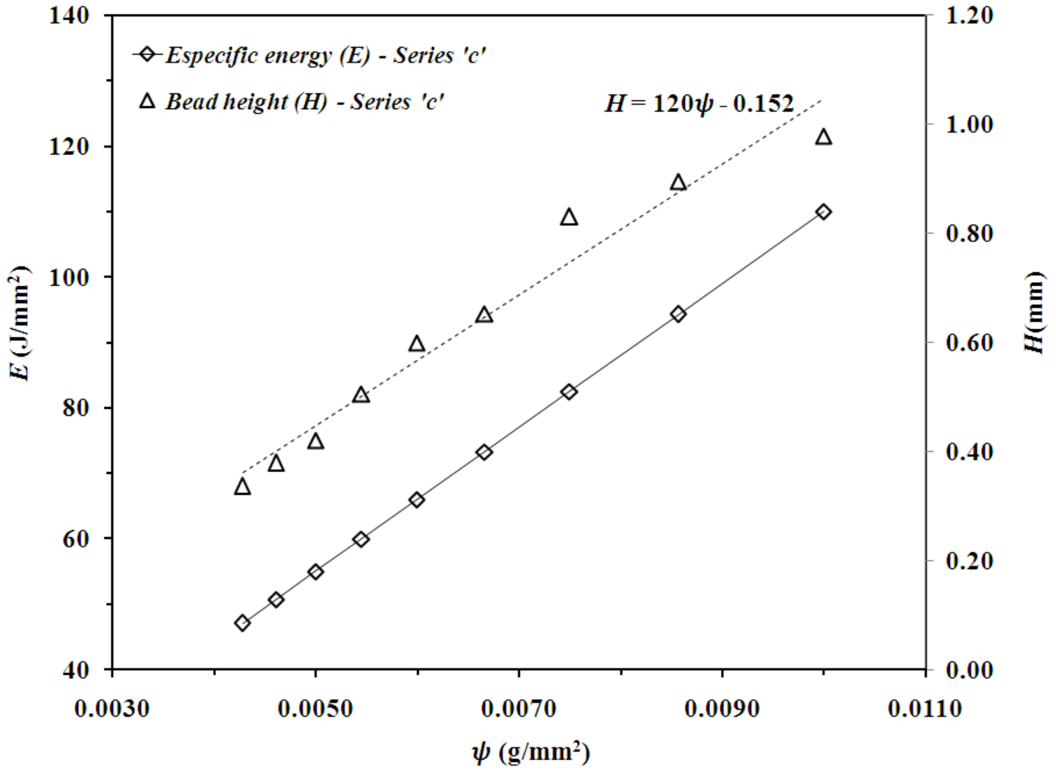

Fig.4 The E-ψ and H-ψ relationships for the 'c' series of parameters [74].

Using equations (2), (3), (6) and (7), assuming a constant laser beam diameter, the relationship between the individual processing parameters such as the laser power, powder feed rate and laser scan speed and the clad geometrical characteristics (i.e. the clad height) can be estimated for the critical state of Ti-Nb claddings. For example, for a given range of clad heights, an operating chart may be developed (as shown in Fig.5) with which one easily finds the appropriate processing parameters. Earlier in this section, it was shown experimentally that within the given operating range of V (i.e. 5-11.67 mm/s), the clad general quality is independent of V. Theoretically, there is no upper limit for V as long as the values of P and F are chosen correspondingly high enough. However, experimental verification is only done for the range of V specified above.

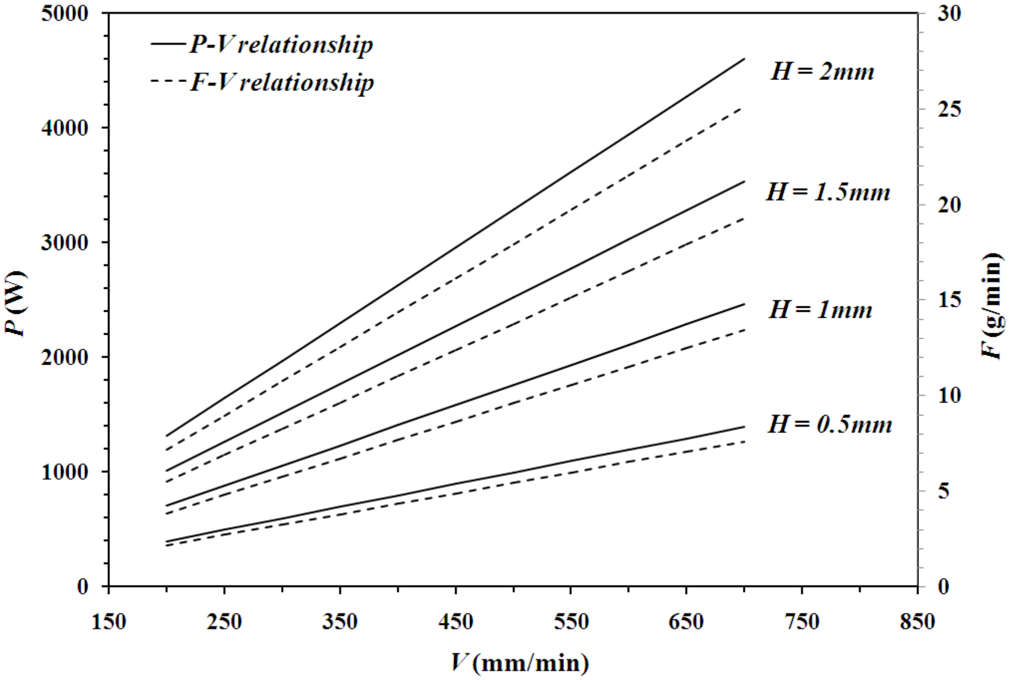

Fig.5 Operating window for laser deposition of Ti-45wt.%Nb on Ti-6Al-4V, representing *P-V* and *F-V* relationships with the assumption of constant beam diameter (~2 mm) [74].

2.2.3 Chemical composition

To analyse the chemical composition of the Ti-Nb claddings, EDS spectrums are taken from the entire clad section, as indicated in Fig.6 (a). Also, another EDS spectrum is taken from a small arbitrarily chosen area near the clad surface (shown in Fig.6 (b)). Multiple measurements (at least three) are performed for each sample and the average chemical composition values are listed in Table 2. According to this table, the near surface composition is consistent with that of the bulk composition for samples ***c1*** to ***c6***. This may be inferred as a proof of uniform composition throughout the clad sections. It should be mentioned that for the first six samples (***c1-c6***) even each individual pair of measurements revealed consistency of surface and bulk chemical composition values. However, from sample c7 to sample c9, individual measurements showed some differences between the surface and bulk chemical composition. Moreover, averaging individual measurements for sample ***c8*** did not reveal a significant difference although individual values were quite different.

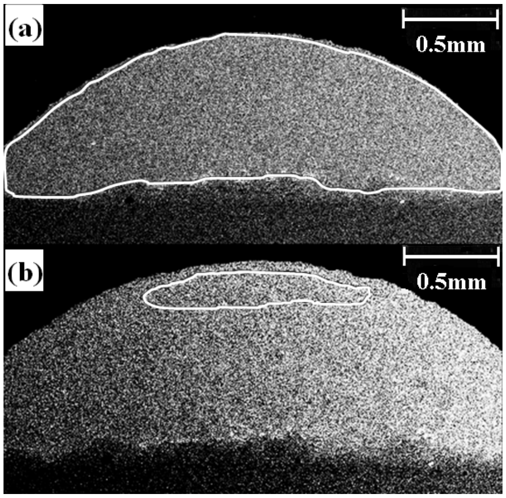

Fig.6 Schematic representation of targeted areas for EDS analysis of (a) the entire clad section and (b) near the clad surface [74].

Studies of mass transport in melt pools by Chan et al. [75, 76] with the help of numerical modelling showed that the very rapid homogenization during the laser surface alloying process cannot be explained by the diffusion mechanism but only by the intense Marangoni convection [77] due to high temperature gradients within the melt pool. In this case, diffusion in liquid state has a minor effect in homogenization of the melt pool composition. To incorporate the influence of processing parameters into the homogenization phenomenon, the surface tension number, *S*, is defined to characterize the influence of convection in melt pool homogenization during laser material processing. The greater the *S* value, the faster is convective flow and the higher role of convection in the melt pool homogenization. This factor correlates the thermocapillarity-induced convection velocity to the laser processing parameters as follow [75]:

$$S = \frac{(\partial\gamma/\partial T)qD}{\mu_l V k_t} \tag{8}$$

where $(\partial\gamma/\partial T)$ is a coefficient representing the temperature dependence of the melt surface tension (N/m K), q is the net absorbed power per unit area of the substrate (W/m^2), D is the laser beam diameter (m), μ_l is the viscosity of the melt pool (g/s m), V is the laser scan speed (m/s) and k_t is the thermal conductivity. Assuming the same $(\partial\gamma/\partial T)$ and μ_l values for all samples in series ‘c’, the *S* factor is inversely proportional to the laser scan speed. It is shown that for small *S* values (i.e. below 45 000 [76]) convection is negligible. As a rough estimate for metals, the convection speeds are much higher (several orders of magnitude) than the scan speeds applied in laser processing, resulting in a very rapid homogenization. However, in some materials such as Al-Nb alloys, very small values of $(\partial\gamma/\partial T)$ leads to *S* values sensitive not only to thermophysical properties of the melt pool but also to scan speed [78]. Therefore, the non-uniform clad chemical composition in samples ***c7*** to ***c9*** may be explained by the weakened role of convection in liquid homogenization due to the increased scan speeds. In other words, while the role of diffusion is negligible during the short lifetime of the melt pool in laser processing, the reduced effectiveness of the convective flow causes insufficient mass transport rates for formation of a uniform composition. It should be mentioned that the calculation of the exact S values was not done due to the high level of uncertainty involved in the calculation of thermophysical properties of Ti-Nb liquid alloys.

The clad dilution from the substrate is simply defined as the difference between the overall content of Ti+ Al+V in the clad sections and the Ti content of the original blend of powders. The former can be calculated from the measured clad bulk compositions (given in Table 2), while the later is 55 wt.% (determined from the composition of original Ti-45wt.%Nb powder mixture). The dilution values listed in Table 2 are then calculated by the following formula:

$$Clad\ dilution(\mathrm{wt.\%}) = [(\mathrm{Ti} + \mathrm{Al} + \mathrm{V})\mathrm{wt.\%}]_{\mathrm{clad}} - 55 \tag{9}$$

According to Table 2, the amount of dilution increases from sample ***c1*** to sample ***c9***. Alternatively, the amount of dilution is increased by simultaneous decrease in ψ and E values. The decrease in powder density, ψ, tends to improve the laser beam/substrate contact efficiency and increases the contribution of the substrate melting in the melt pool formation. It, therefore, resulted in a consistent increase in the amount of dilution from sample ***c1*** to sample ***c9***.

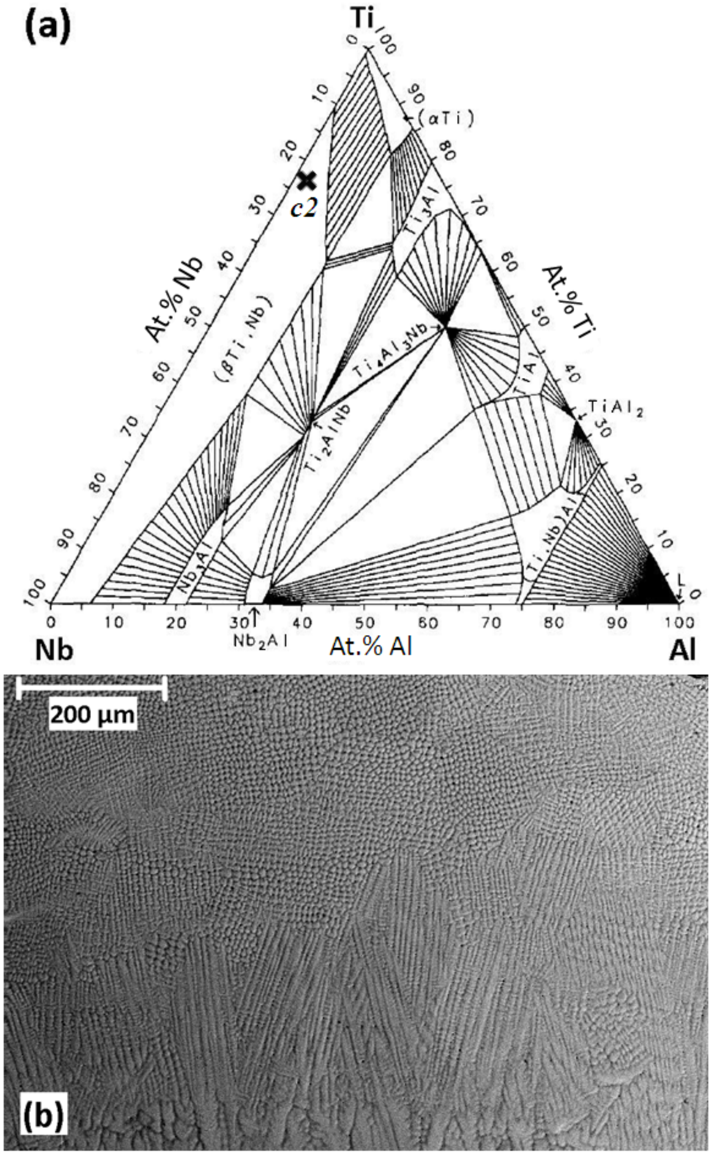

Fig. 7 (a) An isothermal section of the ternary Ti-Al-Nb phase diagram at 700ºC calculated and experimentally verified by Kattner and Boettinger [79]. The bulk composition of the clad section *c2* is marked on the *β*-phase region; (b) Backscatter SEM micrograph from a cross-sectional view of the clad microstructure showing the *β*-phase dendrites solidified at different orientations from the bottom to the top of the clad section *c3;* the dendrites at the top of the image are oriented along the normal to the surface [74].

2.2.4 The optimized cladding process

In the final cladding process to create a multi-layer coating free of Al and V, the ***c3*** set of parameters was used to ensure the lowest possible amount of dilution, a pore-free clad structure with highly uniform composition throughout the clad section. Furthermore, excluding the negligible vanadium content, the measured bulk composition of the sample ***c3*** (based on data given in Table 2) lies within the single-phase region of *β*(Ti, Nb) solid solution in the phase diagram shown in Fig. 7(a). Fig. 7(b) shows the corresponding single-phase structure consisting of *β*(Ti, Nb) dendrites solidified at different orientations throughout the clad section. Thus, with ***c3*** set of parameters, formation of a uniform single-phase structure can also be ensured. The final cladding, with the cross-section shown in Fig. 8, is made in three layers each consisting of 15 tracks overlapped by 60% in width. The EDS analysis performed for the second layer (over the area shown in Fig. 8) revealed a composition of ~Ti-40wt.%Nb with no trace of Al and V elements. Therefore, applying the conditions mentioned above, a compositionally modified surface of ~Ti-40wt.%Nb can be made by a 2-layer deposition of Ti-45wt.%Nb on Ti-6Al-4V.

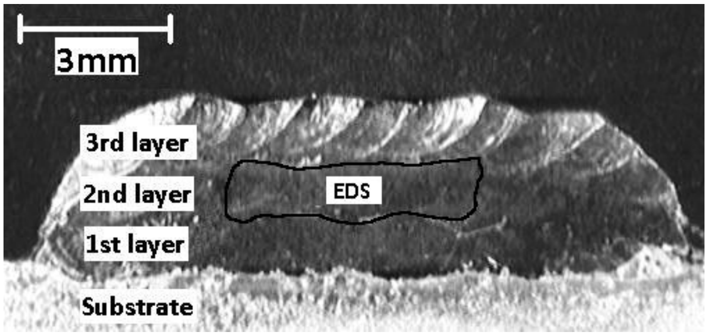

Fig. 8 An optical image showing the polished cross-section of a multi-layer Ti-Nb deposit on a Ti-6Al-4V substrate [74].

2.3 Summary

The surface composition of a Ti-6Al-4V plate was modified through multi-layer laser deposition of pre-mixed Ti-45wt.%Nb powder. Identified combined parameters in laser material processing, the laser specific energy, E, and the powder density, ψ, along with the newly defined energy variable named the laser supplied energy E_s, were successfully used to find the optimized set of individual processing parameters. The optimized set of deposition variables included a laser power of 1100 W, a laser spot diameter of 2 mm, a laser scan speed of 350 mm/min (or ~5.83 mm/s) and a powder feed rate of 0.1 g/s. Using these parameters, continuous single-beads are formed with pore-free sections exhibiting a homogeneous chemical composition with minimal dilution from the substrate. The microstructures were also uniform containing only dendrites of β(Ti, Nb) solid solution phase. Multi-layer deposition of multi-track claddings with 60% overlap in width resulted in the complete replacement of Al and V elements with Nb in the second layer (i.e. after ~1 mm in clad height from the clad/substrate interface) representing a Ti-40wt.%Nb alloy. Therefore, the modified surface of Ti-6Al-4V plate contains only Ti and Nb in composition exhibiting a better biocompatibility when exposed to human body environments.

Chapter 3:

Prediction of melt-pool morphology

The developed model simulates the real-time melt-pool shape and geometry and predicts the local solidification conditions along the solid/liquid interface. Using element activation/deactivation in each solution time step, relatively large clad structures can be finely meshed and solved in a coupled real-time fashion. To validate the model predictions of temperature distribution and final clad geometry, dynamic temperature measurements and optical microscopy are used for single-track deposition of AISI 304L steel on the same material. Furthermore, solidification microstructures developed in laser deposition of Ti-Nb alloys on Ti-6Al-4V are used for verification of the predicted melt-pool characteristics such as the solid/liquid interface orientation, the dendrite size variation and comparative clad dilutions.

3.1 Experimental setup and procedure

The experimental set-up is identical to the one used in Chapter 2. For the temperature measurement, XCIB inconel overbraided type K thermocouples with maximum temperature of 1250 °C were used at a data acquisition rate of 140 Hz. Pre-alloyed AISI 304L powder was deposited on a AISI 304L substrate in a 15 mm track. AISI 304L was chosen for experimental validation of the model since it can be easily processed in laser powder deposition. Pre-mixed Ti45Nb powder was deposited on Ti-6Al-4V substrates in single-tracks of 10 mm. In both cases, the substrate dimensions were 20×25×5 mm^3 with respect to the *x*, *y* and *z* axes according to Fig. 9. The deposition process was performed along the *y* axis starting at (0, 5,

5) mm. The operating parameters are listed in Table 3. The conditions used for deposition of Ti45Nb on Ti-6Al-4V are similar to those in samples ***c1*** and ***c7*** given in Chapter 2.

Table 3 Process parameters for deposition of AISI 304L on AISI 304L, and Ti45Nb on Ti-6Al-4V.

Parameter	**Material**		**Unit**
	AISI 304L	**Ti45Nb**	
Powder feed rate, F	0.1	0.1	g/s
Laser power, P_L	300	1100	W
Radius of the powder jet on the substrate	0.001	0.001	m
Radius of the laser beam on the substrate	0.0007	0.001	m
Ambient temperature, T_0	25	25	°C
Melting temperature of the substrate, T_m	1454	1735	°C
Laser scan velocity, V	1.5	5 & 10	mm/s

3.2 Description of the numerical model

The numerical model is developed using the finite element method to solve the transport equations for heat conduction considering the boundary conditions and relevant numerical adjustments for laser powder deposition.

3.2.1 Mathematical representation

The 3D time-dependent temperature distribution throughout the substrate and deposited additive material can be determined by solving the transient heat conduction equation:

$$\frac{\partial}{\partial x}\left(k\frac{\partial T}{\partial x}\right)+\frac{\partial}{\partial y}\left(k\frac{\partial T}{\partial y}\right)+\frac{\partial}{\partial z}\left(k_t\frac{\partial T}{\partial z}\right)+Q_l=\frac{\partial(\rho c_p T)}{\partial t} \tag{10}$$

where k_t (W/m K) is thermal conductivity, Q_l (W/m^3) is the power generated per unit volume, c_p (J/g K) is the specific heat capacity and ρ (g/m^3) is density.

Equation (10) must be solved along with the proper initial and boundary conditions. The initial and convection-radiation boundary conditions can be defined as follows:

For the substrate material:

$$T(x,y,z,0)=T_0 \tag{11}$$

For the newly added material in each solution time step:

$$T(x,y,z,t_{\text{activation}})=T_0 \tag{12}$$

For all materials:

$$T(x, y, z, \infty) = T_0 \tag{13}$$

Convection and radiation boundary conditions are applied to all outer surfaces:

$$k_t(\nabla T.\mathbf{n}) = [-h(T - T_0) - \varepsilon_R \sigma_R (T^4 - {T_0}^4)] \tag{14}$$

where T_0 (K) is the ambient temperature, $t_{\text{activation}}$ the time of addition of deposited material into the system, **n** the normal vector of the surface, ε_R the emissivity, h (W/m^2.K) the heat convection coefficient, and σ_R the Stefan-Boltzman constant (5.67×10^{-8} W/m^2.K^4). In this approach, the effect of the moving laser beam was considered in the boundary conditions. Therefore, the boundary condition, Equation (14), for the area of the substrate under the laser beam irradiation is defined as:

$$k_t(\nabla T.\mathbf{n}) = [\beta I - h(T - T_0) - \varepsilon_R \sigma_R \left(T^4 - {T_0}^4\right)] \tag{15}$$

where β is the absorption factor, I (W/m^2) is the laser power distribution on the substrate.

3.2.2 Assumptions and adjustments

Below is a list of the main adjustments and assumptions made to consider different involved process parameters and simplify the solution process where required.

1) The laser power intensity distribution is considered to be a circular Gaussian TEM$_{00}$ mode:

$$I(r) = \frac{2P_{\mathrm{L}}}{\pi r_{\mathrm{L}}^2} \exp\left(\frac{-2r^2}{r_{\mathrm{L}}^2}\right) \tag{16}$$

   where r_{L} (m) is the laser beam radius, r (m) is the distance from the center of the laser beam, and P_{L} (W) is the laser power. The projection of the circular distribution is applied to non-planar surfaces.

2) Unocic et al [80] have shown that, using a continuous wave Nd:YAG laser and depositing on a H-13 tool steel substrate, energy absorption factor in laser powder deposition changes in the range of 30-50% depending upon the laser power and laser scan velocity. They also showed that the powder feed rate and the type of powder have almost no effect on the energy absorption factor. Therefore, in this study, assuming the same effect from an AISI 304L stainless steel substrate and a continuous wave fiber laser, the laser power absorption factor is approximated to a value of 40%.
3) All material properties are considered temperature dependent.
4) The heat convection coefficient h is taken 40 W/m^2.K for all temperatures.

5) Only those powder particles entering the area within the intersection of the melt pool and powder stream are considered to be melted and deposited.
6) The effect of latent heat of fusion is taken into account through modification of the specific heat capacity at the melting temperature [21, 22, 81]:

$$c_{\mathrm{p}}^{*} = \frac{L_{\mathrm{f}}}{T_{\mathrm{m}} - T_{0}} + c_{\mathrm{p}} \tag{17}$$

   where c_{p} is the specific heat capacity, c_{p}^{*} the modified specific heat capacity, L_{f} the latent heat of fusion, and T_{m} the melting temperature.

7) The convective heat transfer caused by fluid flow within the melt-pool, also called "themocapillary (Marangoni) flow" [82], is considered by modifying the thermal conductivity for the liquid phase by a factor of 2.5.
8) The powder particles coming through the lateral feeding system travel a short distance under the laser beam irradiation before entering the melt-pool. It is assumed that the particles are not heated until they enter the melt-pool. In other words, the deposition material is added at ambient temperature into the melt-pool domain.
9) The powder catchment efficiency of the system, C, is defined as the fraction of the injected powder which is received within the deposition zone, i.e. the intersectional area between the laser beam column and the substrate surface. Considering the characteristics of the lateral feeding system, the powder catchment efficiency for this study is approximated to 50%.

3.2.3 Modelling architecture and solution strategy

To dynamically incorporate the material addition in the modelling procedure, the cladding process is simulated sequentially, considering the concept originally proposed for the decoupled geometry prediction of the additive material in a single and multilayer deposition process [10, 16]. The final solution of each time step is considered as the initial conditions for the next time step. In each step, a new set of elements representing the deposited material at the corresponding time interval is selected and activated. The developed technique is schematically illustrated in Fig. 9.

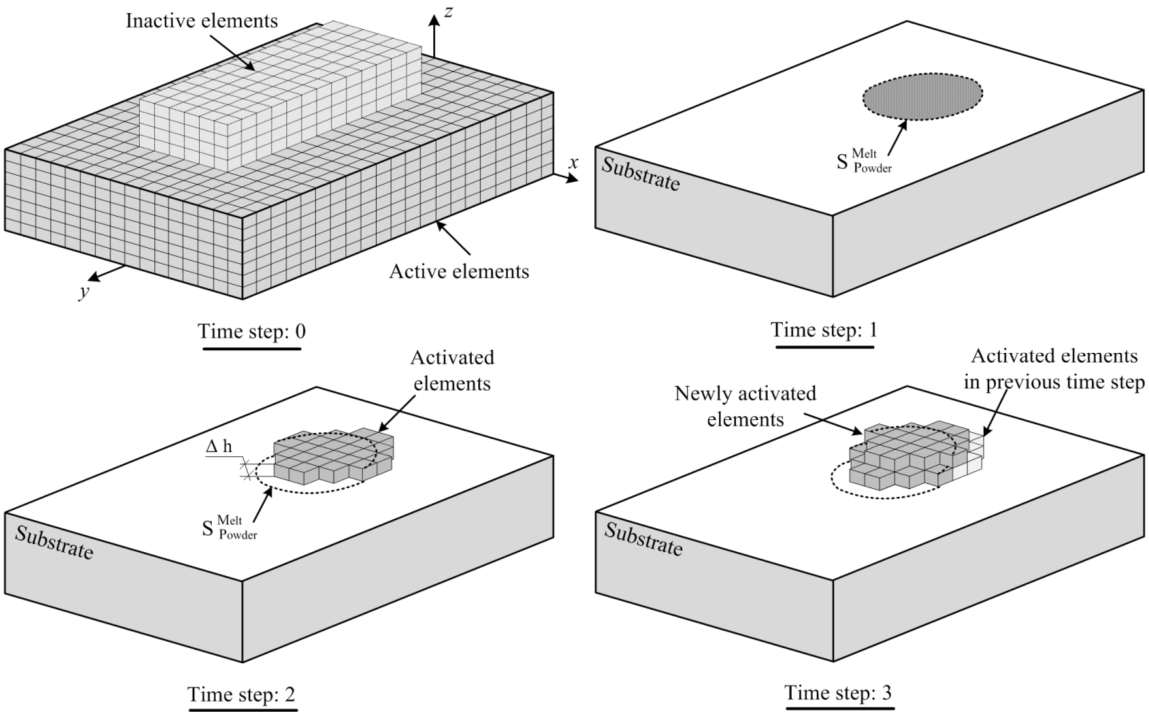

Fig. 9 Modelling of the laser cladding process: dynamic addition of material over the solution time steps to predict the deposition geometry [66].

The simulation process starts with solving the heat transfer governing equations for the irradiated substrate held initially at room temperature, T_0. Having obtained the temperature distribution for Time step 1, the initial melt-pool boundary on the substrate surface can be approximated based on the pre-defined melting temperature of the clad material, as illustrated in Fig. 9. In Time step 2, within the intersectional area of the melt pool and powder stream, $S_{\mathrm{powder}}^{\mathrm{melt}}$, the inactive elements attached to the substrate surface are activated. With the newly developed geometry, the model is solved for the updated location of the laser beam which is calculated from the laser scan velocity and scanning direction. By repeating this procedure for successive time steps, the accumulation of added elements will form the geometry of the deposited material, as illustrated in Fig. 10(a). The number of layers of elements, n_{l}, to be activated in each time step can be determined from the deposition height, Δh, and the element side length, l_{el}:

$$n_{\mathrm{l}} = \Delta h / l_{\mathrm{el}} \tag{18}$$

Assuming a uniform and steady flow of powder particles into the deposition zone, the deposition height Δh in each time step can be calculated as follows:

$$\Delta h = \frac{FC\Delta t}{\rho(\pi r_{\mathrm{L}}{}^2 + 2r_{\mathrm{L}}V\Delta t)} \tag{19}$$

where Δt (s) is the solution time step, F (g/s) the powder feed rate, ρ (g/m^3) the powder density and V (m/s) the laser scan velocity. Based on the criteria used for approximation of the powder catchment efficiency C, the term $FC\Delta t$ equals the amount of powder in each time step entering the intersectional area of the laser beam circular column and the substrate surface. The term $(\pi {r_\mathrm{L}}^2 + 2r_\mathrm{L}V\Delta t)$ represents the area swept by the laser beam on the substrate surface in one time step.

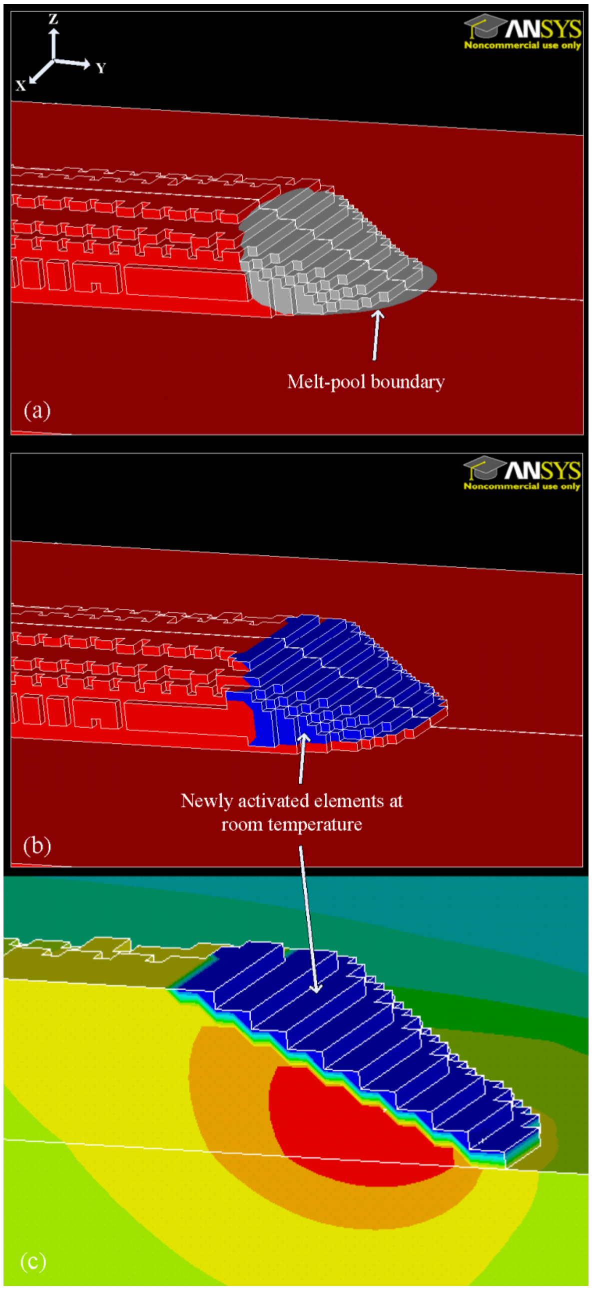

Fig. 10 Schematic representation of material addition procedure during the deposition process; (a) Melt-pool boundary determined based on the nodal temperature at $t = t_1$, (b) activated element s at room temperature (in blue) for solution at $t = t_1 + \Delta t$, (c) activated elements associated with the nodes within the melt-pool in a symmetric half-view with respect to Y-Z plane [66].

Fig. 10 shows schematically the activation procedure of the newly added elements in one time step. As can be seen in Fig. 10 (a), the selected elements in grey have temperatures higher than a predefined melting temperature. The resultant curved interface represents the estimated 3D projection of the melt-pool boundary on the surface. Based on the calculated number of the layers of elements n_l, the inactive elements associated with the outer surface of the melt-pool area are activated, as shown in Fig. 10(b). The new model is then solved considering the ambient temperature for the newly activated elements, depicted in the darkest colour in Fig. 10 (c). Heat flux boundary condition from the laser beam irradiation is applied only on upper face of the surface elements located within the intersectional area of the laser beam column and the built model.

3.3 Results and discussion

The deposition process of AISI 304L is modelled and the simulation outputs are experimentally verified for the temperature history of the substrate and the clad geometrical development.

3.3.1 Process simulation and its verification

To validate the simulation results, the single-track deposition of AISI 304L steel on a 25×20×5 mm^3 substrate of the same material is numerically and experimentally performed using the operating parameters given in Table 3. Listed in Table 4 are the temperature dependent thermophysical properties of AISI 304L steel as well as the modifications made for numerical incorporation of the marangoni flow and the effect of the latent heat release upon melting.

To simulate the deposition process, the solution domain is discretized using 78,561 8-node hexagonal elements. The clad material must be meshed as finely as to predict the deposition geometry. However, depending on the overall size of the model and the preset laser scanning length, the computer capacity limits the minimum feasible element size along the deposition line. The smallest element size in the model is then determined by the slowest allowable computational speed. In this study, it is found that with the minimum element size of 0.1 mm, a reasonably fine resolution in the predicted deposition geometry can be obtained for most processing conditions. In this case, the overall simulation time falls within an acceptable range, i.e., from a couple of hours to one day. However, a reduction in the minimum element size in the model to values below 0.1 mm may drastically extend the simulation procedure.

Table 4 Thermophysical properties of AISI 304L steel [83].

T (°C)	Density (kg m^{-3})	c_p (J kg^{-1} K^{-1})	k_t (W m^{-1} K^{-1})	ε_R $^{(d)}$
25	8020	480	14.8	0.10
100	8000	500	15.8	0.11
200	7950	530	17.7	0.12
300	7903	540	18.8	0.13
400	7855	560	20.7	0.13
500	7805	570	21.4	0.14
600	7751	595	23.5	0.15
700	7698	600	24.5	0.16
800	7645	620	25.8	0.17
900	7590	630	27.5	0.17
1000	7532	642	28.8	0.18
1100	7481	656	29.9	0.18
1200	7431	675	31.6	0.19
1300	7381	695	32.8	0.19
1360	7351	720	33.5	0.20
1454	7302	730	33.5	0.20
1454$^{(a)}$	6900	983$^{(b)}$	83.75$^{(c)}$	0.20
1500	6860	800	83.75$^{(c)}$	0.20
1600	6780	800	83.75$^{(c)}$	0.20

(a) The melting temperature, T_m.

(b) The modified value of the specific heat capacity calculated from the actual value, i.e., 800, to account for the release of the latent heat of fusion at the melting point.

(c) The modified value of heat conductivity for temperatures higher than the melting point to consider the effect of marangoni flow. The original value is multiplied by a factor of 2.5.

(d) The emissivity values are considered for polished surfaces.

For both the experiment and simulation, the laser beam is set to scan a 15 mm straight line on the substrate from point (0, 5, 5) mm to (0, 20, 5) mm with respect to the x, y, and z axes, as schematically shown in Fig. 9. Fig. 11(a) depicts the simulated temperature distribution across the process domain and the predicted geometry of the deposited material. Similar to the past simulation studies dealing with dynamic addition of elements [19, 21, 22], the real-time thermocouple measurements are used to verify the validity of the simulated temperature distribution at selected positions in the substrate throughout the process. In this way, the temperature of two points inside the substrate, i.e., point A at (3, 17, 3.5) mm and point B at (3, 12, 3.5) mm with respect to the x, y, and z axes, are measured during the process. These two points lie underneath the deposition track in unmelted substrate. The measured data are then compared with its numerical counterparts, as shown in Fig. 13.

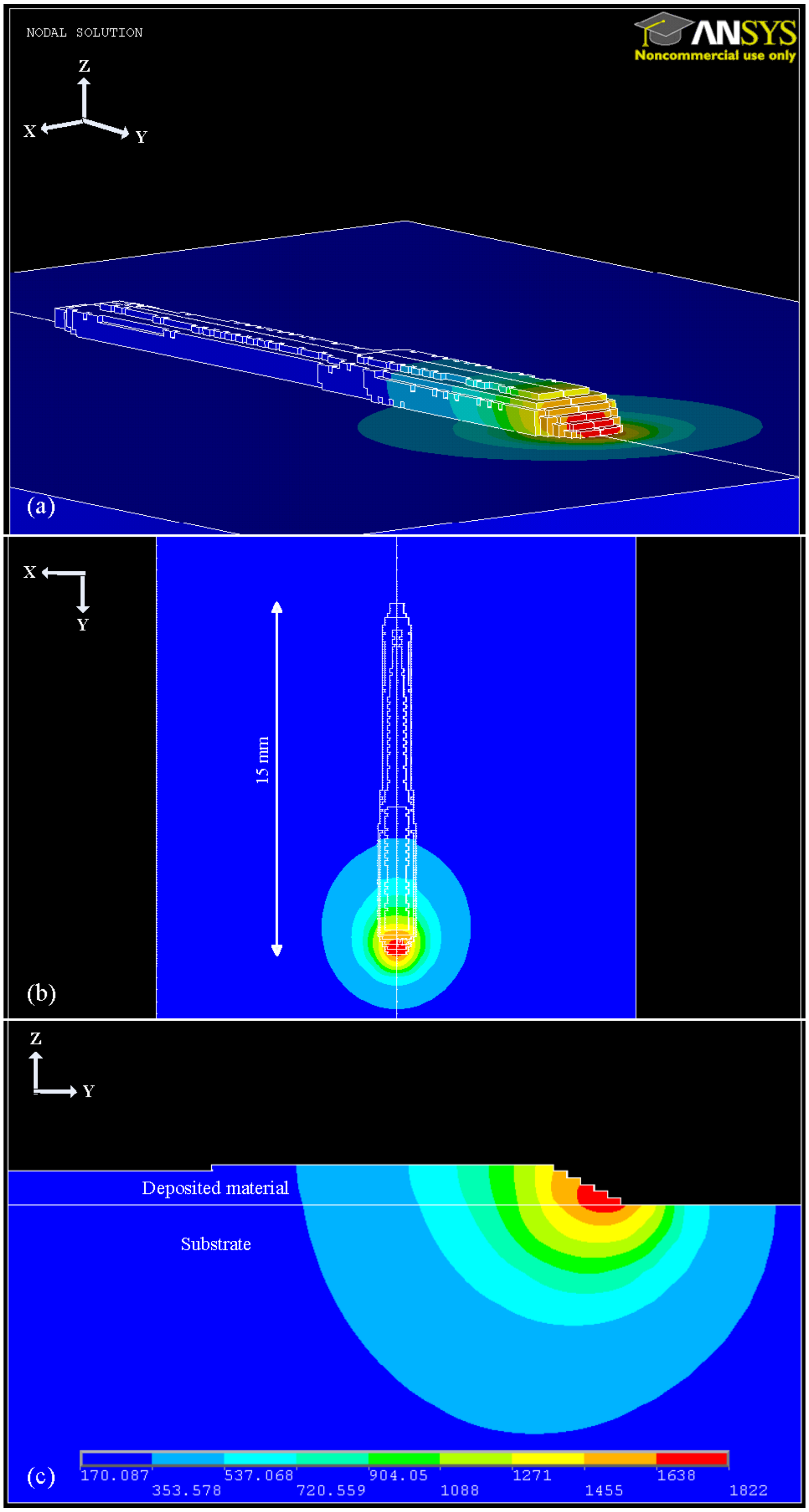

Fig. 11 Transient temperature distribution, in °C, and geometry prediction of a single-track deposition of AISI 304L; (a) 3D clad geometrical development, (b) clad width prediction at top view, (c) clad height prediction from a half-symmetry view with respect to Y-Z plane [66].

The development of the melt-pool boundary during the process is illustrated in Fig. 12. Since the deposition material is the same as that of the substrate, the melting temperature of the clad section is taken as that of AISI 304L steel, i.e., T_m = 1454 °C. As can be inferred from Fig. 12, the estimated boundary expands until t = 7.4 s where after the melt-pool geometry and morphology stabilize. Referring also to Fig. 11(b), the stabilization of the melt-pool occurs approximately where the final clad width is established.

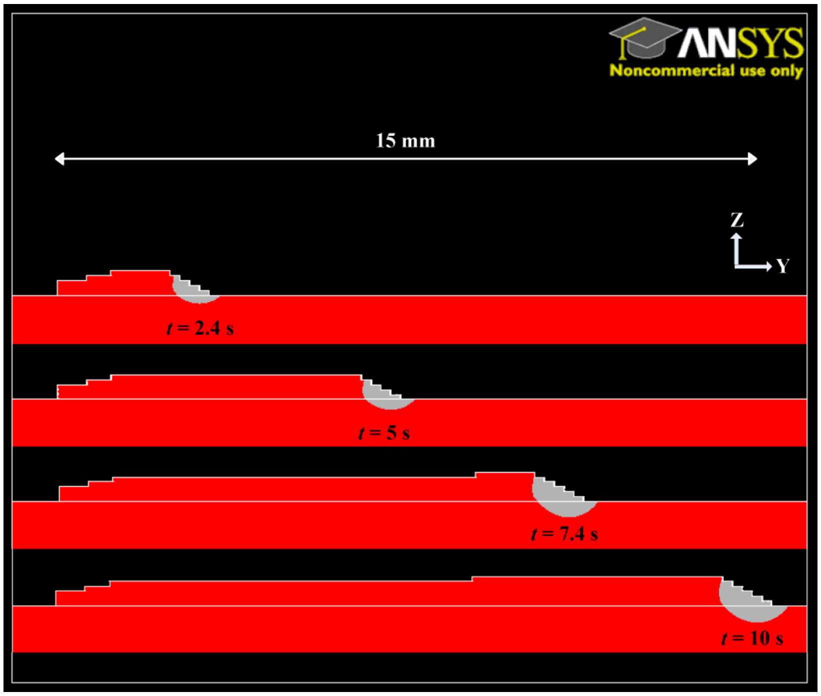

Fig. 12 Development of melt-pool boundaries during single-track laser deposition of AISI 304L. The boundary was estimated with the isotherm of T_M = 1454 °C [66].

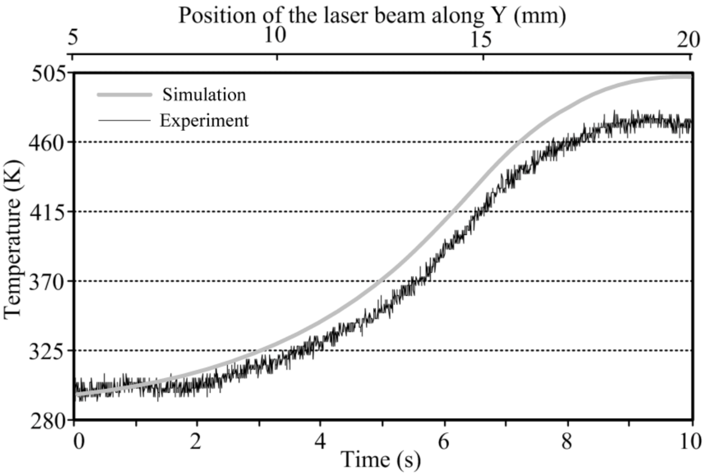

Point A

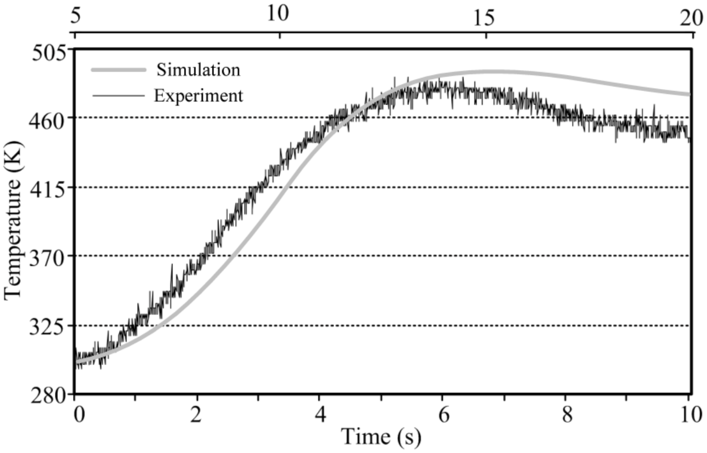

Point B

Fig. 13 Experimental and numerical temperature measurement for points A and B inside the substrate [66].

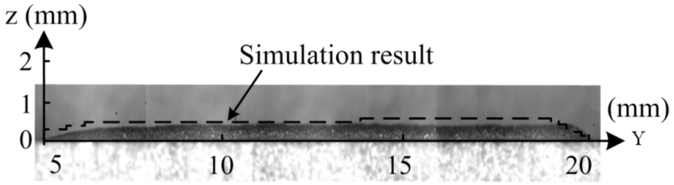

Fig. 14 Longitudinal profile of the experimental deposited track and its numerical simulated counterpart [66].

Comparisons between the numerical and experimental results show a maximum of ~5 percent error in prediction of the temporal temperature distribution at the two selected points inside the substrate. However, the prediction accuracy may vary to some extent for points closer to and within the moving melt-pool area, in which the real temperature cannot be experimentally evaluated using a thermocouple set-up. Fig. 14 shows a comparison of the shape of the deposited formed along a longitudinal section of the clad as determined from experiment and the model. A good agreement between the heights of the simulated and actual clad is obtained. The average error in prediction of the deposition geometry is 8.3 percent. These errors can be attributed to experimental setup, assumptions made in the modelling process, and also the inherent errors of the numerical methods.

3.3.2 A case study: laser deposition of Ti-Nb alloys

The temporal development of the melt-pool largely affects the physical characteristics associated with the solid/liquid interface such as the local orientation and temperature gradient, which themselves are the key factors in developing microstructural features upon solidification. The ability of the model to predict the local parameters along the solid/liquid interface is verified with the evolution of dendritic structures developed during laser deposition of Ti45Nb alloys on Ti-6Al-4V using the processing conditions given in Chapter 2, i.e., the sets ***c1*** and ***c7.***

3.3.2.1 *Development of melt-pool and clad geometries*

Referring to the Ti-Nb phase diagram shown in Fig. 15, the difference between the liquidus temperatures of pure Ti and Ti-45wt%Nb is a relatively small, i.e., ~100 °C. As an approximation, the liquidus temperature of the clad material is taken as the average of that of pure Ti and Ti-45wt%Nb, excluding the minor elements Al and V from the substrate material, i.e., Ti-6Al-4V. Also, since the freezing range of the Ti-Nb alloys up to 45wt%Nb is fairly narrow, the melting temperature of the clad material is taken to be the same as its liquidus temperature, i.e., ~1735 °C. Due to the dilution effect from the substrate material, the clad composition is richer in Ti than that of the original Ti45Nb powder. It is shown that the amount of dilution in this system largely depends on the processing parameters [74]. Considering the Ti-rich clad composition and also taking into account the high uncertainty in the thermophysical data in the Ti-Nb system, the thermal properties of the clad material are approximated assuming the same as those of Ti-6Al-4V.

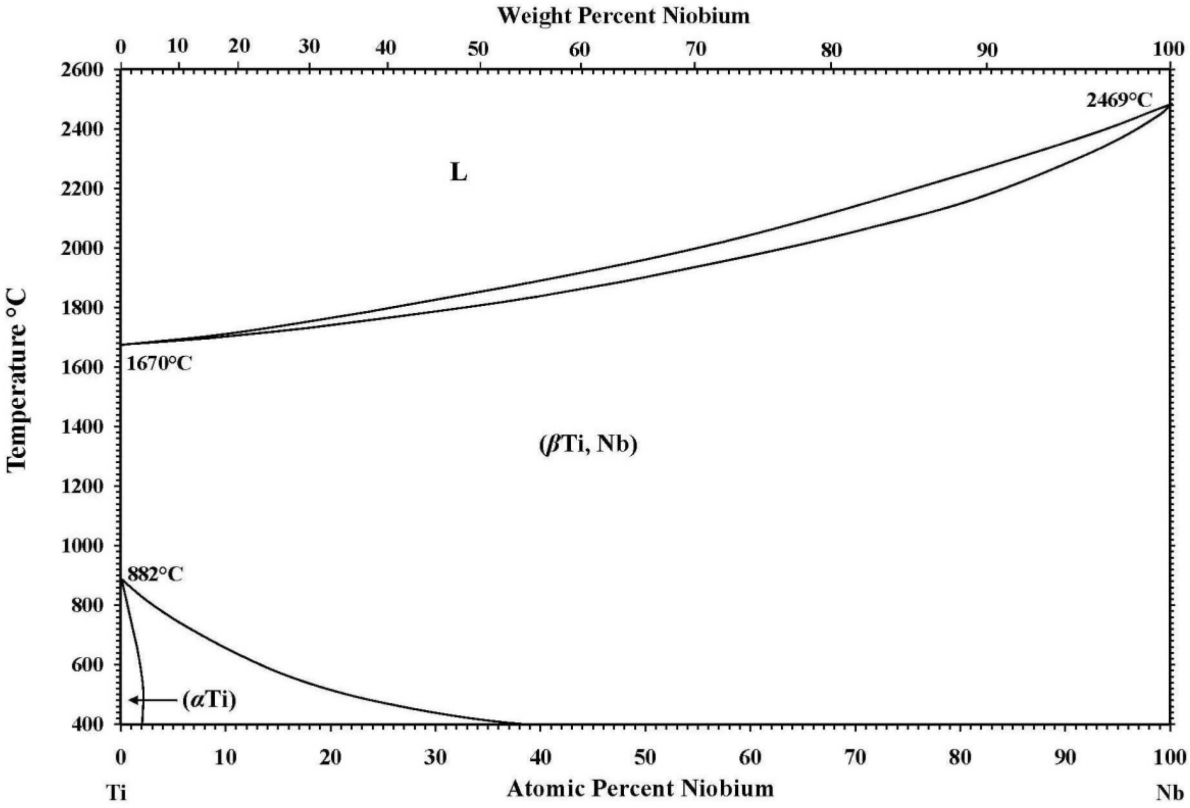

Fig. 15 The assessed Ti-Nb phase diagram [84].

Fig. 16 shows the simulated temporal temperature distribution and clad geometry obtained during the deposition of Ti45Nb on Ti-6Al-4V. The laser deposition process is simulated with the operating parameters and thermophysical properties given in Table 3 and Table 5, respectively. The development of the melt-pool boundary is investigated using the approximated melting temperature of the clad material, i.e., ~1735 °C.

Table 5 Thermophysical properties of Ti-6Al-4V [83].

T (°C)	**Density (kg m^{-3})**	**c_p (J kg^{-1} K^{-1})**	**k_t (W m^{-1} K^{-1})**	**ε_R** (f)
25	4420	546	7.00	0.50
100	4406	562	7.45	0.50
200	4395	584	8.75	0.50
300	4381	606	10.15	0.50
400	4366	629	11.35	0.50
500	4350	651	12.60	0.50
600	4336	673	14.20	0.50
700	4324	694	15.50	0.50
800	4309	714	17.80	0.50
900	4294	734	20.20	0.49
995	4282	753	22.70	0.49
995(a)	4282	693(b)	19.30	0.49
1100	4267	660	21.00	0.48
1200	4252	678	22.90	0.47
1300	4240	696	23.70	0.46
1400	4225	714	24.60	0.46
1500	4205	732	25.80	0.46
1600	4198	750	27.00	0.45
1650	4189	759	28.40	0.45
1650(c)	3920	1007(d)	83.50(e)	0.45
1700	3886	831	83.50(e)	0.45
1800	3818	831	83.50(e)	0.45
1900	3750	831	83.50(e)	0.45

(a) The transition temperature for $\alpha \rightarrow \beta$.

(b) The modified value of the specific heat capacity calculated from the actual value, i.e., 641 J/kg.K, to account for the release of the latent heat of the $\alpha \rightarrow \beta$ transformation at the transition temperature.

(c) The melting temperature, T_m

(d) The modified value of the specific heat capacity calculated from the actual value, i.e., 831 J/kg.K, to account for the release of the latent heat of fusion at the melting point.

(e) The modified value of heat conductivity for temperatures higher than the melting point to consider the effect of marangoni flow. The original value is multiplied by a factor of 2.5.

(f) The emissivity values are considered for polished surfaces.

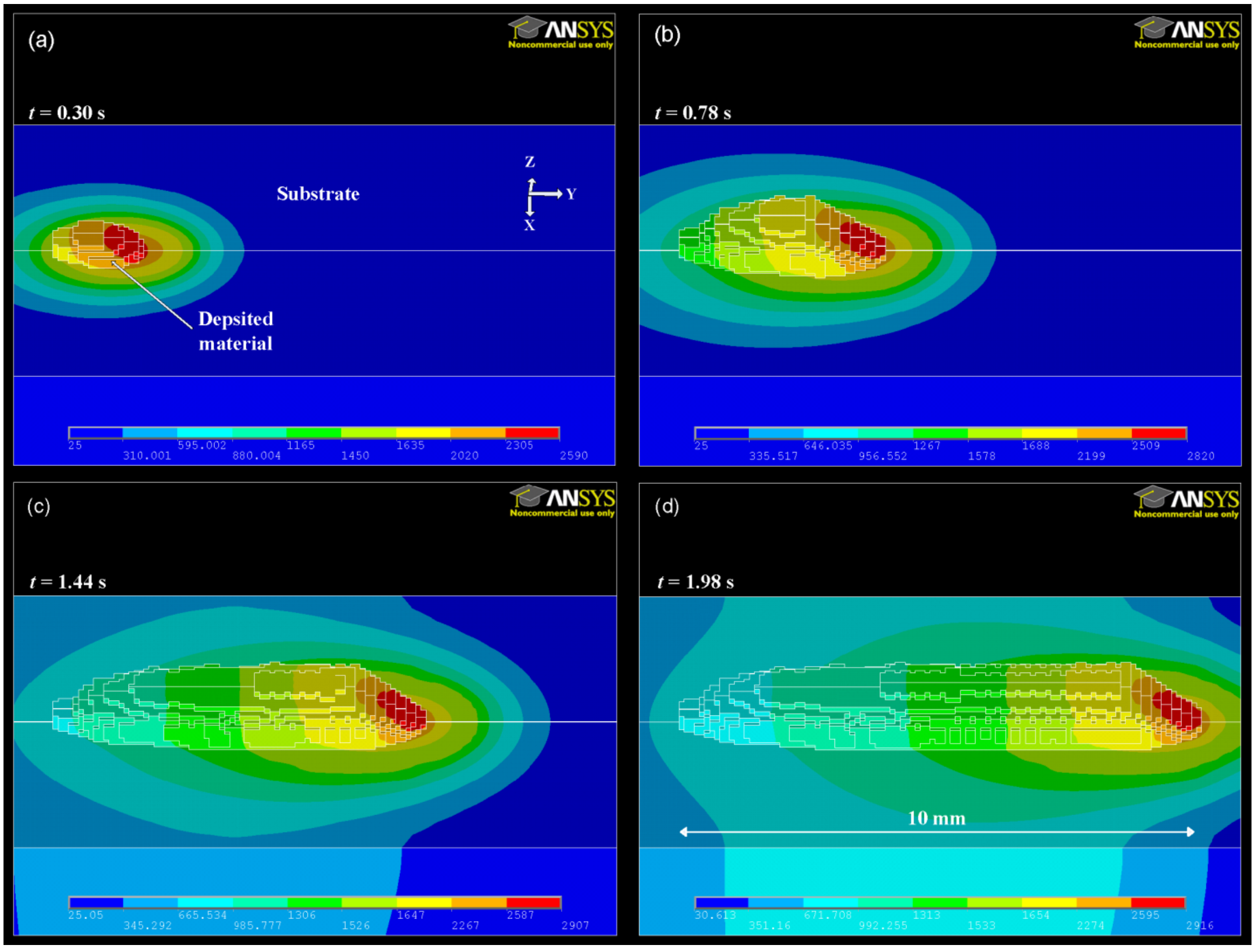

Fig. 16 (a-d) Temporal development of temperature distribution, in °C, and geometrical features in single-track laser deposition of Ti45Nb on Ti-6Al-4V at 5 mm/s laser scan velocity, i.e., the sample *c3* in Chapter 2 [66].

Fig. 17 demonstrates the model accuracy in the prediction of the cross-sectional geometry for the deposition of Ti45Nb on Ti-6Al-4V. The experimental cross-sectional view embedded on the corresponding predicted geometry is taken at 7 mm from the starting point of the deposited track. According to this figure, the general morphology of the cross-section and the deposition height is reasonably predicted by the model. However, finer mesh sizes are required within the clad section in order to enhance the geometrical development of the curved surface of the clad section. The effect of fluid flow in convective heat transfer is considered through modification of the thermal conductivity at temperatures higher than the melting point. However, the gas/solid/liquid triple joint on both sides of the clad section would have appeared softer if the model had been also solved for the fluid velocity. Due to the computational costs for large structures and long deposition paths, solution of the momentum equations for the fluid velocity is not considered in this model. It can nevertheless be taken into account in future improvements of the existing model.

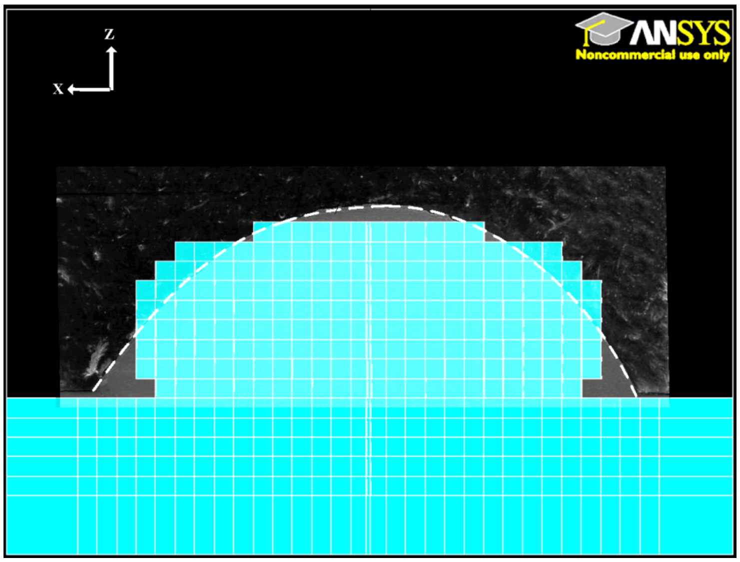

Fig. 17 Comparison between the predicted and experimentally deposited cross-sectional geometry of Ti45Nb on Ti-6Al-4V at 5 mm/s laser scan velocity, i.e., the sample *c3* in Chapter 2 [66]; the embedded optical image is taken from ref. [74].

3.3.2.2 *Solid/Liquid interface and solidification microstructure*

The morphology and the scale developed in directional solidification of alloys are primarily controlled by the locally imposed conditions such as the temperature gradient G and solidification velocity V_s. According to linear stability theory by Mullins and Sekerka [85], the ratio G/V_s determines whether a planar or dendritic structure forms upon solidification. Also, following the model developed by Kurz and Fisher [2], the dendrite tip radius during solidification of binary alloys at medium-range velocities is mainly controlled by G and V_s:

$$R = 2\pi \left[\frac{\Gamma}{m_l G_c - G}\right]^{\frac{1}{2}} \tag{20}$$

$$G_c = -\frac{V_s}{D_l} C_l^*(1-k) \tag{21}$$

where R is the dendrite tip radius, G_c the solute concentration gradient in the liquid at the dendrite tip, Γ the Gibbs-Thomson parameter, m_l the liquidus slope, D_l the liquid diffusion coefficient of the solute atom, k the partition coefficient and C_l^* the solute concentration in the liquid at the dendrite tip. Although the equilibrium dendrite tip radius largely affects the size of microstructural features after solidification, the evolution of cellular/dendritic arm spacing must be determined through numerical solution of the diffusion fields at the solid/liquid interface [86].

Neglecting the effect of preferred growth directions at very high temperature gradients normally present in laser powder deposition, the local dendrite growth velocity is related to the laser scan velocity by [24, 87]:

$$V_s = V Cos\theta \tag{22}$$

where θ is the angle between the normal to the interface and the laser scanning direction. Therefore, considering the general morphology of the solid/liquid interface during laser processing, the solidification rate across the depth varies from zero near the bottom of the clad/substrate interface to a maximum near the top of the clad surface, depending upon the size and the shape of the melt-pool, which themselves depend upon the processing conditions [87]. With 2D numerical analysis, temperature gradient is also shown to vary from a maximum to a minimum along the melt-pool depth towards the surface [88].

By means of finite element analysis, the 3D solid/liquid interface can be predicted with no need of microstructural analysis as a pre-requisite, as illustrated in Fig. 18(a). Fig. 18(b) depicts the variation of temperature gradient on the elements associated with the predicted solid/liquid interface. As can be observed in this figure, the temperature gradient decreases from bottom to top on any Y-Z plane cutting through the melt-pool. This is in accordance with 2D numerical simulation results by Hoadley et al [88]. Moreover, the interface velocity can be evaluated using the local orientation on the predicted interface, as illustrated in Fig. 19(b). Fig. 19(a) shows the estimated solid/liquid interface morphology on the Y-Z symmetry plane. In Fig. 19(b), the estimated solid/liquid interface is imposed on the dendritic pattern revealed in the longitudinal section of deposited Ti-Nb structure. The microstructure orientation, θ_1, of three different points along the interface, p1, p2 and p3, is compared with their corresponding interface normal direction, θ_2. A maximum of 20 percent deviation is calculated at p3 which may be partly explained by the errors in numerical simulation of the interface orientation. Another potential contributing factor, as also pointed out by Zimmermann et al [87], is the effect of preferred crystallographic directions for the growth of the dendritic structures.

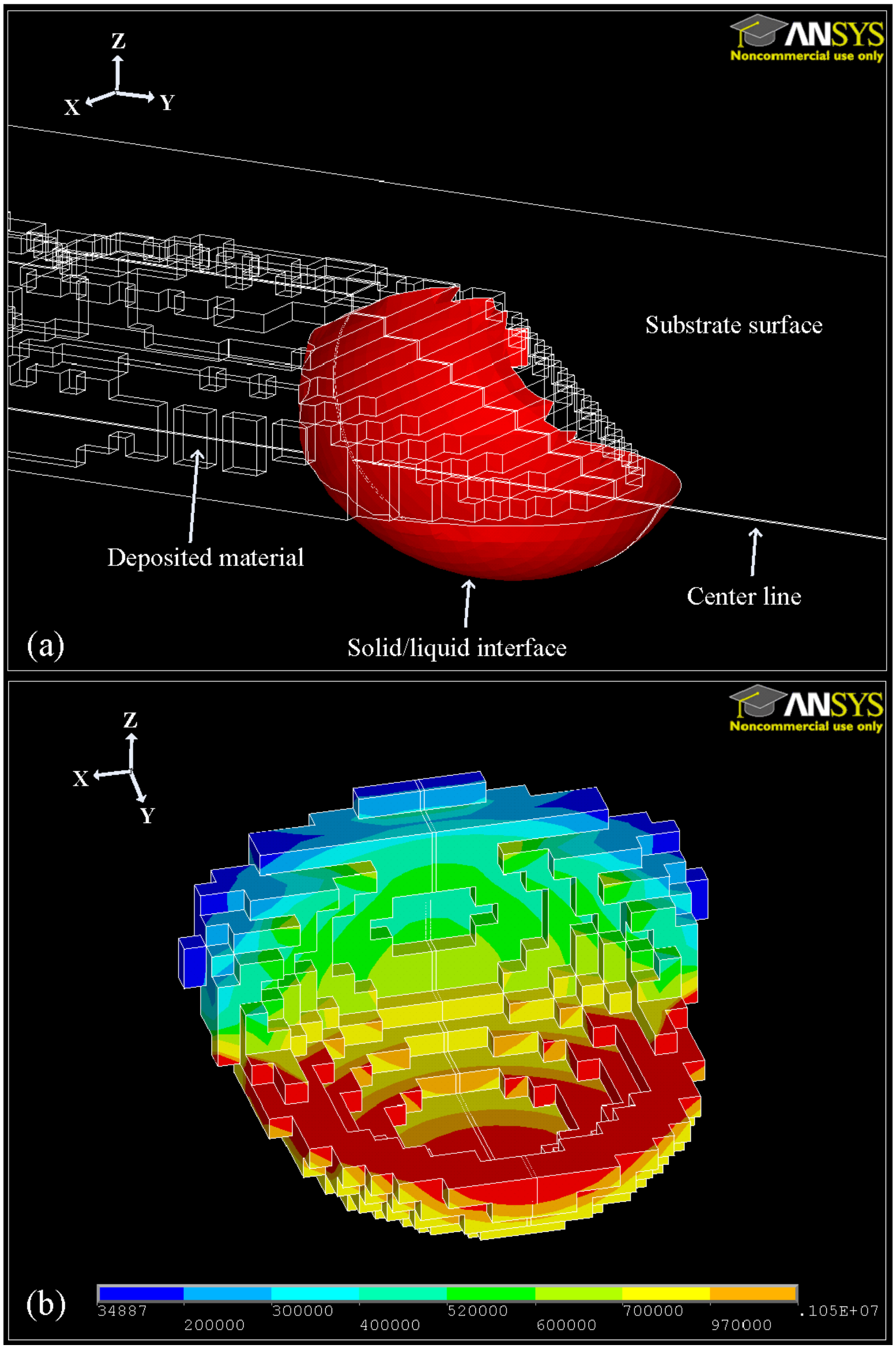

Fig. 18 Simulated deposition of Ti45Nb on Ti-6Al-4V at 5 mm/s laser scan velocity, i.e., the sample *c3* in Chapter 2; (a) The melt-pool boundaries estimated at 7mm deposition with the isotherm of melting point TM = 1735 °C, (b) the distribution of temperature gradient, in °C/m, on the elements attached to the nodes associated with the estimated melt-pool boundary [66].

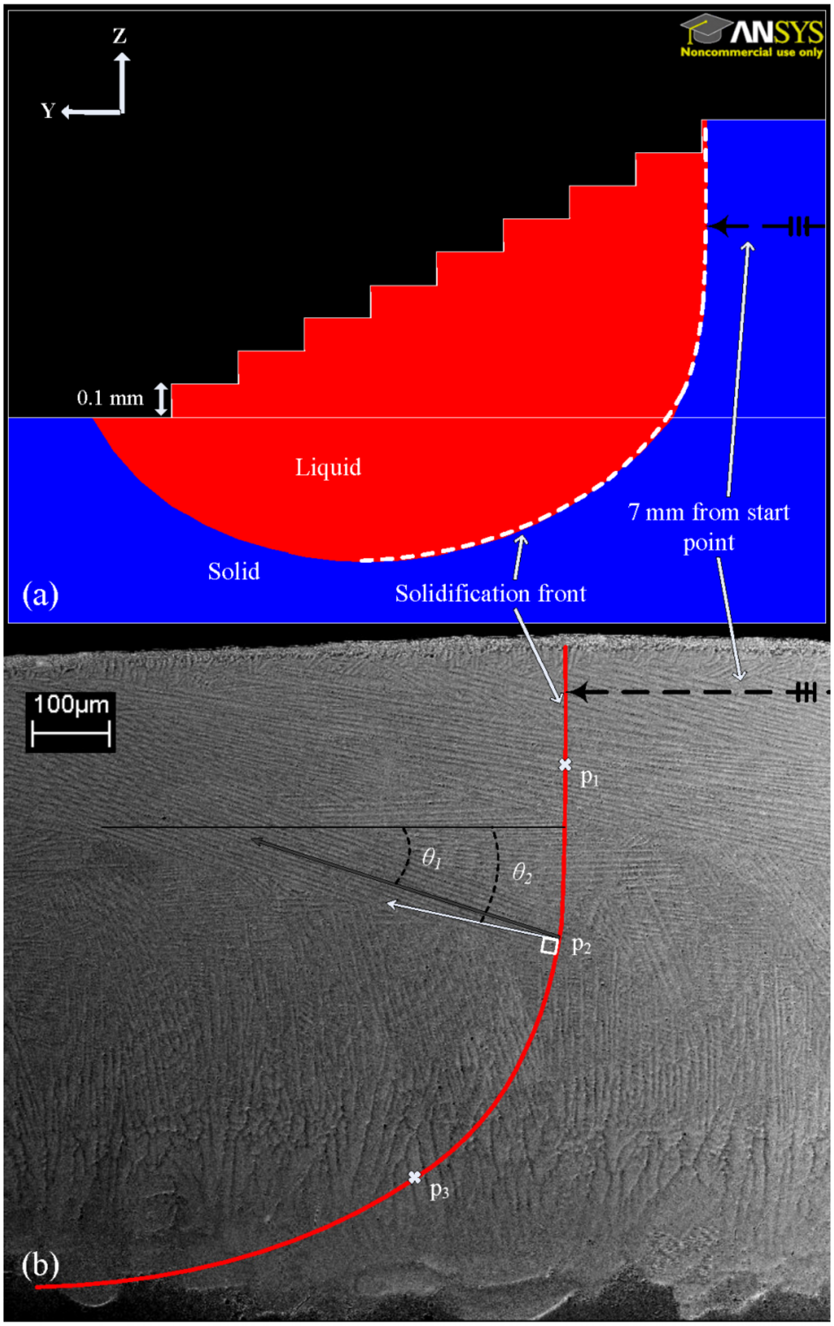

Fig. 19 (a) Estimated melt-pool boundaries and the orientation of solidification front on Y-Z symmetry plane of Fig. 18(a); (b) comparison between the predicted orientation of solid/liquid interface (the angle of normal to the red line and the horizon), θ_2, and the experimentally revealed dendrite growth direction, θ_1, along the height of the Ti-Nb clad longitudinal section, i.e., the sample *c3* in Chapter 2 [66].

3.3.2.3 *Clad dilution*

The dilution from the substrate is an important factor affecting the final properties of the deposited material when the injected powder has a different chemical composition from the substrate material. The developed model is used to investigate the effect of the laser scan velocity on the clad dilution. Fig. 20

shows the half-symmetric view of the melt-pool boundaries developed at 5 and 10 mm/s laser scan velocities, corresponding to conditions for samples ***c***3 and ***c***7, respectively, in Chapter 2. According to the comparative depths sketched on the Y-Z symmetry plane, d5 and d10, increase of the laser scan velocity from 5 to 10 mm/s does not significantly affect the melt penetration depth into the substrate. However, the maximum clad height for 5 mm/s laser scan velocity is approximately twice as that for 10 mm/s. Since the melted portion of the substrate is almost the same overall size for both velocities, it can be concluded that the dilution from the substrate into the clad section is higher at the higher velocity, i.e., 10 mm/s. This trend is in accordance with the results of the analytical evaluation of the dilution in laser powder deposition by Fathi et al [89] in which, using mathematical modeling, they pointed out that the amount of dilution goes up by increasing the laser scan velocity.

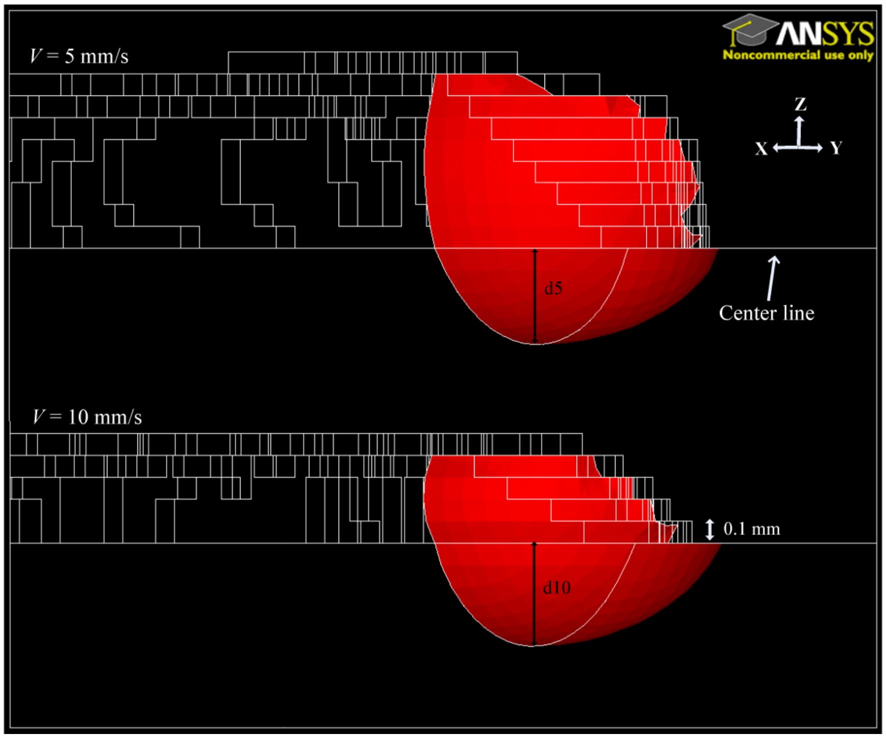

Fig. 20 Half-symmetry views on Y-Z plane for the melt-pool development after 7mm deposition of Ti45Nb on Ti-6Al-4V at two different laser scan velocities, 5 and 10 mm/s [66].

3.4 Summary

A transient finite element model was developed to simulate the temperature distribution and real-time development of the melt-pool morphology and geometry in the laser powder deposition. The proposed modelling strategy was successfully developed based on element activation/deactivation to incorporate the effect of additive material during the deposition process. Experimental verification of the model by thermocouple measurement of temperature revealed a maximum of ~5 percent error in prediction of the temporal temperature distribution of the selected points inside the substrate in deposition of AISI 304L. The geometrical features of the clad section made of AISI 304L were predicted by an average error of ~8.3 percent.

The present model shows a great ability to simulate the morphology of solid/liquid interfaces during deposition of Ti45Nb on Ti-6Al-4V. Using the predicted orientation, the local solidification velocity and direction were calculated along the solid/liquid interface. A comparison between the estimated solidification directions and the experimentally revealed orientation of dendrites showed a maximum of ~20 percent deviation. It was argued that, other than the inherent errors of numerical analyses, this deviation can be also due to the effect of preferred crystallographic directions for the dendrite growth at the interface. The temperature gradient, as the other contributing factor in determination of solidification microstructures, was also evaluated along the predicted solid/liquid interface. Moreover, in agreement with previous analytical simulations, the present model showed that the amount of dilution increases by the laser scan velocity. Listed below are the main advantages of the present model over the past numerical investigations:

1) Real-time geometrical characteristics of the melt-pool and deposited materials were predicted without assuming predefined geometries or shapes as priories.
2) The spatial resolution within the melt-pool area was satisfactory for realistic 3D representation of the solid/liquid interface morphology. The model outputs were easily treated for extraction of local conditions data for constrained solidification, i.e., the solidification velocity and the temperature gradient along the solid/liquid interface.
3) The heat transfer equations are coupled to the deposition process with additive material.
4) The real-time morphology of the melt surface was simulated representing a realistically inclined surface under the laser beam irradiation.

Using the same method represented in this study, the accuracy in prediction of geometrical features can be significantly improved in future by enhancing the spatial resolution of the computational domain, and by also solving for the fluid velocity.

Chapter 4:

Evaluation of local solidification conditions

As discussed earlier in Chapter 2, through a general process optimization, the best overall performance of laser powder deposition of Ti-Nb alloys was obtained using conditions of sample ***c3*** given in Table 1 and Table 2. Fig. 21 presents the resultant microstructure of this sample along a longitudinal cross-section cut through the centerline of the deposited track. As can be seen, the dendritic morphology varies in size and orientation along the sample height which is due to the differences in the local solidification conditions. This chapter deals with the general analytical modelling of Ti-Nb alloy solidification which will further be used for the evaluation of the developed numerical models of the resulting solidification microstructures.

4.1 Solidification modelling of Ti-Nb alloys using KGT model

In powder deposition using concentrated sources of power such as a laser at relatively high deposition speeds, the liquid solidifies directionally from the substrate. Since such a solid/liquid metallurgical interface already exists nucleation easily occurs. Therefore solidification during laser cladding, and thus the types of microstructures produced, are controlled by the growth phenomena. The focus of this section is then only on the growth selection phenomena (neglecting nucleation even if it can be of importance especially in undercooled solidification processing). Also, various growth models developed so far can be only applied for steady state conditions which, in short time intervals, are valid for most rapid solidification processes including laser powder deposition. Furthermore, quasi-steady state conditions can be assumed as a good approximation for most cases [87].

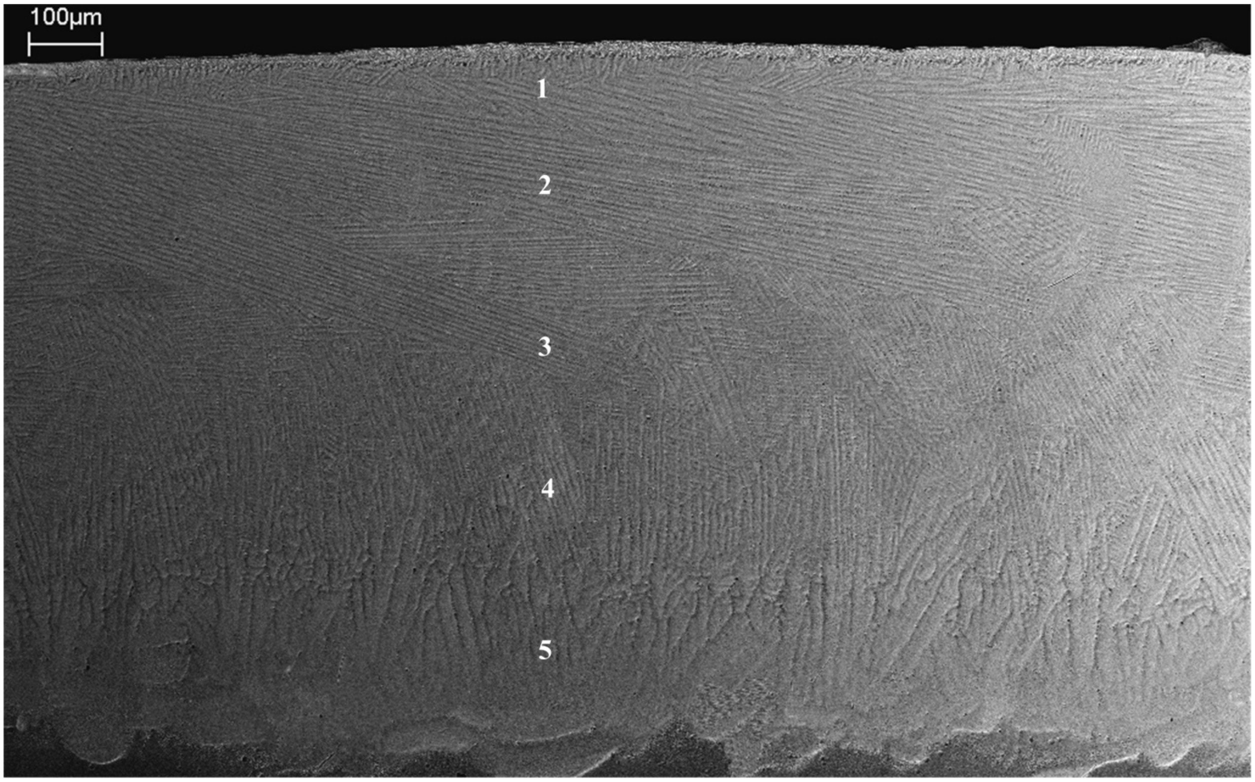

Fig. 21 The solidification microstructure of sample *c3* through a centered longitudinal section.

Since a constrained dendrite growth with a positive temperature gradient in both the liquid and the solid is present in the laser powder deposition process, the growth phenomenon can be assumed to occur at steady-state with idealized thermal conditions (i.e. constant thermal gradient in the liquid at the tip/melt interface). In such cases, the predictions of the KGT (Kurz-Giovanola-Trivedi) model [90] have been shown to agree very well with the experimental measurements [56]. A detailed description of the KGT model is presented in Appendix A1.

Input parameters to the solidification model include the material properties and the interface velocity, while the model calculates the corresponding dendrite tip radius (R). The input parameters of the solidification model are listed in Table 6.

4.1.1 Process parameters

The interface velocity V_s is correlated to the laser scan speed V. In unidirectional solidification, it can be assumed that the temperature gradient in the liquid at the interface is constant and equal to the overall temperature gradient within the interface in the melt pool which is determined by solving the heat flow equations with boundary conditions imposed by the process parameters (i.e. the laser scan speed V the laser power P_L and the laser beam diameter D). In unidirectional solidification and constrained dendritic growth, the temperature gradient at the interface in the liquid is not affected by the solidification process since the latent heat of fusion is dissipated through the solid and the thermal diffusion length is much greater than the scale of the dendritic region [91].

Table 6 The input parameters used in the KGT model for liquid Ti-rich Ti-Nb alloys.

Process parameters	V_s	Interface velocity, m s^{-1}
	G	Temperature gradient in the liquid, K m^{-1}
Material parameters	c_0	Alloy bulk chemical composition, wt.%
	Γ	Gibbs Thompson parameter, K m *Estimated value*: 1.941×10^{-7}
	D_0	Proportionality constant for diffusion in liquid alloy, m^2 s^{-1} *Estimated value*: 7.3352×10^{-8}
	Q	Activation energy of solute diffusion in liquid alloy, cal mole^{-1} *Estimated value*: 1.1111×10^{4}
	R_g	Gas constant, cal mole^{-1} K^{-1} 1.9858775
	T_m	Melting point of the solvent, K 1941
	k	Equilibrium partition coefficient, 1.25
	m_l	Equilibrium liquidus slope, K/wt.% 5

4.1.2 Material properties

Among the material properties listed in Table 6, R_g is a global constant and T_m and c_0 are defined by the selected alloy system, while the remainder are thermophysical alloy properties which must be estimated from the existing material models in the literature.

4.1.2.1 *Gibbs Thompson coefficient,* Γ

According to Mullins and Sekerka [85], the Gibbs Thompson coefficient of a dilute liquid binary alloy at its melting temperature can be estimated as:

$$\Gamma = \gamma T_\mathrm{m}/L_f \tag{23}$$

where T_m is the melting point of the solvent, γ is the specific liquid-solid interfacial free energy assumed independent of composition and L is the latent heat of the solvent per unit volume. Typically for metals, $\gamma/L_f \approx 10^{-10}$ m. Therefore, Γ for any dilute binary alloy may be estimated generally as:

$$\Gamma = T_{\mathrm{m}} \times 10^{-10}\ \mathrm{K\,m} \tag{24}$$

The Gibbs Thompson coefficient of liquid Ti-rich Ti-Nb alloys at a temperature near their melting point can be estimated as 1.941×10^{-7} K m. Since the dendrite tip temperature is normally close to the liquidus temperature corresponding to the initial alloy composition, the above estimation is reasonable.

4.1.2.2 *Temperature dependence of diffusion coefficient, D_0 and Q*

A simple and easily applicable model developed by Liu *et al.* [92] is used to estimate the diffusion coefficient of Nb in liquid Ti-rich Ti-Nb alloys. They have presented a way to correlate the solute diffusivity to the self-diffusion coefficients in a dilute binary alloy. This model has been shown to perfectly match the experimental values of solute diffusivity in low-melting temperature dilute alloys (e.g. diffusivity of Cu in dilute Ag-Cu alloys). According to the model, the diffusion coefficient of solute A in solvent B can be estimated as:

$$D_{\mathrm{AB}}^{\mathrm{l}} = \left(\frac{d_{\mathrm{B}}}{d_{\mathrm{A}}}\right) D_{\mathrm{BB}}^{\mathrm{l}} = D_{0,\mathrm{l}}^{\mathrm{BB}} \left(\frac{d_{\mathrm{B}}}{d_{\mathrm{A}}}\right) \exp\left(-\frac{Q^{\mathrm{l}}}{R_{\mathrm{g}}T}\right) \tag{25}$$

$$Q^{\mathrm{l}} = 0.17Q^{\mathrm{s}} = 0.17R_{\mathrm{g}}T_{\mathrm{m}}(16 + k_0) \tag{26}$$

$$D_{0,\mathrm{l}}^{\mathrm{BB}} = (8.95 - 0.0734A) \times 10^{-8}\ \mathrm{m^2\,s^{-1}} \tag{27}$$

where $D_{\mathrm{BB}}^{\mathrm{l}}$ is the self-diffusion coefficient of the solvent B, d_{B} is the atomic diameter of the solvent B, d_{A} is the atomic diameter of the solute A, D_0^{BB} is the proportionality constant of the liquid solvent B, Q^{l} is the self-diffusion activation energy of solute B, k_0 is the atomic valence (1, 2, 3 for BCC, HCP, FCC structures, respectively), T_{m} is the melting point of the solvent B and A is the atomic number of the solvent B. The diffusivity of Nb in liquid Ti-rich Ti-Nb alloys can then be found at different temperatures using the following calculated constants:

- $D_{0,\mathrm{l}}^{\mathrm{Nb\ in\ Ti}}$ or $D_0 = 7.3352 \times 10^{-8}\ \mathrm{m^2\,s^{-1}}$
- Q^{l} or $Q = 1.1111 \times 10^4$ cal mole^{-1}.

4.1.2.3 *Equilibrium liquidus slope and partition coefficient, m_l and k*

Referring to the Ti-Nb equilibrium phase diagram shown in Fig. 15, the liquidus slope for Ti-rich alloys up to 35 wt.%Nb can be assumed constant and equal to 5 K/wt.%. The partition coefficient is also assumed to be 1.25 around the same compositional range.

4.1.3 *R*-V_{s} relationship in Ti-Nb alloys

According to the KGT model (refer to the principles given in Appendix A1), the following equations are numerically solved to determine the R-V_{s} relationship for a given alloy composition c_0 and a constant positive thermal gradient G in the liquid.

$$R = 2\pi\left[\frac{\Gamma}{m_l G_{\mathrm{c}} \xi_{\mathrm{c}} - G}\right]^{\frac{1}{2}} \tag{28}$$

$$\xi_{\mathrm{c}} = 1 - \frac{2k}{\{1+[2\pi/P]^2\}^{\frac{1}{2}} - 1 + 2k} \tag{29}$$

$$G_{\mathrm{c}} = -\frac{V_s}{D_{\mathrm{l}}} c_{\mathrm{l}}^*(1-k) \tag{30}$$

$$c_{\mathrm{l}}^* = \frac{c_0}{1-(1-k)\mathrm{Iv}(P)} \tag{31}$$

$$\mathrm{Iv}(P) \equiv P\exp(P)E_1(P) \tag{32}$$

$$P = RV_s/(2D_{\mathrm{l}}) \tag{33}$$

where $E_1(P)$ is the exponential integral function. The alloy composition c_0, temperature gradient G and solidification velocity V_{s} can be controlled to yield the desired dendritic features such as the tip radius R.

4.1.3.1 *Effect of alloy composition,* c_0

As can be seen in Fig. 22, the higher the solute content (i.e., Nb) the wider velocity range and the smaller tip radius for dendritic growth. Referring to the Ti-Nb phase diagram in Fig. 15, the freezing range expands as the Nb content increases and thus extends the velocity range of dendritic growth. It should also be noted that only a planar front is stable outside the velocity ranges shown in Fig. 22 for each alloy.

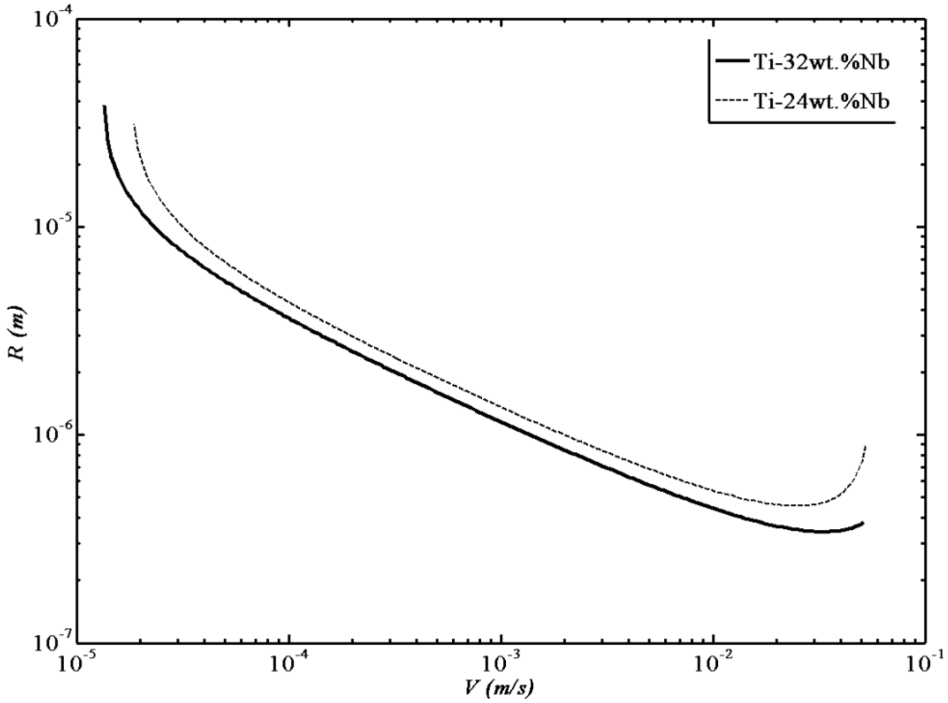

Fig. 22 The effect of c_0 on the estimated R-V_s relationship using KGT model in solidification of Ti-rich Ti-Nb alloys at temperature gradient of $G=2.5\times10^5$ K m^{-1}.

4.1.3.2 *Effect of temperature gradient, G*

As will be reported in more detail later, both temperature gradients and velocities near the top and bottom of the experimental clad have been determined from the thermal model of Chapter 3. The values for temperature gradient were $G=2.5\times10^5$ K m^{-1} and $G=5.0\times10^5$ K m^{-1} near the top and bottom of the clad (shown in Fig. 21), respectively. These values were chosen for calculations to demonstrate the influence of temperature gradient on the R-V_s relationship (see Fig. 23). Increasing the temperature gradient shrinks the range of tip velocities within which the dendrites can grow with a steady tip radius. Also, for the range of experimental velocities (i.e. 6.2×10^{-3} and 2×10^{-4} m s^{-1} at the top and bottom of the clad respectively), the temperature gradients of interest have little effect on the dendrite tip radius.

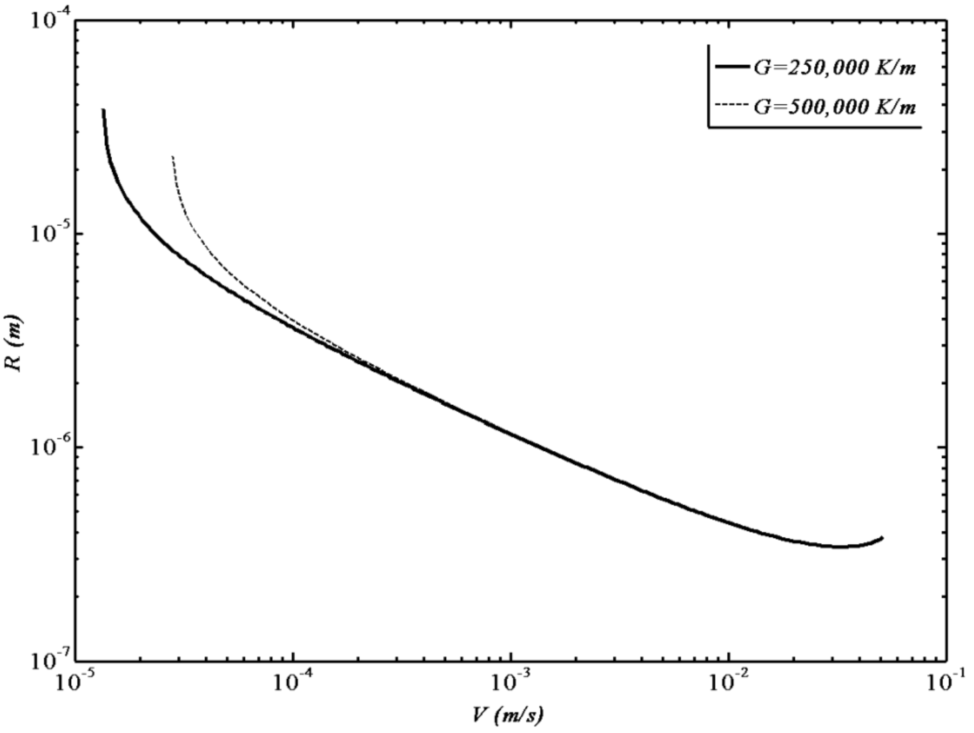

Fig. 23 The effect of G on the estimated R-V_s relationship using KGT model in solidification of Ti-32wt.%Nb alloy.

4.1.4 Growth direction

Constrained solidification conditions in laser treatment of materials are the consequence of the high laser scan velocity with respect to the heat diffusion rate, $^{a}/_{r_L}$, where a is the heat diffusivity [24, 87]. The resulting solidification microstructures are normally elongated in shape. It is shown that the solidification direction usually occurs along the normal to the solid/liquid interface. Therefore, the local growth rate V_s can be calculated knowing the angle θ between the interface normal and the laser scan direction, as demonstrated in Fig. 19(b). However, in the case of cellular/dendritic structures with developed side branches, not only the heat flux constraint but also the preferred crystallographic directions may affect the resultant microstructure orientations [87]. The local dendrite growth velocity is then related to the laser scan velocity by:

$$V_S = VCos\theta / Cos\varphi \tag{34}$$

where φ is the angle between the interface normal and the dendrite axis. Due to the normally large imposed temperature gradients during laser processing, the microstructures are often free of side branches and grow primarily normal to the interface, i.e., $\varphi = 0$ [24].

4.2 Columnar-to-equiaxed transition (CET)

Once nucleated, equiaxed grains grow in volume fractions limited by a number of parameters such as the thermal gradient and the solidification velocity. Therefore, they might be entrapped into the columnar region or overlap it if their volume fraction is large. Depending on the volume fraction of equiaxed grains when being passed by the columnar front, the growth type can be determined.

Since CET occurs in directional growth of dendrites, the KGT model can be used to predict the dendrite tip temperature and composition which enable us to determine the liquidus temperature and composition profiles ahead of the columnar front. Also, the same model with the assumption of zero temperature gradient can be applied for the equiaxed growth of dendrites within the constitutionally supercooled region ahead of the advancing columnar front [93]. The local undercooling profile can be obtained from the difference between the local temperature imposed by the existing temperature gradient and the liquidus temperature determined from the liquid composition ahead of the advancing columnar front. The growth velocity of nucleated equiaxed dendrites within the constitutionally supercooled region is then determined with the help of the calculated local undercooling and solved KGT model for the case of zero temperature gradient. A detailed analysis of the concentration and temperature fields within the constitutionally undercooled liquid in front of the dendrites in directional solidification is given in Appendix A2.

4.2.1 Mathematical formulation

The size of each equiaxed grain when it reaches the columnar front can be numerically obtained by integration [93]:

$$R_e = \int_0^{z_n} \frac{V_e[z]}{V_s} dz \tag{35}$$

where z_n is the distance from the interface where the undercooling in the liquid is equal to the nucleation undercooling. $V_{\mathrm{e}}[z]$ is the growth velocity of equiaxed grains calculated based on the local composition and undercooling as indicated in equations (89) and (94). The extended volume fraction of unhindered equiaxed dendrites can be obtained using the size of each grain, assuming unhindered spherical dendritic grains [93]:

$$\emptyset_e = N_0 4\pi {R_e}^3/3 \tag{36}$$

The actual volume fraction can then be calculated using Avrami's equation to remove the assumption of unhindered growth [93]:

$$\emptyset = 1 - \exp[-\emptyset_{\mathrm{e}}] \tag{37}$$

The composition profile along the isotherm of the dendrite tips (i.e. between two dendrite tips) varies from a maximum at the tip to a minimum in-between. This correspondingly introduces a fluctuating liquidus temperature profile at the columnar interface. Therefore, assuming constant composition profile along the interface makes the calculated undercooling less than the actual value, thus underestimating the volume fraction of equiaxed grains [93].

At the first stage, for a given temperature gradient, we need to calculate the tip composition and temperature of the advancing columnar front at different velocities (i.e. the C_l^*-V_s and T_t-V_s relationships). This is achieved by using KGT model and numerically solving equations (67)-(70), (72) and (64) for a predefined temperature gradient, as explained in Section 4.1. Then, at a given interface velocity, the equilibrium liquidus temperature is calculated using the corresponding C_l^* value and the liquidus line equation given in Table 6. The local undercooling ahead of the advancing interface, for each interface velocity and assuming a constant predefined temperature gradient, can be determined by going through equations (90)-(94) with substitution of the corresponding dendrite tip temperature.

Once the local undercooling is obtained at a given interface velocity, the growth velocity of the nucleated equiaxed grains within the liquid ahead of the columnar interface ($V_e[z]$) can be estimated using the pre-solved KGT model for the case of zero temperature gradient. Then, for definite values of nucleation undercooling, ΔT_n, and the number of heterogeneous nucleation sites per unit volume, N_0, equations (35)-(37) can be numerically solved to determine the actual volume fraction of equiaxed dendrites at different velocities of the columnar front (i.e. the $\emptyset$- V_s relationship).

4.2.2 Input and output parameters

Other than the regular input parameters in the KGT model listed in Table 6, the CET model requires two other material-related input parameters: nucleation undercooling ΔT_n, and the number of heterogeneous nucleation sites N_0 per unit volume. ΔT_n is normally assumed to be approximately 1K for heterogeneous nucleation in liquid metals [93]. However, no clear basis exist to estimate the N_0 value for a given material system. For binary alloy systems, N_0 is considered as one per cubic millimetre or 1000/cm^3 [93, 94, 95]. a_0 values within the commonly applied range of 5-50 Å [90] do not notably affect the R- V_s and C_s^*-V_s relationships through almost the entire velocity range.

4.2.3 Numerical scheme

The numerical procedure to determine the transition from mixed columnar-equiaxed to fully equiaxed structure is schematically illustrated in Fig. 24. The output of the model is the CET vector containing the interface velocities and temperature gradients at which the transition occurs.

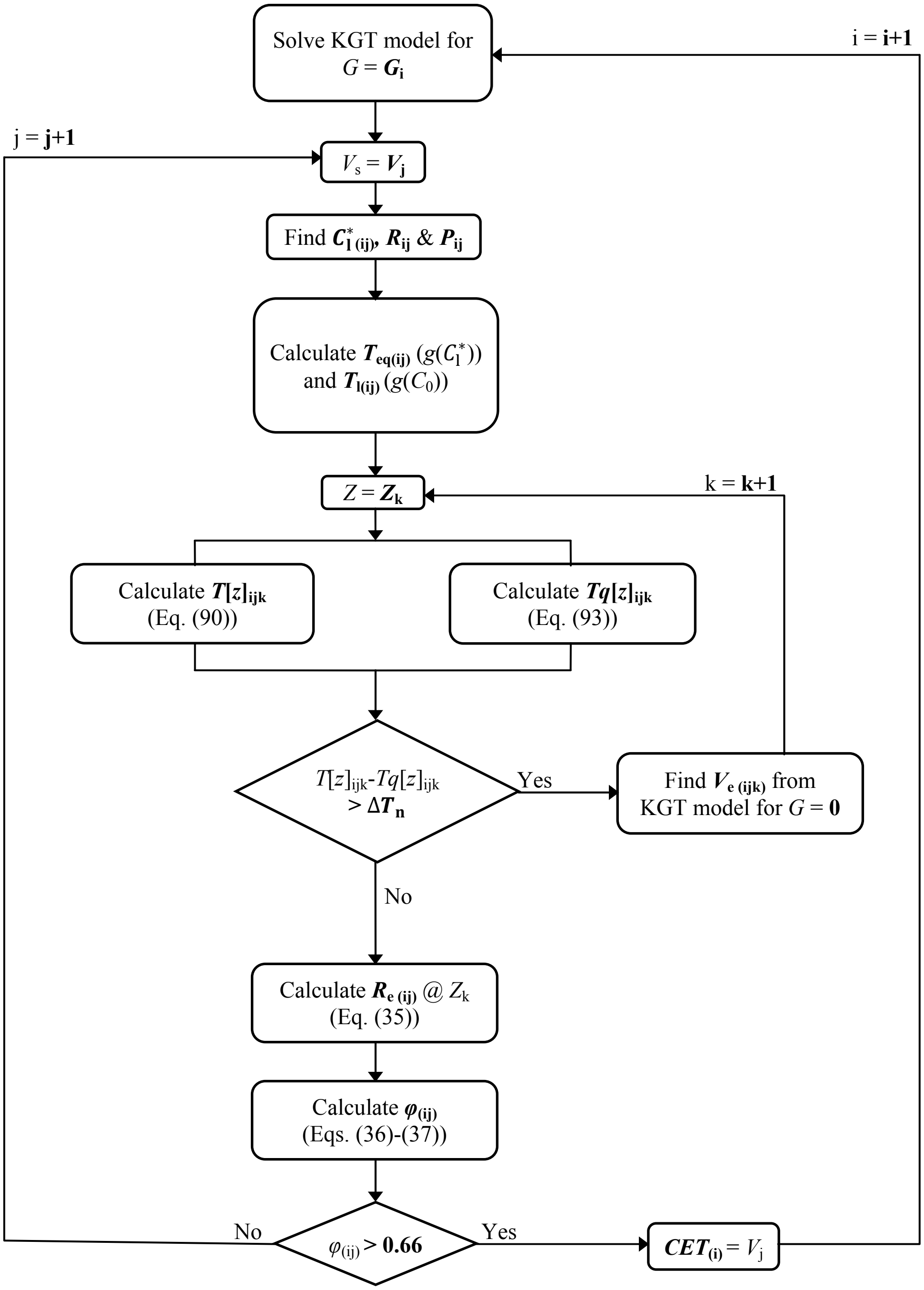

Fig. 24 Flowchart of the CET computation procedure based on the KGT model; index *i* denotes the *i*th *G* while the entire scheme is being repeated for different *G* values, index *j* indicates the *j*th V_s and index *k* represents different locations ahead of the columnar front.

4.2.4 CET evaluation in Ti-Nb alloys

Other than the variables specifically defined for CET such as N_0, ΔT_n and a_0, the parameters in the KGT model (i.e. c_0) can also affect the output of the CET computation. ΔT_n is shown to affect the CET only in the very low velocity-low temperature gradient regime [93] which is not of concern in laser powder deposition.

Fig. 25 shows the prediction of KGT model for the CET in Ti-rich TiNb alloys in terms of the local processing conditions and using the thermophysical properties given in Table 6. As can be seen in this figure, the higher Nb content the wider freezing range in the Ti-Nb phase diagram (referring to Fig. 15), thus the higher probability of equiaxed growth of dendrites (i.e. the larger equiaxed area). However, even with the highest Nb content tested in this study, i.e., 32wt.%, the typical range of process conditions for laser powder deposition falls entirely within the columnar region, shown as the shaded area in Fig. 25. Therefore, as can also be seen in the Fig. 21, it is very unlikely for the equiaxed microstructure to grow in the melt pool ahead of the advancing columnar dendrites. The solidification microstructure shown in Fig. 21 clearly depicts the dominance of columnar growth over the entire domain, although at different orientations.

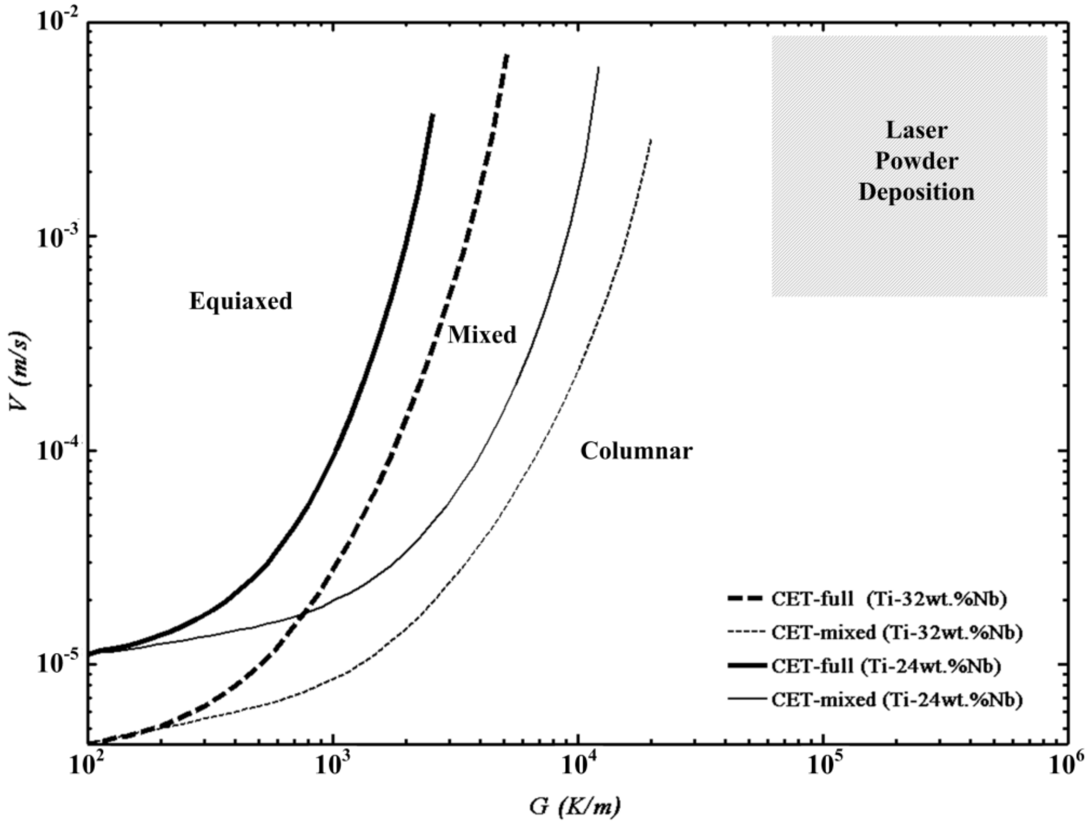

Fig. 25 The effect of c_0 on the CET (based on the KGT model) in solidification of Ti-rich Ti-Nb alloys. The curves CET-full separates the complete equiaxed structure from the mixed columnar-equiaxed, while the curves CET-mixed are the borders between the complete columnar and mixed columnar-equiaxed structures.

4.3 Summary

The dependency of the dendrite tip radius *R* on the local solidification parameters, V_s and *G*, was determined for Ti-rich Ti-Nb alloys using the classical theories of solidification, i.e., the so-called KGT model. The established R-V_s relationship will then be used to analytically verify the simulation output of the dendrite growth kinetics and the resultant morphologies. It was also shown that, at the strictly constrained solidification conditions present in laser powder deposition, the growth direction will be most likely along the normal to the interface. Finally, using the KGT model, the columnar-to-equiaxed transition (CET) was mapped onto the variations of the local solidification conditions, V_s and *G*. Considering the normal range of operating parameters in laser powder deposition, it was concluded that equiaxed growth of dendrites in the supper-cooled liquid ahead of the solidification front will be very unlikely to occur. In other words, the growth morphology will be fully columnar which can be also experimentally validated referring to the microstructure shown in Fig. 21.

Chapter 5:

Modeling and simulation of solidification microstructure

This chapter presents the mathematical derivation and numerical simulation of phase field equations based on minimization of the free energy functional for directional solidification of a dilute binary alloy. The time evolution of phase and concentration fields are presented for an optimized set of model parameters.

5.1 Phase field simulation

A detailed description of the derivation of phase field formulation for a dilute binary alloy is provided in Appendix A3. Since the liquidus slope and partition coefficient of Ti-rich Ti-Nb alloys are assumed constant, as previously discussed in Chapter 4, the formulation for dilute binary alloys still holds valid. The final set of phase and concentration fields with dimensionless parameters are developed here for the numerical simulation. The effect of phase field parameters, particularly the interface width, on the evolution of the dendrite structure is investigated both qualitatively and quantitatively. The competition for dendrite arm spacing selection in directional solidification is finally simulated with the optimum phase field parameters.

5.1.1 Phase field equations with dimensionless parameters

Time and space can be re-scaled by $\bar{t} = t/\tilde{\tau}(\theta)$ and $\bar{x} = x/W_\phi$ in order to characterize Eqs. (111)-(113), in Appendix A3, by the dimensionless parameters: $\hat{\lambda} = (1-k)^2 c_0^l \bar{\lambda}$, $\bar{D} \equiv D_L \tilde{\tau}(\theta)/W_\phi^2$, $\bar{c} = c/c_0^l$, $\bar{l}_T = l_T/W_\phi$, $\bar{V}_p = V_p \tilde{\tau}(\theta)/W_\phi$ and $\bar{z} = z/W_\phi$. Thus, these equations which are used for numerical treatment can be re-written as

$$\frac{\partial \phi}{\partial \bar{t}} = \nabla.\left(\widetilde{W}^2(\theta)\nabla\phi\right) - \partial_{\bar{x}}\left[\widetilde{W}(\theta)\widetilde{W}'(\theta)\partial_{\bar{y}}\phi\right] + \partial_{\bar{y}}\left[\widetilde{W}(\theta)\widetilde{W}'(\theta)\partial_{\bar{x}}\phi\right] - \tag{38}$$

$$\frac{\partial g(\phi)}{\partial \phi} - \frac{\hat{\lambda}}{(1-k)}\left(e^{\bar{u}} - 1 + \frac{\left(\bar{z} - \bar{V}_p \bar{t}\right)}{\bar{l}_T}(1-k)\right)\tilde{g}'(\phi) + \eta'\left(\vec{\bar{x}}, \bar{t}\right)$$

$$\frac{\partial \bar{c}}{\partial \bar{t}} = \nabla.\left(\bar{D}Q(\phi)\bar{c}\nabla\bar{u}\right) + \nabla.\left(a_t(1-k)\left(e^{\bar{u}} + \frac{\left(\bar{z}-\bar{V}_p\bar{t}\right)}{\bar{l}_T}(1-k)\right)\frac{\partial\phi}{\partial\bar{t}}\frac{\nabla\phi}{|\nabla\phi|}\right) \tag{39}$$

$$\bar{u} = ln\left(\frac{2\bar{c}}{[1+k-(1-k)h(\phi)]}\right) \tag{40}$$

Interpolation functions remain the same as those presented by Eqs. (114)-(117), in Appendix A3. It should be noted that in the final numerical procedure the dependence of the time scale on the anisotropy of interface is neglected, i.e., $\tilde{\tau}(\theta) = \tau$. Also, for simplicity, the stochastic noise term in Eq. (38), $\eta'\left(\vec{\bar{x}}, \bar{t}\right)$, is also taken as zero.

5.1.2 Numerical procedure

Eqs. (38)-(40) can be explicitly discretized using a finite volume scheme described in Sections 5.7 and 6.8 of ref. [42]. A set of processing parameters and thermophysical properties of the binary alloy is defined and relevant initial and boundary conditions are applied in the numerical scheme whose convergence can be controlled though manipulation of so-called phase field parameters. A finite volume code for isothermal alloy solidification provided by ref. [42] was modified for directional solidification.

5.1.2.1 *Phase field parameters*

Calculating the sharp interface parameters of Eqs. (38)-(40) while taking as reference the concentration on the liquid side of the interface $c_0^l = c_0/k$, the following criteria is obtained linking the sharp interface kinetics to that of the phase field for directional solidification [49].

$$\frac{c}{c_0^l} = 1 - (1-k)\kappa d_0 A(\theta) - (1-k)\frac{(z-V_p t)}{l_T} - (1-k)\beta v_n \tag{41}$$

where $d_0 = \Gamma/\Delta T_0$ is the solutal capillary length, $\Delta T_0 = |m_l|(1-k)c_0^l$ the freezing range, $\beta = 1/(\mu_k \Delta T_0)$ and μ_k the atomic mobility at the interface. β is negligible at low solidification rates. It is shown that with a particular $\hat{\lambda}$ (the inverse nucleation barrier), using the thin interface relations, a unique choice of W_ϕ and τ will be established such as to yield the same d_0 and β in the simulations [42,49]. The following equations are thus developed to map the diffuse interface kinetics to those of the sharp model using the coupling coefficient $\hat{\lambda}$.

$$d_0 = \frac{a_1 W_\phi}{\hat{\lambda}} \tag{42}$$

$$\bar{D} = a_2 \hat{\lambda} \tag{43}$$

$$\tau = \frac{\bar{D} W_\phi^2}{D_l} \tag{44}$$

where $a_1 = 0.8839$ and $a_2 = 0.6267$. The whole idea is to be able to establish a diffuse interface with unrealistically large width, W_ϕ, through selection of a reasonably large $\hat{\lambda}$, for the sake of numerical efficiency. However, the anti-trapping current, the second term on the right-hand side of Eq. (39), is introduced to self-consistently counter the effect of a large interface thickness to reproduce the material parameters d_0 and β.

5.1.2.2 *Initial and boundary conditions*

The dimensionless grid space and time step are chosen as $\Delta\bar{x} = 1$ and $\Delta\bar{t} = 0.02$, respectively. A solid seed is introduced at the bottom of domain with the locus of interface center points randomly varying in the range of (50±10)$\Delta\bar{x}$. The initial order parameter field $\phi_{initial}$ is then defined on two sides of the interface using the function "tanh $(z'/\sqrt{2})$" assigning values from $\phi = 1$ on the solid part to $\phi = -1$ on the liquid part along the normal to the interface. The initial dimensionless concentration field $\bar{c}_{initial}$ can be assigned using the existing order parameter field and a predefined supersaturation $\widetilde{U}$ (taken 0.55 in this study) along with Eq. (40), knowing that

$$e^u = 1 - (1-k)\widetilde{U} \tag{45}$$

Thus,

$$\bar{c}_{initial} = 0.5\big((1+k) - (1-k)\phi_{initial}\big)e^u \tag{46}$$

For both the order parameter and concentration fields, all boundaries are considered adiabatic (i.e., zero-flux boundaries). The thermal gradient is directed from bottom to top with the temperature of steady-state growth (i.e., that belonging to the liquid composition $c_0^l = c_0/k$) as the reference temperature located at vicinity of the initial solid-liquid interface. The change in temperature by time marching is considered only along the y-axis so as to represent the pulling velocity of the sample through the thermal gradient field in the same direction only.

5.2 Cellular automaton (CA) simulation

In the following sections, the mathematical basis and the latest developed numerical procedure for the cellular automaton method are described.

5.2.1 Mathematical formulation

The mathematical basis includes the solution of the heat and solute conservation equations for an aggregate system of solid and liquid at a given transformation time.

5.2.1.1 *Heat conservation*

In columnar growth of alloys, the temperature field has a uniform gradient moving at a constant pre-set velocity. One can neglect the effect of the latent heat release on the solidification process [32, 96]. This assumption is reasonable since, in constrained solidification, heat is moving out through the solid phase with a much higher diffusivity than that of the solute being rejected into the liquid ahead of the interface [1].

5.2.1.2 *Solute conservation*

The solute conservation equation is solved for solid and liquid separately and a boundary condition is set at the S/L interface to link the solution in two phases:

$$\frac{\partial C_i}{\partial t} = D_i \left(\frac{\partial^2 C_i}{\partial x^2} + \frac{\partial^2 C_i}{\partial y^2} \right) \tag{47}$$

where C is the composition; the subscript i denotes solid or liquid; and D_i is the diffusion coefficient. Constant composition boundary condition is kept at low and high temperature boundaries (i.e. the bottom and top boundaries) while the boundaries along the growth direction are periodic.

The S/L interface is not known a priori and is calculated as a part of the solution. Since equation (47) involves second order spatial derivations, two boundary conditions are required. The first one is obtained through the assumption of thermodynamic equilibrium at the S/L interface which relates its temperature and composition to the local undercooling including the thermal, solutal and curvature components:

$$T_t = T_l^{eq} + (c_l^* - c_0)m_l - \Gamma \kappa f(\varphi, \theta) \tag{48}$$

The equilibrium concentration at the interface is therefore calculated as follows:

$$c_l^* = c_0 + \frac{T^* - T_l^{eq}}{m_l} + \frac{\Gamma \kappa f(\varphi, \theta)}{m_l} \tag{49}$$

where T_l^{eq} is the equilibrium liquidus temperature at the initial composition, c_0. m_l is the slope of the liquidus line. Γ is the Gibbs-Thomson coefficient, κ is the interface curvature and $f(\varphi, \theta)$ is the function representing the anisotropy of the surface tension, based on the difference between the angle of preferential growth direction, θ, and the angle of the normal to the interface, φ, with respect to a reference axis. Asterisks denote values at the S/L interface.

The interfacial energy γ for cubic crystals with a four-fold symmetry can be expressed as [56]:

$$\gamma(\varphi, \theta) = \gamma_0 . \psi(\varphi, \theta) \tag{50}$$

$$\psi(\varphi, \theta) = 1 + \varepsilon \cos[4(\varphi - \theta)] \tag{51}$$

where ε is the amplitude of the anisotropy of the surface tension. According to the Gibbs-Thomson equation, $f(\varphi, \theta)$ in Eq. (48) can be calculated as follows:

$$f(\varphi, \theta) = \psi(\varphi, \theta) + \frac{\partial^2}{\partial \varphi^2} \psi(\varphi, \theta) = 1 - \delta \cos[4(\varphi - \theta)] \tag{52}$$

where $\delta = 15\varepsilon$.

The second boundary condition is the conservation of solute on the moving S/L interface:

$$V_n(c_l^* - c_s^*) = \left[-D_l \left(\frac{\partial c_l}{\partial x} + \frac{\partial c_l}{\partial y} \right) + D_s \left(\frac{\partial c_s}{\partial x} + \frac{\partial c_s}{\partial y} \right) \right] . \vec{\mathbf{n}} \tag{53}$$

where V_n is the interface normal velocity and $\vec{\mathbf{n}}$ the interface normal vector.

The local equilibrium at the S/L interface requires a solute redistribution on its both sides with the equilibrium partition coefficient k:

$$c_s^* = k c_l^* \tag{54}$$

Equation (54) links the solutions of equation (47) according to the given boundary conditions (i.e. equations (48) and (53)).

5.2.2 Numerical solution

The computational domain is spatially resolved into square cells with the side length, *a*, small enough to reveal the desirable dendritic features. Following the Cellular Automaton (CA) method, each cell holds the values of local temperature, composition and solid fraction contributing to the global solution of the transport equations. The evolution of these values is also controlled by a set of pre-defined transition rules. A detailed report on the latest and most commonly used numerical methods for the solution of conservation equations as well as the tracking method of the interface motion is provided in Appendix A4.

Fig. 26 shows the general algorithm representing the cellular automata-finite difference scheme for simulation of directional solidification in alloys. The simulation sequences indicated in this algorithm are executed repeatedly until a pre-set solidification time, t_s, is reached.

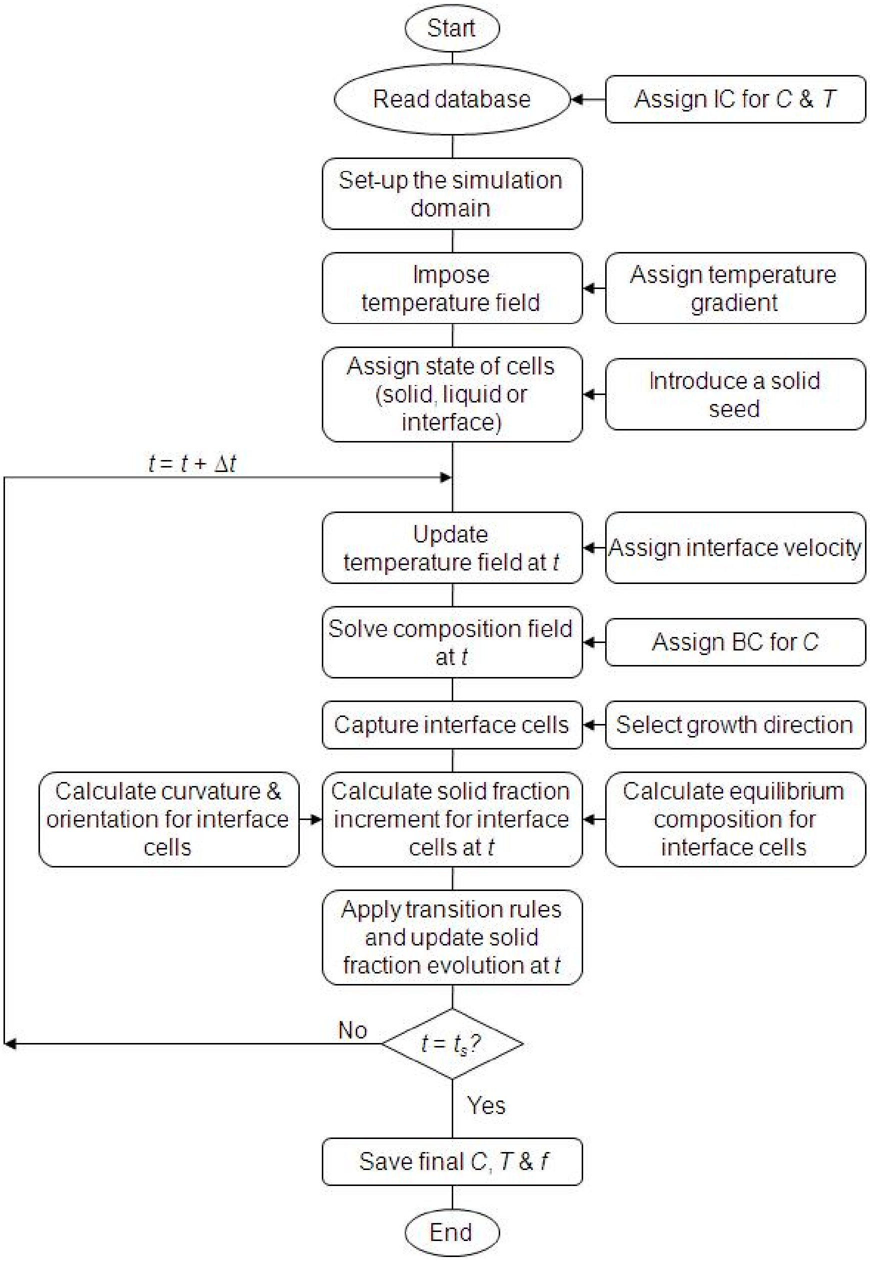

Fig. 26 Cellular automata-finite difference algorithm for dendrite solidification.

5.3 Model evaluation

Since the phase field method is shown to be the most quantitatively reliable method [41, 42, 49], the model validation procedure is only carried out for the phase field method. The CA methods are however faster and are powerful tools when only used for qualitative analysis of solidification microstructures. This way, the final output of CA simulations will be presented only for comparison.

The accuracy of the developed phase field model is evaluated for the directional solidification of Ti-32wt.%Nb under two different processing conditions corresponding to points 2 and 5 of the microstructure shown in Fig. 21. The thermophysical properties of the alloy and the local processing conditions of the two points, namely the temperature gradient and the pulling velocity, are listed in Table 7. An important factor is the ability of model to predict the steady state directional growth of dendrites at a fixed temperature gradient and pulling velocity. For this purpose, the concept of stability parameter developed by Terivedi and Kurz [56] is used to correlate the model with the experimental/analytical criterion. The effect of the interface width, chosen as wide as the smallest grid size of the system, on the prediction accuracy of the morphological features and the steady state dendrite tip radius is studied to determine the mesh size dependency of the model. Also, predictions of the KGT model are used to validate the R-V relationship until the system has reached steady state.

Table 7 Thermophysical properties and processing conditions of Ti-32wt.%Nb alloy.

m_l (K/wt.%)		5
c_0 (wt.%)		32
k		1.25
D_l (m^2 s^{-1})		6.5×10^{-9}
D_S (m^2 s^{-1})		6.5×10^{-13}
Γ (K m)		1.941×10^{-7}
ϵ_4		0.03
V_p (m s^{-1})	Point 2	0.0062
	Point 5	0.0005
G (K m^{-1})	Point 2	2.5×10^5
	Point 5	5.0×10^5

5.3.1 Stability parameter

Using the concept of marginal stability [56, 90], the modern theories of dendrite growth established a uniquely defined steady state tip velocity and radius as a function of melt undercooling. This concept was derived from stability analysis of an SL interface advancing at steady state. The stability criterion was established using a perturbation analysis of an interface of initial conditions corresponding to the steady state, mainly shape, composition, velocity and temperature. The perturbation technique mathematically introduces the effect of time dependency into the shape of the interface, which otherwise moves at a constant velocity. It was shown that at steady state, the dendrite tip can be approximated by a paraboloid of revolution whose radius is a function of composition, temperature gradients, capillarity and the stability parameter σ^* [56]. This parameter has been experimentally and theoretically determined to be around 0.02 [55, 90, 97]. This value is obtained when theory and experiments are in agreement and is a constant only when the system is isotropic.

The following expression for the stability parameter is obtained by Langer and Muller-Krumbhaar [97]

$$\sigma^* = \frac{2d_0 D_l}{V_n R^2} \tag{55}$$

where d_0 is the capillarity length defined as

$$d_0 = \frac{\Gamma f(\varphi,\theta)}{m_l c_l^*(k-1)} \tag{56}$$

Therefore,

$$\sigma^* = \frac{2D_l \Gamma f(\varphi,\theta)}{V_n R^2 m_l c_l^*(k-1)} \tag{57}$$

At steady state where the tip composition c_l^*, radius R and normal velocity V_n are fixed, and at a given crystallographic orientation φ, the stability parameter is a constant value. This parameter can be used to define the steady state of the simulated dendritic features and is expected to approach the experimental and theoretical value of 0.02 as the system becomes steady. However, the present model does not need the concept of marginal stability to uniquely define dendritic features at non-steady and steady conditions. The role of the stability parameter is contained in the model, but the simulation process itself determines its value throughout a transient analysis of solute diffusion without assuming a pre-established shape for the dendrite tip or the dendrite in general. Unlike the classic theories of dendrite growth, the variations in shape are reflected in the solution including the time dependency.

5.3.2 Mesh dependency

The ratio of W_ϕ / d_0 whose changes represent the alteration of coupling factor $\hat{\lambda}$, is chosen as the main tool for numerical experimentation of the developed phase field model. The following table summarizes different sets of numerical properties of the phase field model.

Table 8 Conditions for numerical experimentation.

Test#	W_ϕ (m)	nx×ny	d_0 (m)	W_ϕ/d_0
1	1.50×10^{-7}	400×400	1.50×10^{-8}	10.00
2	1.25×10^{-7}	400×400	1.50×10^{-8}	8.33
3	1.00×10^{-7}	500×500	1.50×10^{-8}	6.67
4	0.90×10^{-7}	500×500	1.50×10^{-8}	6.00
5	0.80×10^{-7}	600×600	1.50×10^{-8}	5.33
6	0.70×10^{-7}	700×700	1.50×10^{-8}	4.67
7	0.60×10^{-7}	800×800	1.50×10^{-8}	4.00
8	0.50×10^{-7}	1000×1000	1.50×10^{-8}	3.33

The meshing system is rectangular-based and adaptive which distributes the cell size from the finest $dx = W$ near the interface to the coarsest $dx = 8 \times W$ away from the interface. The total size of the system $nx\times ny$ was chosen so as to yield the same actual size of the sample as those of test 1. Therefore, by choosing the finest mesh possible, the change in the overall size of the system can be simply correlated to the change in the interface width as follows

$$(nx, ny)_{\text{test2}} = (nx, ny)_{\text{test1}} \left(\frac{(W_\phi/d_0)_{\text{test1}}}{(W_\phi/d_0)_{\text{test2}}}\right) \tag{58}$$

Artificial solute trapping for thinner interfaces is weaker. It causes a more effective solute rejection in the liquid in front of the advancing interface, thus more closely resembling the sharp interface kinetics. Therefore, in theory, the thinner interface the more accurate the results will be. However, as can be inferred from the following equation, the computational cost dramatically increases by reducing the interface width below a certain value. Considering Eqs. (42)-(62), the overall simulation time can be correlated to the chosen interface width as

$$(t_{total})_{\text{test2}} = (t_{total})_{\text{test1}} \left(\frac{(W_\phi/d_0)_{\text{test1}}}{(W_\phi/d_0)_{\text{test2}}}\right)^3 \tag{59}$$

On the other hand, the solution of the developed phase field model becomes unsteady for $\frac{W_\phi}{d_0} > \approx 10$, returning no output. In this study, in order to determine the largest possible interface width by which a reasonable accuracy can be achieved, a numerical experimentation was designed. As shown in Table 8, a series of simulations are performed for the same thermophysical properties and processing conditions given in Table 7, differing only in the value of interface width. The final mesh resolution will then be selected by tracking the changes in the simulated morphological features and also checking the growth kinetics with the help of analytical models of dendritic growth, i.e., the KGT model.

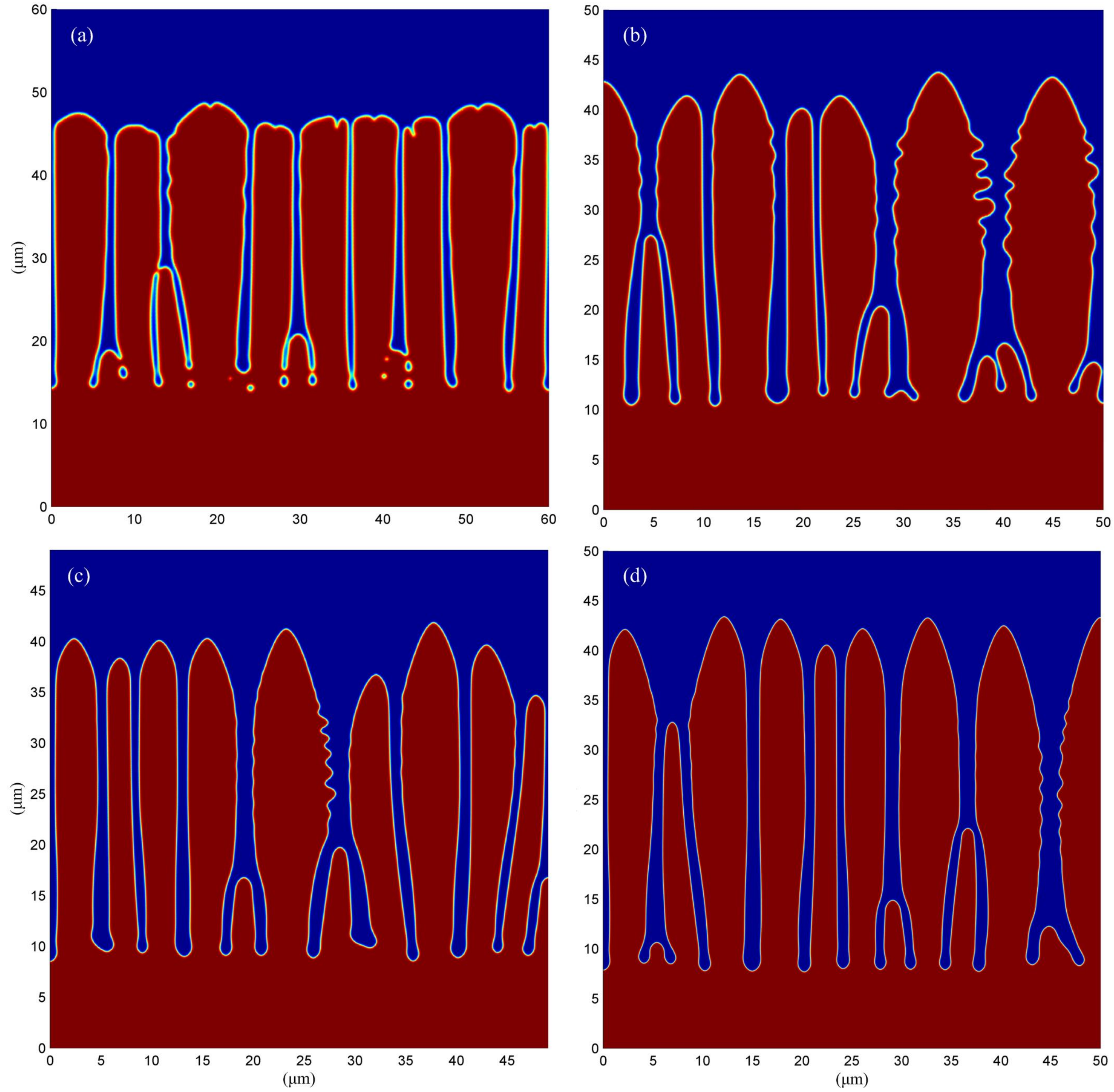

Fig. 27 The effect of interface width on morphological features in directional growth of dendrites of Ti-32wt.%Nb alloy under conditions given in Table 7 and Table 8; (a) W_ϕ=1.5×10^{-7} m, (b) W_ϕ=1.0×10^{-7} m, (c) W_ϕ=0.7×10^{-7} m and (d) W_ϕ=0.5×10^{-7} m.

Fig. 27 shows how the width of interface in phase field simulations affects the order parameter field and thus the clarity in prediction of dendritic morphological features such as the primary and secondary arm spacing. For W_ϕ=1.5×10^{-7} m, as shown in Fig. 27(a), the system does not even approach a steady state solution for the dendrite tip morphology. Reducing the interface width down to 0.7×10^{-7} m (Fig. 27(c)) shows an increase in clearance between the dendrite arms and also a visible reduction in the growth magnitude of the secondary arms. However, no significant change in these features can be observed by further decreasing the interface width to 0.5×10^{-7} m, as indicated in Fig. 27(d).

To investigate the effect of interface width on the growth kinetics, the steady state tip radius R for a given set of processing conditions, i.e., the temperature gradient G and the pulling speed V_p, was compared with the analytical value found with the KGT model. Referring to the prediction of the KGT model in Fig. 23, the equilibrium tip radius for the conditions given in Table 7 is ~5×10^{-7} m, which is shown as a straight line in Fig. 28. The tip radius for the dendritic structures simulated with each interface width was averaged over the number of primary dendrite arms growing at steady state within the simulation domain. It was simply found through fitting the largest possible circle onto the dendrite tips shown in Fig. 27. Fig. 28 indicates that, reducing the interface width, the simulated tip radius becomes smaller approaching the analytical value predicted by the KGT model. Furthermore, sharpening the interface to a width below ~0.08 µm, will cause no significant change in the simulated steady state dendrite tip radius.

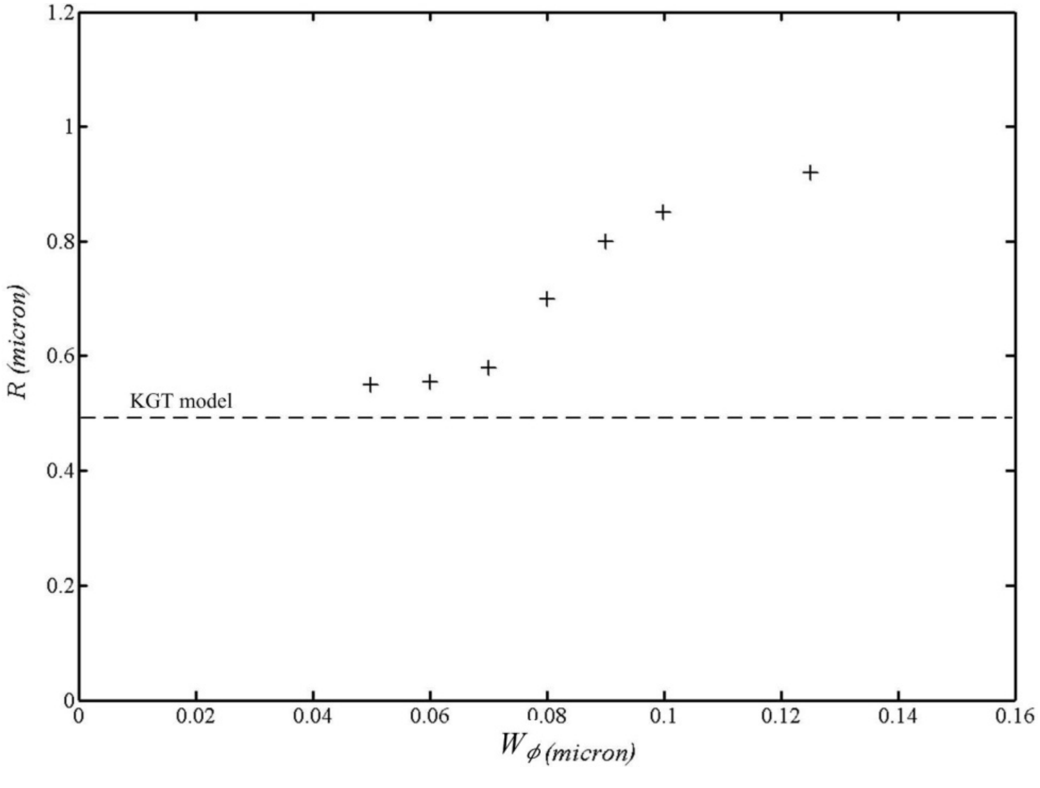

Fig. 28 Steady state tip radius for simulations with various interface width values; The straight line represents the prediction of KGT model for solidification of Ti-32wt.%Nb under conditions given in Table 7.

Therefore, considering the accuracy in prediction of morphological details (referring to Fig. 27) and also the degree to which the interface width affects the simulated steady state tip radius (as shown in Fig. 28), interface width of 0.7×10^{-7} m is selected for the entire study. With this resolution in defining the SL interface, not only the accuracy of the simulation stays reasonably close to that of the finest resolution tested, i.e., 0.5×10^{-7} m, but also the computational costs fall within an acceptable range for the domain sizes used in the study.

5.3.3 Validation of growth kinetics

In the microstructure shown in Fig. 21, the local solidification conditions of two points, one from the top and one from the bottom, i.e., points 2 and 5 respectively, are extracted from the thermal model. The validity of the simulated kinetics of dendrite growth until steady state is examined with the analytical predictions of the KGT model shown in Fig. 23. Interestingly, as also indicated in Fig. 29, the R-V_s relationship is hardly affected by the temperature gradients in the range of 2.5×10^{-5} - 5×10^{-5} K m^{-1}, and at the tip velocities greater than ~10^{-4} m s^{-1}. Therefore, considering the local solidification conditions, the microstructures corresponding to the points 2 and 5 should follow the same analytical R-V_s relationship based on the KGT model, but ending at different steady state velocities, as denoted by the arrows in Fig. 29. Also included in this figure is the R-V_s relationship simulated by the phase field model for solidification of point 2 until steady state. For this curve, the tip radius and velocities are averaged over the number of dendrites growing at a number of given total solidification times, such as those whose developed microstructures are shown in Fig. 30. As can be seen, there is a good agreement between the simulation and the KGT model predictions.

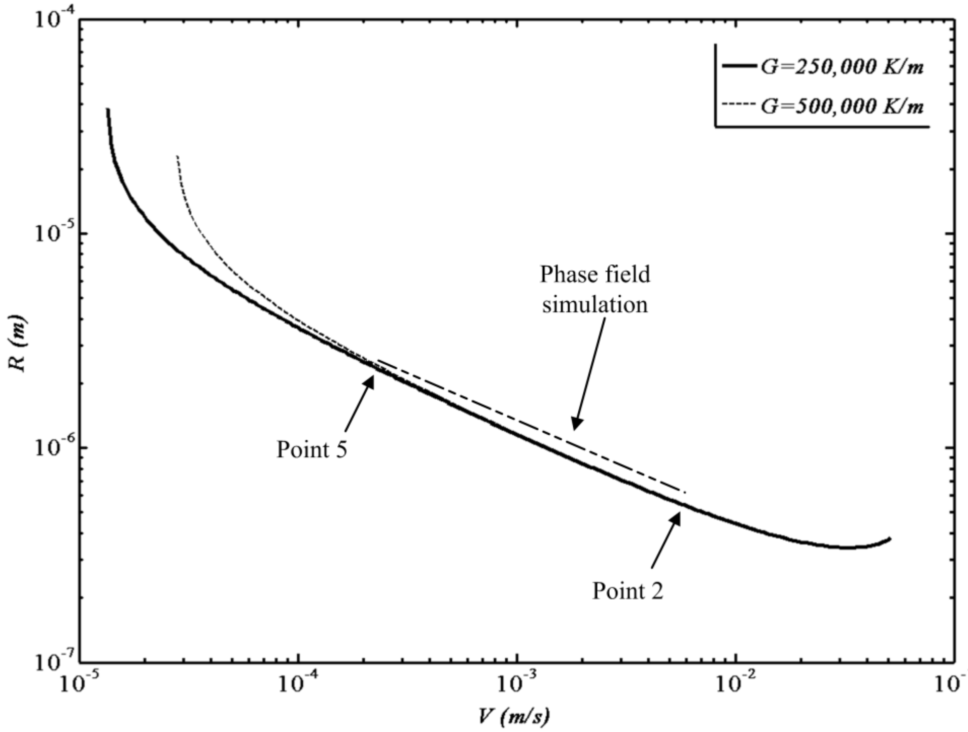

Fig. 29 Comparison between simulated and analytical R-V_s relationship for solidification of Ti-32wt.%Nb alloy under conditions given in Table 7.

Fig. 30 shows the developed microstructures at different overall solidification times from the early stages up to the steady state growth of Ti-32wt.%Nb alloy under conditions corresponding to those of point 2. The morphological features in this figure can be distinguished by the simulated normalised concentration field, i.e., c/c_0. According to Eqs. (42)-(62), the overall solidification time at a given number of iterations nt is calculated as follows

$$t_{total} = \bar{t} \times \tau \tag{60}$$

where the dimensionless time $\bar{t}$ and the system time scale τ are given as

$$\bar{t} = dt \times nt \tag{61}$$

$$\tau = \frac{\mathrm{a}_2 \mathrm{a}_1 W_{\phi}^3}{d_0 D_l} \tag{62}$$

where dt is the dimensionless simulation time step which is taken as 0.02 for the entire study. The straight lines drawn in Fig. 30 (c) and (d) represent the locations of the solidus line for Ti-32wt.%Nb alloy. The fixed position of the solidus line from the dendrites tip after t_{total} = 0.0281 s is an indication of growth at steady state yielding a stable dendrite length in the system.

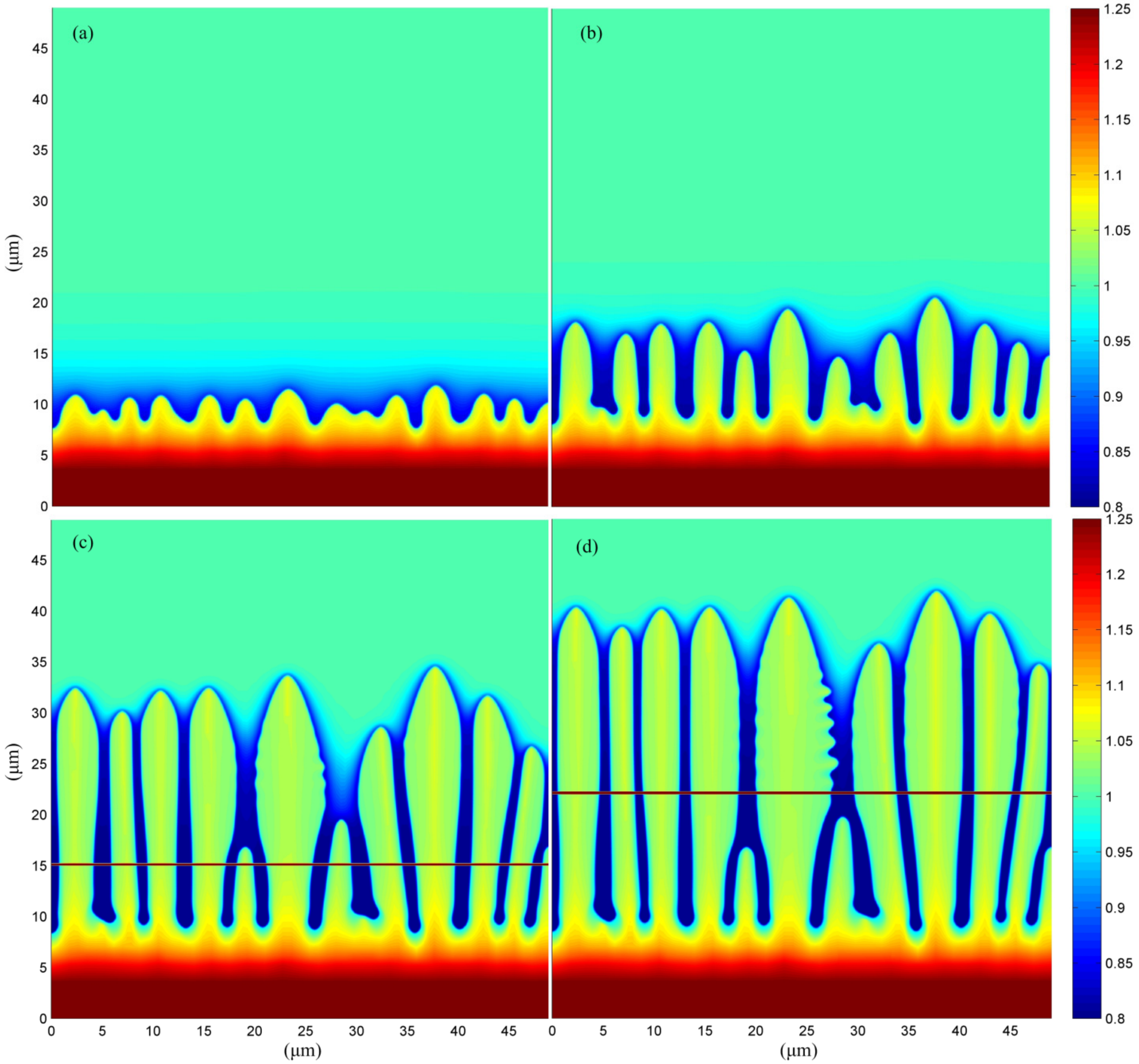

Fig. 30 Phase field simulations for the normalised concentration filed at different solidification times until steady state directional growth of dendrites in Ti-32wt.%Nb alloy; (a) t_{total} = 0.0211 s, (b) t_{total} = 0.0253 s, (c) t_{total} = 0.0281 s and (d) t_{total} = 0.0296 s; The straight lines represent the locus of the alloy solidus temperature (simulation parameters: W_{ϕ}=0.7×10^{-7} m, τ=7.0371×10^{-6} s)

5.4 summary

The mathematical formulation and solution strategies were presented for the numerical procedures of the two well-known methods of microstructure modelling, phase field and cellular automaton. The developed phase field model for directional solidification, which is the most accurate one, was then evaluated for the steady-state growth conditions, mesh size dependency and the growth kinetics. It was shown that the concept of stability parameter is inherently considered in the development of the mathematical basis of the phase field model. Moreover, the simulation results of directional solidification at constant G and V_s

showed that the dendrites always approach the steady-state growth kinetics. Analysis of mesh size dependency for the most severe growth conditions, i.e., the conditions present at the finest region of the microstructure, indicated that reducing the interface width W_ϕ to a value below 0.7×10^{-7} m does not significantly affect the quality of morphological features and the growth kinetics. Finally, the growth kinetics of dendrites until steady-state was validated using the analytical R-V_s relationship found using the KGT model. It was shown that the variations of dendrite tip radius until steady state growth, estimated from the phase field model, remarkably matches the analytical predictions of the KGT model for the corresponding local parameters, V_s and G, of the two selected locations in the microstructure shown in Fig. 21.

Chapter 6:

Application of solidification model to laser powder deposition

The solidification model is used to investigate the effect of local solidification parameters, i.e., V_s and G, on the spacing evolution of dendrites in laser powder deposition of Ti-Nb alloys. The ability of the model is tested to predict the formation of microporosity as well as to explain the mechanisms involved. Finally, the developed model is employed to simulate the transient growth of dendrites using the temporal temperature distribution previously obtained from the thermal analysis.

6.1 Spacing characterization

Spacing characterization is done locally at constant temperature gradients and solidification velocities present in some selected locations in the microstructure shown in Fig. 21. The effect of the width of simulation domain on the spacing evolution is investigated to determine the smallest applicable width over which the spacing may not be affected. The simulation results for dendrite spacing evolution are compared with the experimental observations. It is also qualitatively compared with the predictions of an existing analytical/experimental model.

6.1.1 Effect of system size

The boundary conditions can affect the simulated dendrite arm spacing if the system size is not chosen large enough so as to realistically consider the finite size of a single grain in the microstructure [49]. However, on the other hand, the computational cost drastically increases with the system size. Therefore, the most convenient system (or grain) size with which a stable dendrite arm spacing can be simulated is to be estimated. According to the microstructure shown in Fig. 21, the finite grain size varies along the height due to the differences in the local solidification conditions, G and V_s. Therefore, the appropriate system size will be different for the upper part of the melt-pool, i.e., at point 2, from the bottom part, i.e., at point 5. Phase field simulations are performed for these two points with constant control parameters in order to find their effective system sizes. The simulated local solidification conditions of the points are listed in Table 9.

Table 9 Local solidification conditions of points 1 to 5 of the microstructure shown in Fig. 21.

#point	G (K m^{-1})	V_s (m s^{-1})
1	1.0×10^5	0.00667
2	2.5×10^5	0.00620
3	4.0×10^5	0.00550
4	4.5×10^5	0.00250
5	5.0×10^5	0.00050

Fig. 31 and Fig. 32 show the dendrite arm spacing evolution simulated for points 2 and 5, respectively, at some selected system sizes. Also, the variations of the steady state dendrite arm spacing simulated by various sample widths are shown in Fig. 33. The results indicate that the boundary effects are negligible for the range of sample widths tested, especially for widths greater than 50 μm and 150 μm for points 2 and 5 respectively. Looking more closely into the microstructure shown in Fig. 21, it can be observed that the average finite grain size is hardly over 100 μm for areas around points 1 to 4, while it gets as high as ~ 200 μm in the region around point 5 (i.e., at the bottom of the melt-pool). Therefore, the simulation of spacing evolutions for the middle and top parts of the microstructures (points 1 to 4) is carried out using the finite system width of 100 μm. Only for point 5, the system width is taken as 150 μm.

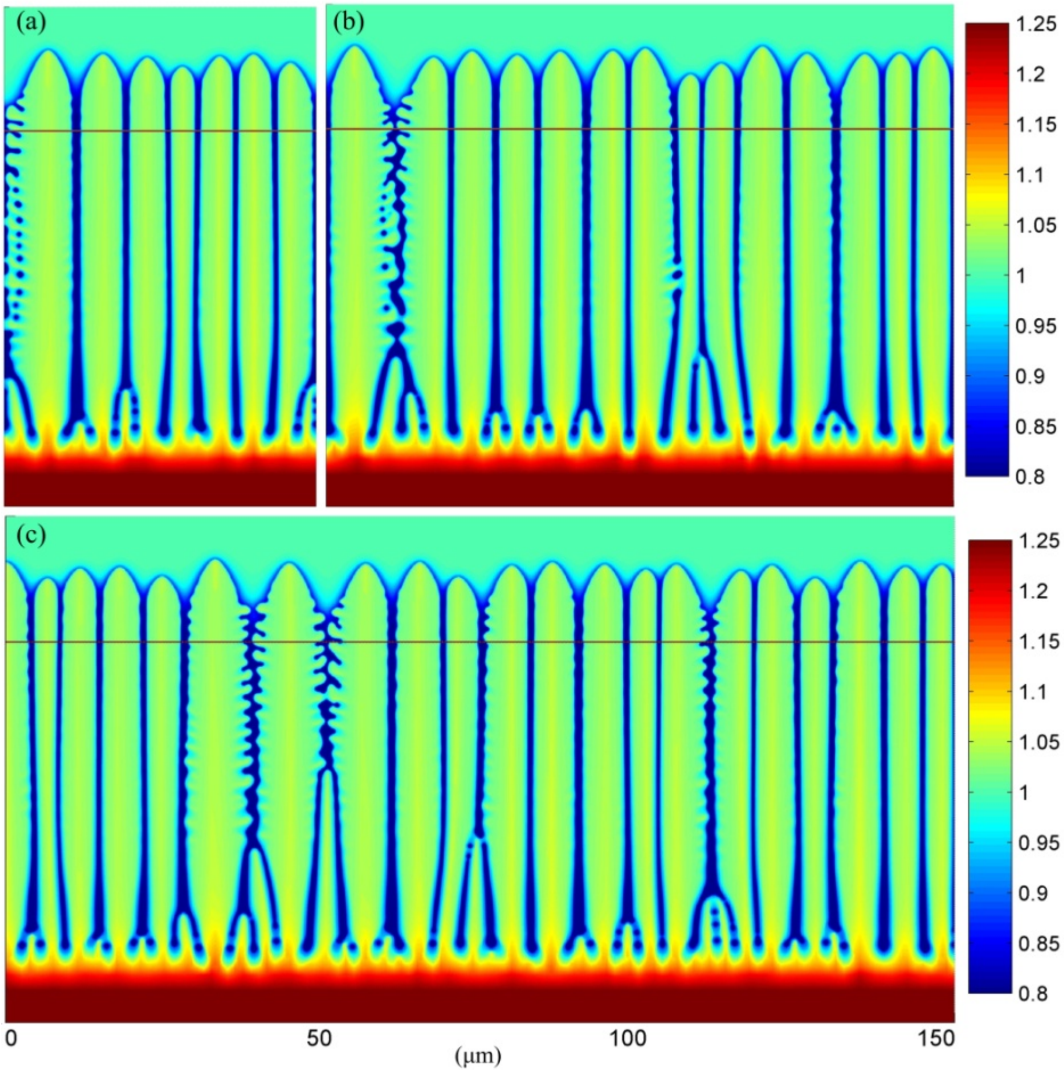

Fig. 31 Simulated dendrite arm spacing evolution for point 2 of the microstructure shown in Fig. 21 at system sizes (a) 50×80 μm, (b) 100×80 μm and (c) 150×80 μm; The straight lines are the imposed solidus temperatures and the colour contrast shows the normalised concentration field.

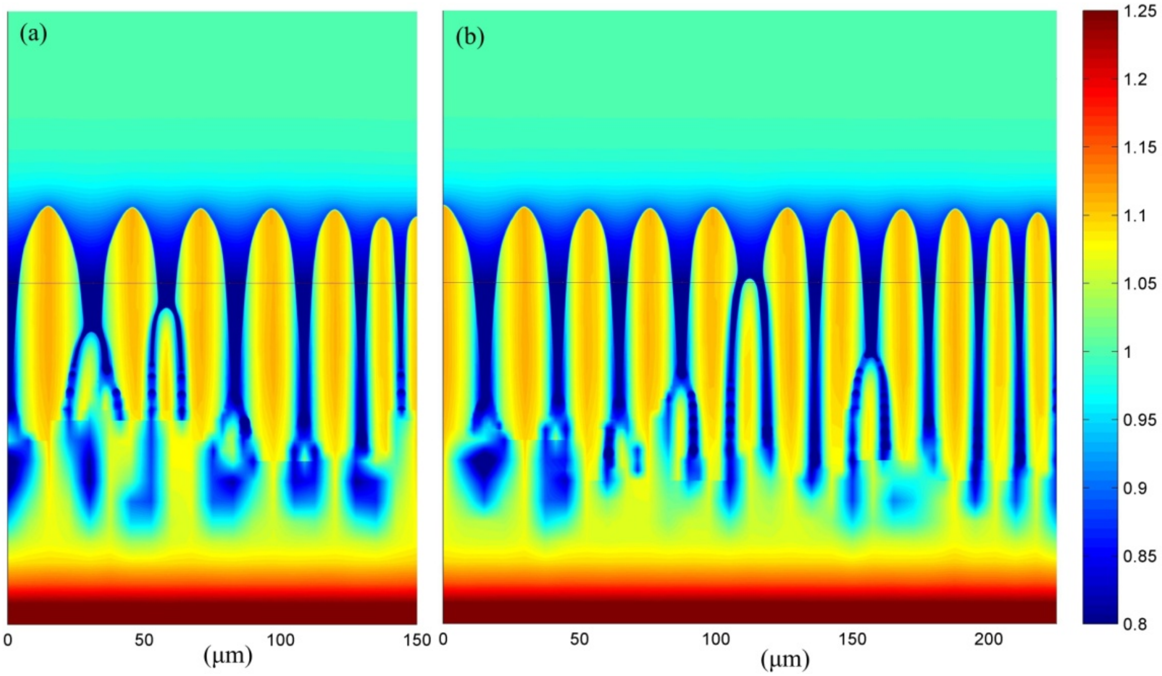

Fig. 32 Simulated dendrite arm spacing evolution for point 5 of the microstructure shown in Fig. 21 at system sizes (a) 150×225 μm and (b) 225×225 μm; The straight lines are the imposed solidus temperatures and the colour contrast shows the normalised concentration field.

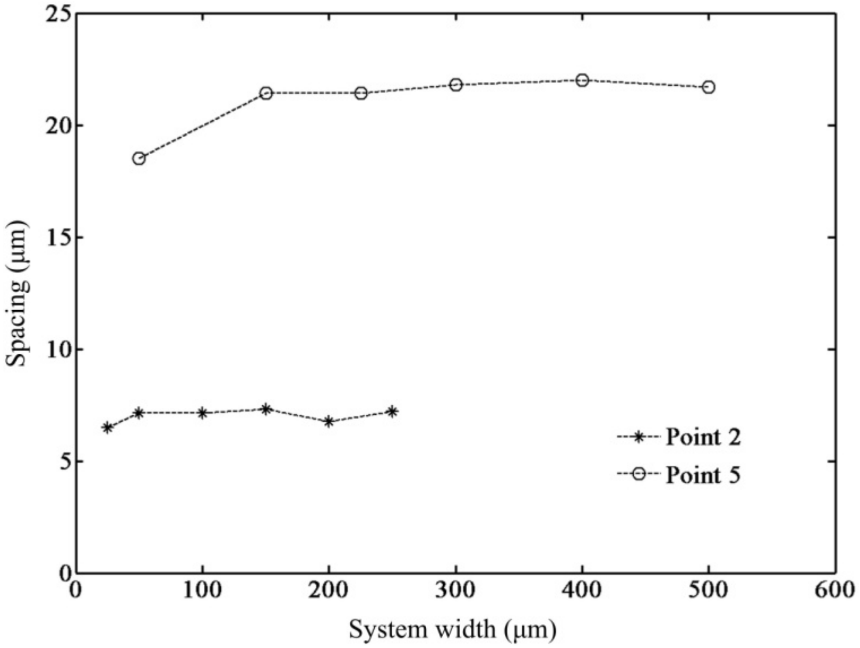

Fig. 33 Steady state dendrite arm spacing vs. transverse sample width for simulated for the solidification conditions points 2 and 5 of the of the microstructure shown in Fig. 21.

6.1.2 Dendrite spacing evolution

The evolution of the dendrite arm spacing of the points denoted on Fig. 21 is simulated considering the local processing conditions extracted from the thermal model (Table 9). The growth conditions are assumed to be constant locally with respect to the size of the simulation domain and a single grain of dendrites in the microstructure. In this case, the pulling speed becomes as large as the front velocity once the initial transient is over and dendrites grow at steady state. Fig. 34 and Fig. 35 depict the simulated dendrite structures along with the sample images taken at the corresponding locations denoted on the microstructure shown in Fig. 21. The comparison between the averaged experimental and simulated dendrite arm spacing is shown in Fig. 36.

The experimental values are averaged over at least 5 different spots along the same height from the melt-pool bottom. A remarkable agreement can be observed between the experiment and simulations both quantitatively and qualitatively. There is a minimum spacing at the mid-height of the microstructure which can be explained by the mutual effects of the front velocity and the temperature gradient as moving towards the top of the melt-pool. This behaviour may be also predicted using the following experimentally developed formula by Hunt [27] for the dependence of primary arm spacing λ_1 on the local solidification conditions, i.e., constant V_s and G, and on the alloy thermophysical properties.

$$\lambda_1 = 2.83(k\Delta T_0 D\Gamma)^{0.25} V_s{}^{-0.25} G^{-0.5} \tag{63}$$

Referring to Fig. 18 and Fig. 19, as one moves towards the top of the melt-pool along the SL interface, the temperature gradient G decreases by about one order of magnitude, while the front velocity V_s increases from zero up to the process speed V_L. According to the above equation, the former favours larger primary spacing while the latter does the opposite, thus introducing a minimum spacing around the mid-height of the structure.

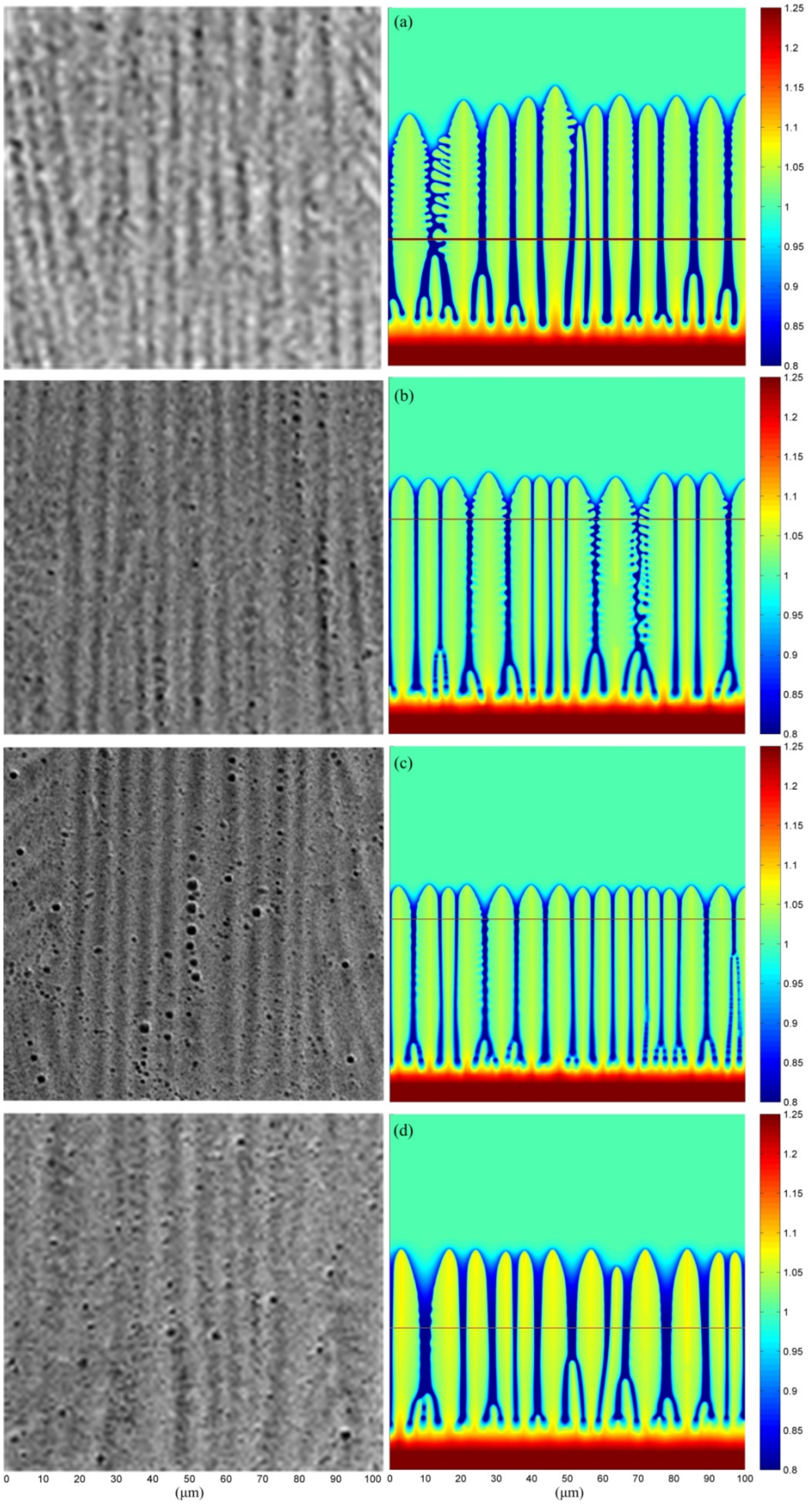

Fig. 34 Dendrite arm spacing evolution simulated locally for upper part of the microstructure shown in Fig. 21; (a) Point 1, (b) Point 2, (c) Point 3 and (d) Point 4; The straight lines are the imposed solidus temperatures and the colour contrast shows the normalised concentration field.

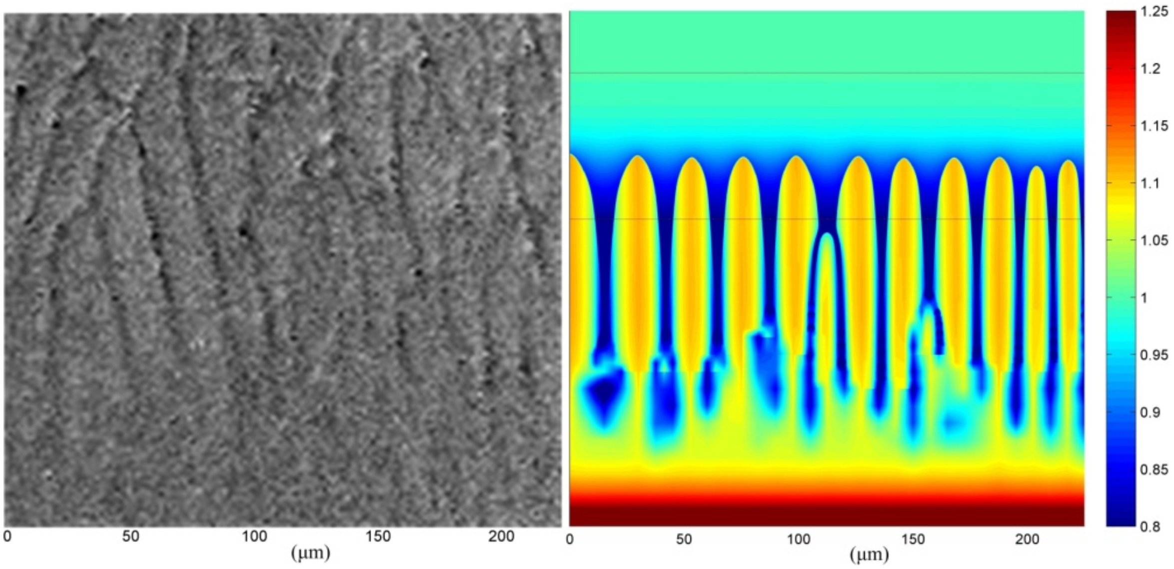

Fig. 35 Dendrite arm spacing evolution simulated locally for the lower part (point 5) of the microstructure shown in Fig. 21; The straight lines are the imposed solidus (lower one) and liquidus (upper one) temperatures and the colour contrast shows the normalised concentration field.

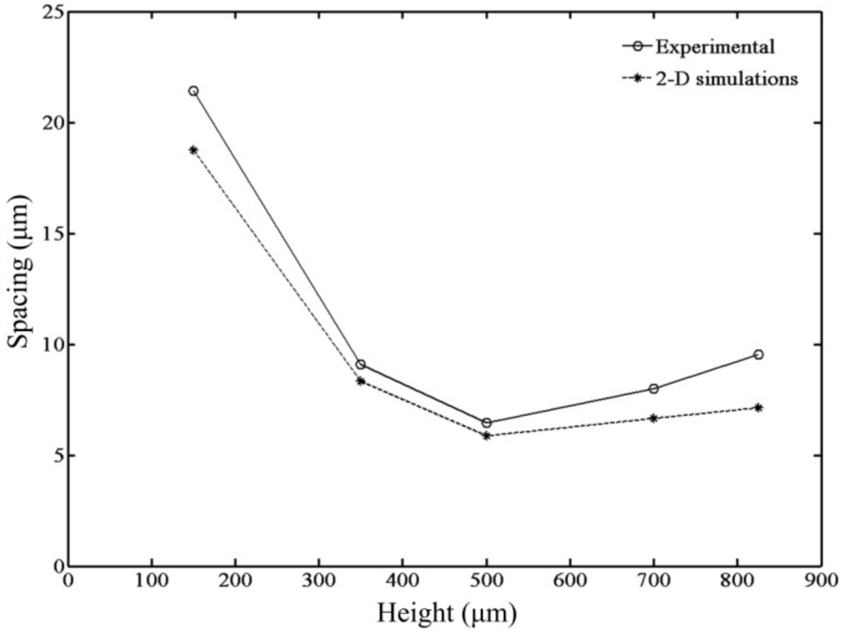

Fig. 36 The experimental and simulated average dendrite arm spacing vs. the distance from the melt-pool bottom.

6.2 Evaluation of microporosity

Microporosity is a defect which can be produced in solidification due to two main concomitant phenomena during the process: solidification shrinkage and gas segregation. By means of numerical and analytical models, it has been shown that the solid fraction per unit area and the secondary dendrite arm spacing (SDAS) are the two major factors controlling the state of the pores during solidification [98, 99].

The larger the solid fraction, the thinner is the liquid channel through which the pores have to pass in order to be released. This is equivalent to the conditions where smaller primary arm spacings exist. The release of pores is constrained where smaller SDAS is present. This can lead to the entrapment of pores by the solid and formation of microporosity. In general, it can be also concluded that the presence of side branching facilitates the formation of microporosities.

Fig. 37(a) shows the pattern of microporosities in the mid-height of the microstructure shown in Fig. 21. The phase field simulation of the dendrite growth pattern at the same location is presented in Fig. 37(b). As can be seen in this figure, the extent of secondary arm formation randomly varies along the dendrite array. Around the region denoted on the Fig. 37(b), the secondary arms have grown by the largest amount in the microstructure and the liquid phase is entrapped by the solid phase at several locations. It can be concluded that the vulnerability to microporosity formation is highest in such areas which are randomly distributed in the structure. The microstructure shown in Fig. 37(a) also depicts the presence of several micropores lined up in between two primary arms, which may be assumed as an indication of extensive side branching in this area.

Phase field simulations of dendrite growth show a great potential in the prediction of randomly distributed locations for extended growth of dendrite secondary arms, which may be correlated with the formation of microporosity. However, more accurate conclusions are to be made in an extensive study of multi-phase field simulation of dendrite growth taking into account a second phase field parameter representing the state of the pores during solidification.

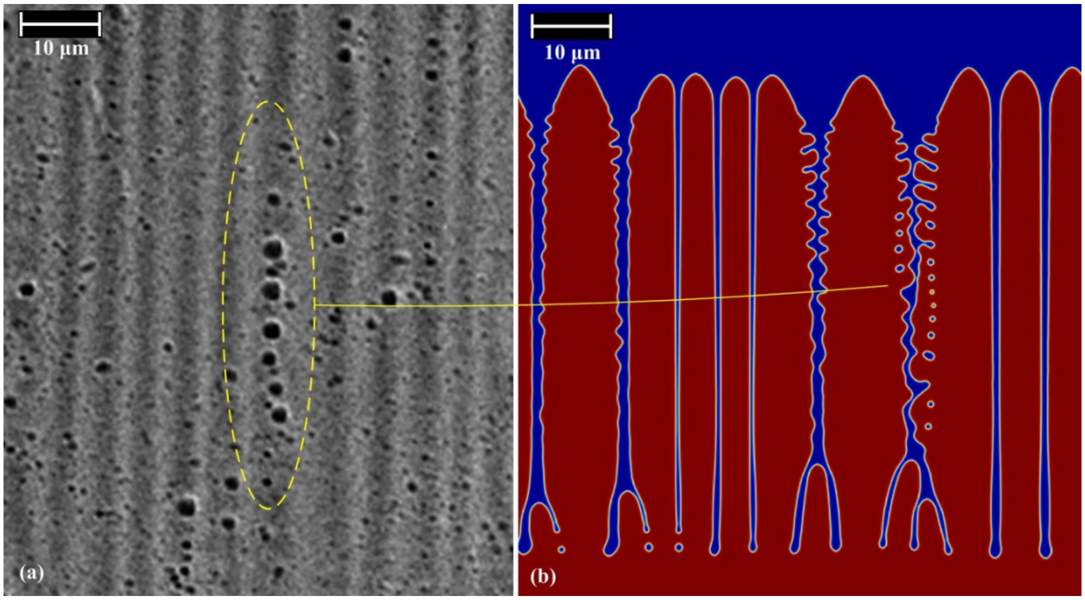

Fig. 37 (a) Evolution of microporosity in laser powder deposition of Ti-Nb alloys; the image is taken from the mid-height of the microstructure shown in Fig. 21; (b) the phase field simulation of dendritic growth at conditions corresponding to the mid-height of microstructure shown in Fig. 21, i.e., at point 2.

6.3 Transient growth conditions

Using the thermal model developed in this study, it has been shown that very high cooling rates with a highly transient pattern are characteristics of the laser powder deposition process. The simulation results of the thermal model for the temperature distribution can be directly fed into the microstructure model in order to perform a fully transient analysis of the dendrite growth evolution throughout the deposition process. Also, realistic morphology of the initial SL interface can be estimated from the temporal temperature distribution through the isotherm of melting temperature of the alloy.

6.3.1 Estimation of thermal conditions

As was discussed in Chapter 2 (Table 2), the measured chemical composition is nearly uniform throughout the clad section. Therefore, we assumed that the solidification temperature, taken as the alloy liquidus temperature, is constant along the interface during the solidification process. This way, the motion of interface during the process can be assumed analogous to that of the isotherm of the solidification temperature. In Fig. 38, the temperature distribution near and within the melt-pool is captured over the longitudinal center-plane at three successive times during laser powder deposition of Ti45Nb on Ti-6Al-4V at 5 mm/s laser scan velocity, i.e., the sample *c3* in Chapter 2. The isotherm of solidification temperature, i.e., ~1827 ºC, denoted by a dotted line, is shifting to the right along the laser scanning direction, while also keeping the same morphology.

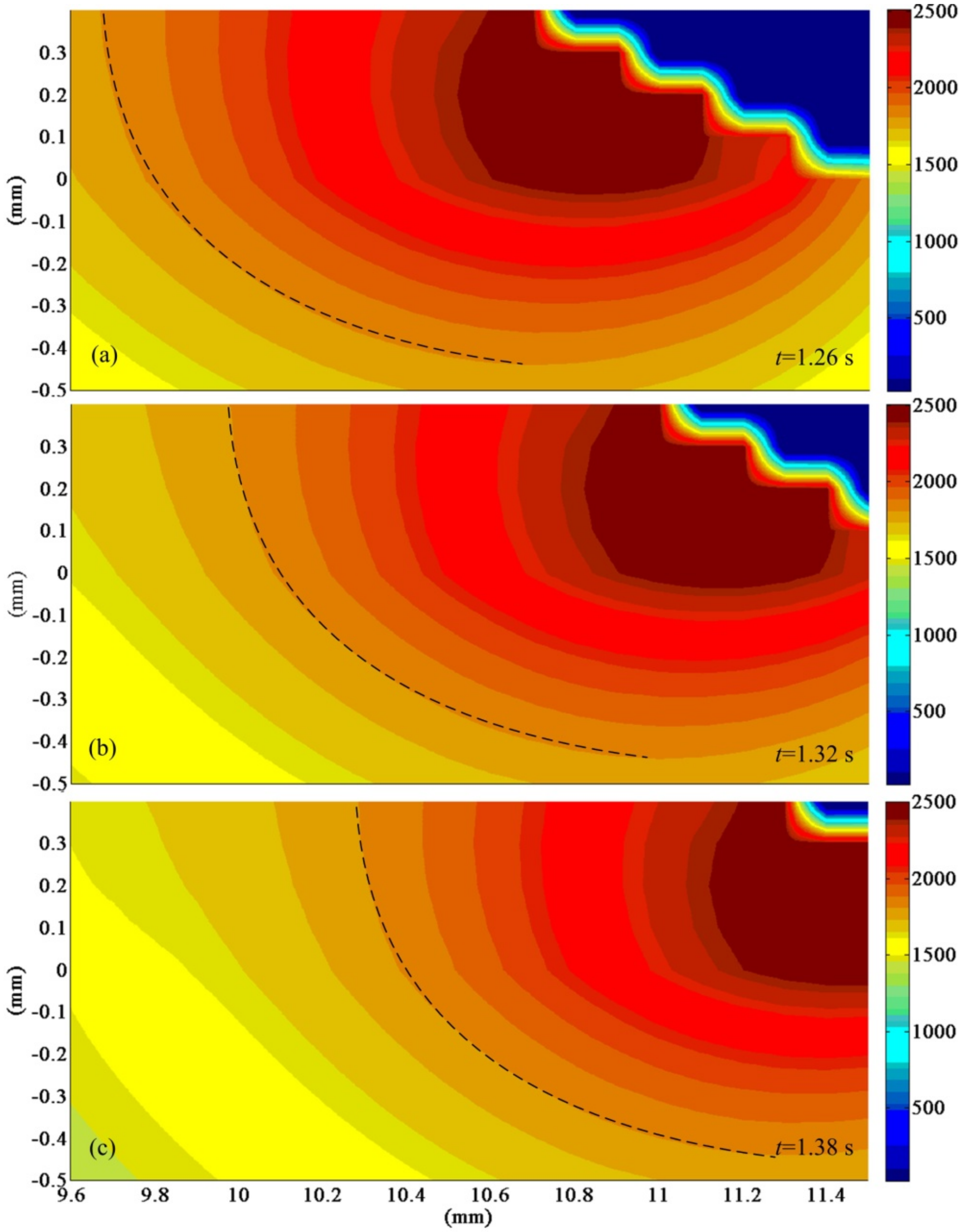

Fig. 38 The isotherms around and within the melt-pool through a longitudinal center-plane in laser powder deposition of Ti45Nb on Ti-6Al-4V at 5 mm/s laser scan velocity, i.e., the sample *c3* in Section 2; (a) *t*=1.26s; (b) *t*=1.32s and (c) *t*=1.38s; The dotted curve represents the isotherm of solidification temperature T_m= 1827 °C; The x-axis values are with respect to the one end of the original substrate, while the origin of y-axis is on the substrate surface; the blue area represents the ambient environment.

6.3.2 Growth of dendrites

So far in this study, the dendrite growth pattern in laser powder deposition has been simulated for rather small domains at steady-state and a fixed cooling rate throughout the simulation space and time. The results have been in good agreement with the experimental observations for the primary dendrite arm spacing at different locations. However, in larger domains where dendrite arrays with different initial orientations meet at some points, complex growth patterns may develop depending upon the thermal and solutal history of the system and random fluctuations in the melt-pool. The assumption of a fixed cooling rate also imposes significant errors in the driving force of dendrite growth where highly transient thermal conditions are applied on a large simulation domain.

To simulate the dendrite growth under transient thermal conditions of the laser powder deposition process, a portion of material including the SL interface within the thermal domain shown in Fig. 38 is considered. The CA method with the algorithm shown in Fig. 26 is applied to the sample while imposing, at each time step, the temperature distribution obtained from the thermal model. The initial seed on the domain is defined with the same morphology as that of the isotherm of melting temperature, as depicted with a dotted line on Fig. 26. Random perturbations are introduced on the initial SL interface and the grid size is taken as 1μm for speed considerations. The noise amplitude for the solid fraction increment is taken as 0.01. The solution time step is 1×10^{-5} s and material properties are the same as those listed in Table 7. The simulated dendrite growth pattern in the time period of 1.26 - 1.38 s during the deposition process of Ti-Nb on Ti-6Al-4V, based on the motion of isotherm of melting temperature shown in Fig. 38(a)-(c), is represented in Fig. 39.

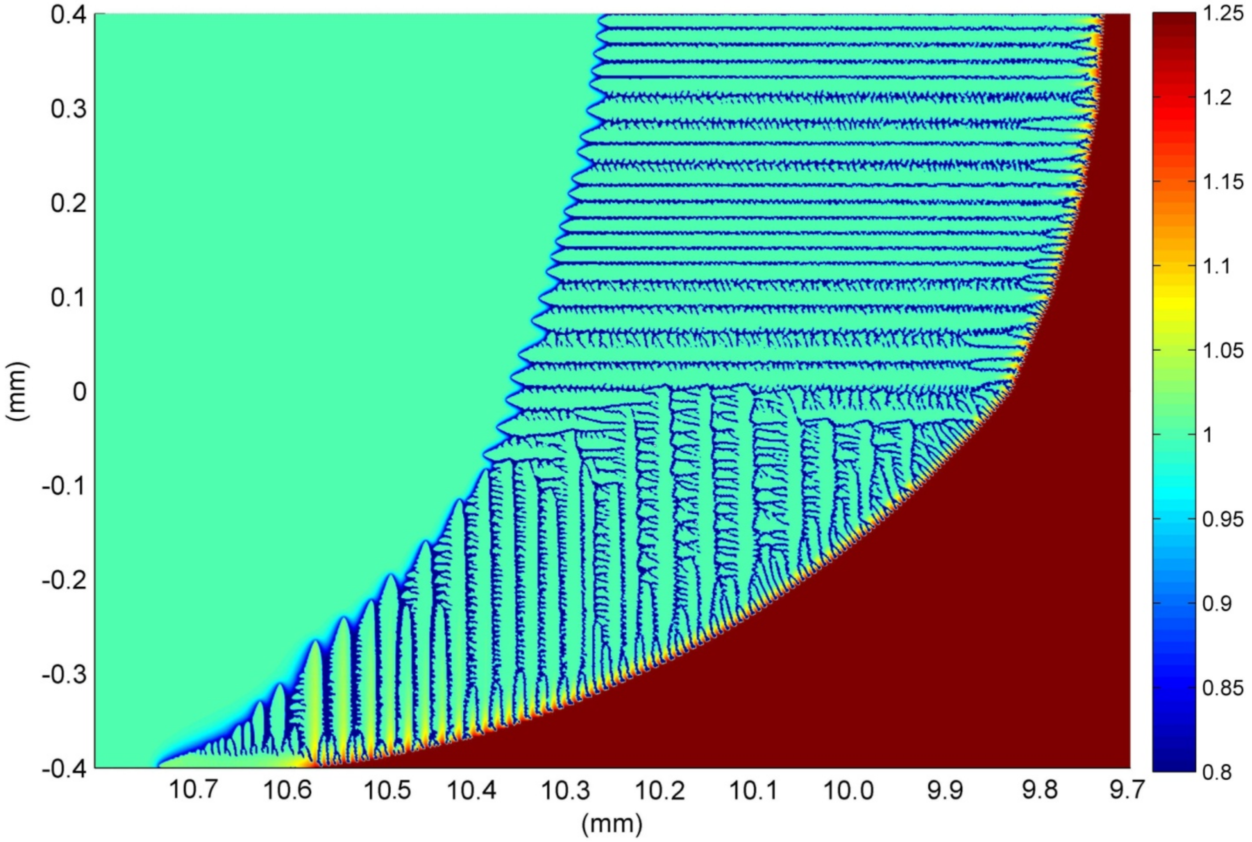

Fig. 39 CA simulation for the normalised concentration field showing the dendrite growth pattern developed in the time period of 1.26 - 1.38 s during laser powder deposition Ti-Nb on Ti-6Al-4V; The temperature distribution at each time step is obtained from the simulations of the thermal model for the sample *c3* in Chapter 2.

As mentioned earlier, the sample in Fig. 39 is taken from the mid-height region of the microstructure shown in Fig. 21. Fig. 39 qualitatively shows that the average primary spacing is increasing downward from the top of the figure which corresponds to an area around the mid-height of the original sample. However, the average spacing is approximately twice as the experimental and PF simulation data for local simulations of growth at steady-state given in Fig. 36. The image shown in Fig. 40(a) and (b) illustrates the qualitative comparison made between the experimental and simulated evolution of the dendrite growth pattern at the conjunction point of the two perpendicular initial orientations. For the dendrites growing upward, they both agree in that secondary arms grow only along the overall advancing direction of the SL interface. Some of these secondary arms eventually turn into primary arms growing along the horizontal axis. The competition is finally won by the horizontal dendrites growing at the top-half part of the domain where the cooling rate is higher.

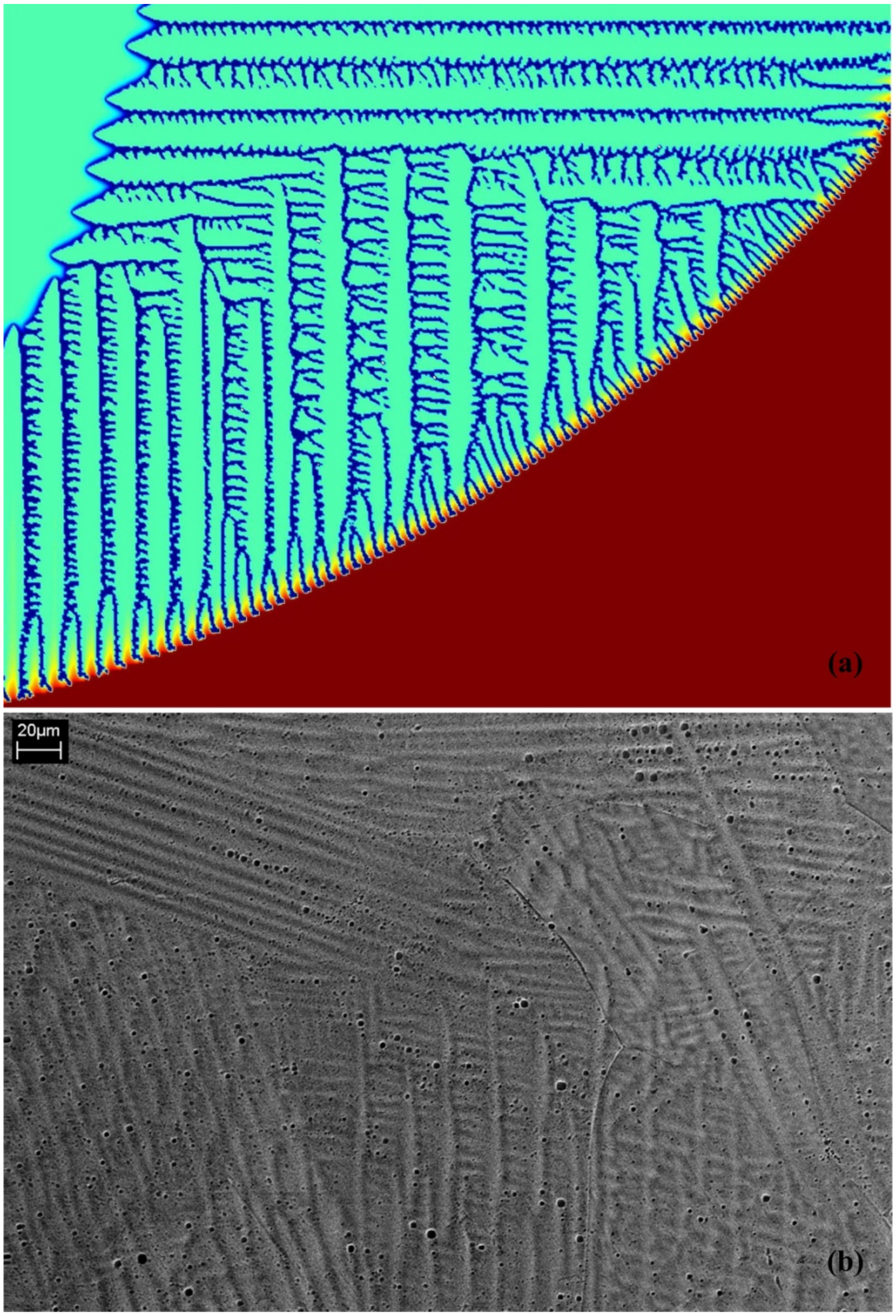

Fig. 40 (a) The CA simulation of the dendrite growth pattern; A magnified portion of the mid-part of the image shown in Fig. 39 showing the impingement of the dendrites advancing along the two perpendicular growth orientations; (b) The experimental observation of the same phenomenon taken from the mid-height of the microstructure shown in Fig. 21.

The growth pattern shown in Fig. 39 and Fig. 40 illustrates that, in the CA simulations with virtual front tracking, the artificial mesh anisotropy is a dominant factor at the extremely high cooling rates of the laser powder deposition process, i.e., in the order of 2000 K/s. As can be observed in Fig. 40, the growth of dendrites at ~45º is superseded by that of the 0º and 90º orientations. Moreover, due to the factors previously described in the Section 1.4.1 of this study, CA techniques are not quantitatively reliable especially at high cooling rates and transient growth conditions. Another source of error in 2-D modelling of microstructure comes from the fact that for large simulation domains the effect of the missing third dimension becomes more significant. Also, although the thermal model is itself experimentally validated, the potential errors in simulation of the temporal evolution of the temperature distribution also contribute to the inherent errors of the microstructure model which is based on the thermal model output.

6.4 Summary

With the optimized set of phase field parameters, the developed model was used to investigate the effect of local processing parameters, V_s and G, on the primary dendrite arm spacing at different locations along the height of the microstructure shown in Fig. 21. Through an investigation of the effect of system width increased on the spacing evolution, it was found that, for the upper part of the microstructure, the dendrite spacing was not considerably affected by the width values over 100μm. However, at the bottom of the microstructure where the dendrite size is significantly larger, the minimum acceptable width went higher up to ~150μm. The simulation results for the spacing evolution at several locations showed a remarkable agreement with the experimental observations, while also matching qualitatively with the experimental predictions of the Hunt model [27]. The counter-effect of V_s and G when moving from the top to bottom of the microstructure resulted in a minimum spacing around the mid-height.

PF simulations showed a great capacity to predict extended growth of secondary arms occurring randomly across the dendrite arrays. Examination of the microstructure revealed that the microporosity lined up at a few random locations between the primary arms, which may be correlated with the extent of the secondary arm formation. Further PF studies are needed to quantify the formation of microporosity and analyze the involved mechanisms by incorporation of a second phase field parameter representing the state of the pores.

CA simulations of transient growth of dendrites in laser powder deposition were able to predict growth competition between different initial orientations of dendrites growing from the SL interface with a realistic morphology. However, the results were not as quantitatively accurate as the PF modelling output for the local simulation of primary dendrite arm spacing at steady-state. Several qualitative features in the microstructure shown in Fig. 21 were successfully simulated with this method, as illustrated in Fig. 39 and Fig. 40. The dendrite arm spacing has slightly decreased from the mid-height of the microstructure (equivalent to the top part of the simulation domain) to the bottom. The dendrites growing upward were overgrown by the dendrites growing along the horizontal axis, which undergo a higher cooling rate during the process. Secondary arms for the upward growing dendrites formed only on one side, i.e., along the overall growth direction, and some finally became primary arms along the horizon which in turn develops secondary arms themselves. Further study of the transient growth of dendrites is to be implemented using the PF method which is significantly more accurate specially when dealing with various growth orientations in one domain and also for simulations at non-steady state conditions.

Chapter 7

Conclusions and future work

The dendritic growth patterns in laser powder deposition of Ti-Nb alloys were simulated in 2-D, both at steady-state and transient thermal conditions. The first element of this study included an experimental design in order to obtain the best visual properties in the deposited material. The developed microstructures were then experimentally studied for the samples deposited with the optimized set of processing parameters, including the laser power, laser scan velocity, beam diameter and powder feed rate. The second element of the current work was to simulate the transient thermal conditions during the laser deposition process of Ti-Nb alloys. An integrated finite element thermal model was developed along with a numerical approach to build the deposition geometry throughout the process. The simulated temperature distribution was then used to describe the morphology of the SL interface based on the motion of the isotherm of solidification temperature of the alloy. The third element of the study consisted of simulation of steady-state and transient growth of dendrites during the laser powder deposition process. An integrated PF model equipped with adaptive grid technique was employed for simulation of directional solidification at steady-state conditions using the local processing parameters obtained from the thermal model, i.e., the temperature gradient and interface velocity. The CA method along with a virtual front tracking scheme was used to model the dendrite growth patterns under transient conditions and on a larger computational domain. This domain consisted of an initial solid seed of the simulated SL interface morphology introducing various initial growth orientations. The core findings of the present study can be itemized as follows:

- A fast procedure was developed for experimental design of laser powder deposition through definition of a new parameter, supplied energy E_s, which combines the effects of laser specific energy, E, and the powder density, ψ. E_s controls the amount of energy transferred to the unit mass of the powder entering the system. The optimized set of processing parameters was found by examining sets of laser processing variables (such as laser power, laser scan velocity, laser beam diameter and powder feed rate), each one representing a unique E_s value. The deposition of crack- and pore-free coatings with continuous beads was the selection criterion for the suitable E_s value.
- Experimental examination of the Ti-Nb samples formed under the optimized set of parameters revealed a uniform chemical composition but a rather non-uniform dendrite morphology and size across the height of the longitudinal and cross-sectional metallography specimens.
- An integrated thermal model was created using finite elements to predict the temperature distribution in the system throughout the deposition process. This model incorporated a novel approach for real-time evolution of the deposition geometry. With this approach, addition of new material in the system was done through activation of a set of previously inactive elements in each solution time step. Therefore, the deposition geometry and thus the SL interface morphology were simulated with realistic shapes resembling those observed in the experiments. The model output can be fed into the microstructure model in two different ways. One way is through the estimation of local processing parameters, the temperature gradient and solidification velocity, for simulation of steady-state growth of dendrites on rather small domains. The other way is to directly use the temporal distribution of temperature for simulation of transient growth of dendrites in larger samples.
- The PF model output showed a remarkable agreement with the predictions of classical models of solidification, i.e., the KGT model, for the kinetics of steady-state growth or the initial unsteady growth of dendrites at a given fixed cooling rate. The spacing simulations for steady-state growth of dendrites at fixed local processing conditions also agreed very well with the experimental observations, both qualitatively and quantitatively. The PF model was able to show a minimum spacing value in the mid-height area of the sample, where the counteracting effects of solidification velocity and temperature gradient set the maximum cooling rate in the process.
- The CA simulation of the transient growth of dendrites in laser powder deposition showed a good ability to reproduce qualitative features when a realistic SL interface orientation is embedded in

the simulation domain, thus introducing various growth orientations on the same field and taking into account the transient thermal conditions. A gradual decrease in the arm spacing was observed from the top to the bottom of the simulation domain, agreeing with the experimental observations. As also observed in the microstructure, the simulation results showed that the growth competition is won by those dendrites more inclined along the actual laser scanning direction, i.e., those dendrites growing closer to the top part of the microstructure. Also, the secondary arms of the dendrites growing upward from the bottom part of the sample formed only on one side, i.e., along the scanning direction, some of which eventually turned into primary arms.

The following ideas are suggested as future work in order to improve the accuracy and capability of the existing set of models:

- The accuracy of the prediction of the deposition geometry and thus the melt-pool morphology can be greatly improved if the deposition area is more finely meshed. However, with the existing numerical scheme which discretizes the entire deposited material into equally spaced intervals, the required computational capacity dramatically increases with further mesh refinements. Therefore, a more novel numerical scheme is to be developed which is capable of re-meshing the entire system in each solution time step, thus keeping the refined mesh only within the deposition area.
- To compensate for the effect of fluid flow, the present thermal model uses a modification in the thermal conductivity at temperatures higher than the melting point of the alloy. Instead, the model accuracy can be further improved by solving also the mass transport equations for the fluid velocity, which in turn significantly lowers the overall computational efficiency.
- The formation of microporosity can be more systematically analyzed developing a multi-phase field model with the second phase field parameter defined as the state of the pores in the system. On the basis of the present PF model, only weak conclusions can be made regarding the correlations between the extent and locations of growth of secondary arms with the likelihood of microporosity formation.
- The PF model is to be implemented for the simulation of dendrite growth patterns under transient growth conditions. Not only will the overall simulation accuracy be improved, but also the effect of artificial mesh anisotropy which is inherent to CA techniques for growth at high cooling rates will be eliminated.

Bibliography

[1] Kurz, W. and Fisher, D.J. 1984. Fundamentals of solidification. Trans Tech, Aedermannsdorf; Switzerland.

[2] Kurz, W. and Fisher, D.J. 1981. Dendrite growth at the limit of stability: tip radius and spacing. *Acta Metallurgica* 29, 11-20.

[3] Lewis, G.K. and Schlienger, E. 2000. Practical considerations and capabilities for laser assisted direct metal deposition. *Materials & Design* 21, 417-423.

[4] Arcella, F.G. and Froes, F.H. 2000. Producing titanium aerospace components from powder using laser forming. *JOM* 52, 28-30.

[5] Griffith, M.L., Keicher, D.M., Atwood, C.L., Romero, J.A., Smugeresky, J.E., Harwell, L.D. and Greene, D.L. 1996. Free form fabrication of metallic components using laser engineered net shaping (LENS). In *Proceedings of the Solid Freeform Fabrication Symposium,* Austin, TX, 1996, 125-132.

[6] Fallah, V., Corbin, S.F. and Khajepour, A. 2010. Solidification behaviour and phase formation during pre-placed laser cladding of Ti45Nb on mild steel. *Surface and Coatings Technology* 204, 2400-2409.

[7] Fallah, V., Alimardani, M., Corbin, S.F. and Khajepour, A. 2010. Impact of localized surface preheating on the microstructure and crack formation in laser direct deposition of Stellite 1 on AISI 4340 steel. *Applied Surface Science* 257, 1716-1723.

[8] Alimardani, M., Fallah, V., Khajepour, A. and Toyserkani, E. 2010. The effect of localized dynamic surface preheating in laser cladding of Stellite 1. *Surface and Coatings Technology* 204, 3911-3919.

[9] Costa, L., Vilar, R., Reti, T. and Deus, A.M. 2005. Rapid tooling by laser powder deposition: Process simulation using finite element analysis. *Acta Materialia* 53, 3987-3999.

[10] Qi, H., Azer, M. and Singh, P. 2010. Adaptive toolpath deposition method for laser net shape manufacturing and repair of turbine compressor airfoils. *The International Journal of Advanced Manufacturing Technology* 48, 121-131.

[11] Kobryn, P.A. and Semiatin, S.L. 2001. The laser additive manufacture of Ti-6Al-4V. *JOM* 53, 40-42.

[12] Hollander, D.A., Von Walter, M., Wirtz, T., Sellei, R., Schmidt-rohlfing, B., Paar, O. and Erli, H. 2006. Structural, mechanical and in vitro characterization of individually structured Ti–6Al–4V produced by direct laser forming. *Biomaterials* 27, 955-963.

[13] Hee Young, K., Satoru, H., Jae Il, K., Hosoda, H. and Miyazaki, S. 2004. Mechanical properties and shape memory behavior of Ti-Nb alloys. *Materials Transactions* 45, 2443-2448.

[14] Lin, J.C., Ju, C. and Lee, C. 2004. Medical implant made of biocompatible low modulus high strength titanium-niobium alloy and method of using the same, US Patent, US6752882.

[15] Wang, B.L., Wang, Y.B. and Zheng, Y.F. 2006. Phase constitution, mechanical property and corrosion resistance of the Ti-Nb alloys. *Key Engineering Materials* 324-325, 655-658.

[16] Kelly, S.M. and Kampe, S.L. 2004. Microstructural evolution in laser-deposited multilayer Ti-6Al-4V builds: Part I. Microstructural characterization. *Metallurgical and Materials Transactions A* 35, 1861-1867.

[17] Kobryn, P.A., Moore, E.H. and Semiatin, S.L. 2000. The effect of laser power and traverse speed on microstructure, porosity, and build height in laser-deposited Ti-6Al-4V. *Scripta Materialia* 43, 299-305.

[18] Yang, J. and Wang, F. 2009. 3D finite element temperature field modelling for direct laser fabrication. *International Journal of Advanced Manufacturing Technology* 43, 1060-1068.

[19] Neela, V. and De, A. 2009. Three-dimensional heat transfer analysis of LENS ™ process using finite element method. *The International Journal of Advanced Manufacturing Technology* 45, 935-943.

[20] Wang, L. and Felicelli, S. 2007. Process modeling in laser deposition of multilayer SS410 steel. *Transactions of the ASME.Journal of Manufacturing Science and Engineering* 129, 1028-1034.

[21] Peyre, P., Aubry, P. and Fabbro, R. 2008. Analytical and numerical modelling of the direct metal deposition laser process. *Journal of Physics.D, Applied Physics* 41, 025403.

[22] Alimardani, M., Toyserkani, E. and Huissoon, J.P. 2007. A 3D dynamic numerical approach for temperature and thermal stress distributions in multilayer laser solid freeform fabrication process. *Optics and Lasers in Engineering* 45, 1115-1130.

[23] Qi, H., Mazumder, J. and Ki, H. 2006. Numerical simulation of heat transfer and fluid flow in coaxial laser cladding process for direct metal deposition. *Journal of Applied Physics* 100, 024903.

[24] Kurz, W. and Trivedi, R. 1992. Microstructure and phase selection in laser treatment of materials. *Journal of Engineering Materials and Technology* 114, 450-458.

[25] Flemings, M.C. 1974. Solidification Processing. *Metallurgical Transactions* 5, 2121-2134.

[26] McLean, M. 1988. Directionally Solidified Materials for High Temperature Service. *British Corrosion Journal,* London.

[27] HUNT, J.D. 1979. Cellular and Primary Dendrite Spacings. In *Proceedings of Solidification and Casting of Metals,* Sheffield, England*,* July 1977*,* 3-9.

[28] Ma, D. 2002. Modeling of primary spacing selection in dendrite arrays during directional solidification. *Metallurgical and Materials Transactions B (Process Metallurgy and Materials Processing Science)* 33B, 223-233.

[29] Wang, W., Kermanpur, A., Lee, P.D., McLean, M., Wang, X., Ward, R.M. and Jacobs, M.H. 2001. An investigation of the effect of perturbations on dendritic growth in nickel base superalloys. In *SP, Superalloys; NI, Nickel base alloys,* Santa Fe, NM; USA, 23-26 Sept. 2001, American Vacuum Society, New York, NY, USA, 267-279.

[30] McCartney, D.G. and Hunt, J.D. 1984. A numerical finite difference model of steady state cellular and dendritic growth. In *Metallurgical Transactions A (Physical Metallurgy and Materials Science),vol.15A,no.6,pp.983-994,June 1984; Symposium on Establishment of Microstructural Spacing during Dendritic and Cooperative Growth, 7 March 1983, Atlanta, GA, USA.* 06, USA, 983-994.

[31] Hunt, J.D. and Lu, S. 1996. Numerical modeling of cellular/dendritic array growth: spacing and structure predictions. *Metallurgical and Materials Transactions A (USA)* 27A, 611-623.

[32] Dilthey, U., Pavlik, V. AND Reichel, T. 1997. Numerical simulation of dendritic solidification with modified cellular automata. Institute of Materials, London, UK.

[33] Sasikumar, R. and Sreenivasan, R. 1994. Two dimensional simulation of dendrite morphology. *Acta Metallurgica et Materialia* 42, 2381-2386.

[34] Zhu, M.F. and Hong, C.P. 2001. A modified cellular automaton model for the simulation of dendritic growth in solidification of alloys. *ISIJ International* 41, 436-445.

[35] Sanchez, L. and Stefanescu, D.M. 2002. Growth of solutal dendrites. A cellular automaton model. *International Journal of Cast Metals Research* 15, 251-256.

[36] Sanchez, L. and Stefanescu, D.M. 2003. Growth of solutal dendrites: a cellular automaton model and its quantitative capabilities. *Metallurgical and Materials Transactions A (Physical Metallurgy and Materials Science)* 34A, 367-382.

[37] Sanchez, L. and Stefanescu, D.M. 2004. A quantitative dendrite growth model and analysis of stability concepts. *Metallurgical and Materials Transactions A (Physical Metallurgy and Materials Science)* 35A, 2471-2485.

[38] Warren, J.A. and Boettinger, W.J. 1995. Prediction of dendritic growth and microsegregation patterns in a binary alloy using the phase-field method. *Acta Metallurgica et Materialia* 43, 689-703.

[39] Suzuki, T., Ode, M., Kim, S.G. and Kim, W.T. 2002. Phase-field model of dendritic growth. *Journal of Crystal Growth (USA)* 237-239, 125-131.

[40] Boettinger, W.J., Warren, J.A., Beckermann, C. and Karma, A. 2002. Phase-Field Simulation Of Solidification. *Annual Review of Materials Reviews (USA)* 32, 163-194.

[41] Echebarria, B., Folch, R., Karma, A. and Plapp, M. 2004. Quantitative phase-field model of alloy solidification. *Physical Review E (Statistical, Nonlinear)* 70, 61604-61-22.

[42] Provatas, N. and Elder, K. 2010. Phase-field methods in materials science and engineering. John Wiley.

[43] Karma, A. and Rappel, W. 1998. Quantitative phase-field modeling of dendritic growth in two and three dimensions. *Physical Review E (Statistical Physics, Plasmas), Fluids* 57, 4323-4349.

[44] Karma, A. and Rappel, W. 1996. Numerical simulation of three-dimensional dendritic growth. *Physical Review Letters* 77, 4050-4053.

[45] Lan, C.W., Chang, Y.C. and Shih, C.J. 2003. Adaptive phase field simulation of non-isothermal free dendritic growth of a binary alloy. *Acta Materialia* 51, 1857-1869.

[46] Granasy, L., Pusztai, T. and Warren, J.A. 2004. Modelling polycrystalline solidification using phase field theory. *Journal of Physics: Condensed Matter* 16, R1205-R1235.

[47] Boettinger, W.J. and Warren, J.A. 1996. The phase field method: simulation of alloy dendritic solidification during recalescence. *Metallurgical and Materials Transactions A (USA)* 27A, 657-669.

[48] Loginova, I., Amberg, G. and Agren, J. 2001. Phase-field simulations of non-isothermal binary alloy solidification. *Acta Materialia (USA)* 49, 573-581.

[49] Amoorezaei, M., Gurevich, S. and Provatas, N. 2010. Spacing characterization in Al–Cu alloys directionally solidified under transient growth conditions. *Acta Materialia* 58, 6115-6124.

[50] Ramirez, J.C., Beckermann, C., Karma, A. and Diepers, H. 2004. Phase-field modeling of binary alloy solidification with coupled heat and solute diffusion. *Physical Review E (Statistical, Nonlinear* 69, 51607-51-16.

[51] Broughton, J.Q., Bonissent, A. and Abraham, F.F. 1981. The FCC (111) and (100) crystal-melt interfaces: A comparison by molecular dynamics simulation. *Journal of Chemical Physics* 74, 4029-4039.

[52] Karma, A. 2001. Phase-field formulation for quantitative modeling of alloy solidification. *Physical Review Letters* 87, 115701/1-115701/4.

[53] Greenwood, M., Haataja, M. and Provatas, N. 2004. Crossover scaling of wavelength selection in directional solidification of binary alloys. *Physical Review Letters* 93, 246101/1-246101/4.

[54] Rappaz, M., Gandin, C., Jacot, A. and Charbon, C. 1995. Modeling of microstructure formation. In *Modeling of Casting, Welding and Advanced Solidification Processes VII; London; UK; 10-15 Sept. 1995;* Minerals, Metals and Materials Society, Warrendale, PA, USA, 501-516.

[55] Lipton, J., Glicksman, M.E. and Kurz, W. 1984. Dendritic growth into undercooled alloy metals. *Materials Science and Engineering* 65, July.

[56] Trivedi, R. and Kurz, W. 1994. Dendritic growth. *International Materials Reviews* 39, 49-74.

[57] Kessler, D.A. and Levine, H. 1986. Stability of dendritic crystals. *Physical Review Letters* 57, 3069-3072.

[58] Zhu, M.F. and Stefanescu, D.M. 2007. Virtual front tracking model for the quantitative modeling of dendritic growth in solidification of alloys. *Acta Materialia* 55, 1741-1755.

[59] Michelic, S.C., Thuswaldner, J.M. and Bernhard, C. 2010. Polydimensional modelling of dendritic growth and microsegregation in multicomponent alloys. *Acta Materialia* 58, 2738-2751.

[60] Jacot, A. and Rappaz, M. 2002. A pseudo-front tracking technique for the modelling of solidification microstructures in multi-component alloys. *Acta Materialia* 50, 1909-1926.

[61] Zhao, P., Vénere, M., Heinrich, J.C. and Poirier, D.R. 2003. Modeling dendritic growth of a binary alloy. *Journal of Computational Physics* 188, July.

[62] Pavlyk, V. and Dilthey, U. 2004. Simulation of weld solidification microstructure and its coupling to the macroscopic heat and fluid flow modelling. *Modelling and Simulation in Materials Science and Engineering* 12, S33-S45.

[63] Yin, H. and Felicelli, S.D. 2010. Dendrite growth simulation during solidification in the LENS process. *Acta Materialia* 58, 1455-1465.

[64] Zhan, X.H., Dong, Z.B., Wei, Y.H. and Ma, R. 2009. Simulation of grain morphologies and competitive growth in weld pool of Ni–Cr alloy. *Journal of Crystal Growth* 311, 4778-4783.

[65] Tan, W., Bailey, N.S. and Shin, Y.C. 2011. A novel integrated model combining Cellular Automata and Phase Field methods for microstructure evolution during solidification of multi-component and multi-phase alloys. *Computational Materials Science* In Press, Corrected Proof.

[66] Fallah, V., Alimardani, M., Corbin, S.F. and Khajepour, A. 2011. Temporal development of melt-pool morphology and clad geometry in laser powder deposition. *Computational Materials Science* 50, 2124-2134.

[67] Alimardani, M., Toyserkani, E. and Huissoon, J.P. 2007. A 3D dynamic numerical approach for temperature and thermal stress distributions in multilayer laser solid freeform fabrication process. *Optics and Lasers in Engineering* 45, 1115-1130.

[68] Gurevich, S., Amoorezaei, M. and Provatas, N. 2010. Phase-field study of spacing evolution during transient growth. *Physical Review E (Statistical, Nonlinear)* 82, 051606 (8 pp.).

[69] Popov, S. 2009. Fiber laser overview and medical applications. In *Tunable Laser Applications,* F.J. Duarte, Ed. CRC, New York, 197-226.

[70] Silfvast, W.T. 2004. Laser Fundamentals. Cambridge University Press, Cambridge.

[71] Steen W M. 2003. Laser material processing. Book. Third Edition. London, UK.

[72] Wu, X., Zhu, B., Zeng, X., Hu, X. and Cui, K. 1996. Critical state of laser cladding with powder auto-feeding. *Surface and Coatings Technology* 79, 200-204.

[73] Zhou, S., Dai, X. and Zeng, X. 2009. Effects of processing parameters on structure of Ni-based WC composite coatings during laser induction hybrid rapid cladding. *Applied Surface Science* 255, 8494-8500.

[74] Fallah, V., Corbin, S.F. and Khajepour, A. 2010. Process optimization of Ti–Nb alloy coatings on a Ti–6Al–4V plate using a fiber laser and blended elemental powders. *Journal of Materials Processing Technology* 210, 2081-2087.

[75] Chan, C., Mazumder, J. AND Chen, M.M. 1983. A model for surface tension driven fluid flow in laser surface alloying. In *Lasers in Materials Processing, Proceedings, Conference,* Los Angeles, Jan. 1983; E.A.Metzbower, Ed. Metals Park, OH, USA; American Society for Metals, 150-157.

[76] Chan, C., Mazumder, J. and Chen, M.M. 1984. A two-dimensional transient model for convection in laser melted pool. *Metallurgical Transactions A (Physical Metallurgy and Materials Science)* 15A, 2175-2184.

[77] Anthony, T.R. and Cline, H.E. 1977. Surface rippling induced by surface-tension gradients during laser surface melting and alloying. *Journal of Applied Physics* 48, 3888-3894.

[78] Almeida, A., Petrov, P., Nogueira, I. and Vilar, R. 2001. Structure and properties of Al–Nb alloys produced by laser surface alloying. *Materials Science and Engineering A* 303, 273-280.

[79] Kattner, U.R. and Boettinger, W.J. 1992. Thermodynamic calculation of the ternary Ti-Al-Nb system. *Materials Science and Engineering: A* 152, 9-17.

[80] Unocic, R.R. and Dupont, J.N. 2004. Process efficiency measurements in the laser engineered net shaping process. *Metallurgical and Materials Transactions B (Process Metallurgy and Materials Processing Science)* 35B, 143-152.

[81] Brown, S. and Song, H. 1992. Finite Element Simulation of Welding of Large Structures. *Journal of Engineering for Industry (Transactions of the ASME) (USA)* 114, 441-451.

[82] Lampa, C., Kaplan, A.F.H., Powell, J. and Magnusson, C. 1997. An analytical thermodynamic model of laser welding. *Journal of Physics D: Applied Physics* 30, 1293-1299.

[83] Mills, K.C. 2002. Recommended values of thermopysical properties for selected commercial alloys. ASM International, Cambridge, England.

[84] Murray, J.L. 1987. The Nb-Ti (Niobium-Titanium) System. In *Phase Diagrams of Binary Titanium Alloys,* J.L. Murray, Ed. ASM International, , 188-193.

[85] Mullins, W.W. and Sekerka, R.F. 1964. Stability of a planar interface during solidification of a dilute binary alloy. *Journal of Applied Physics* 35, 444-451.

[86] Hunt, J.D. and McCartney, D.G. 1987. Numerical finite difference model for steady state cellular array growth. *Acta Metallurgica* 35, 89-99.

[87] Zimmermann, M., Carrard, M. and Kurz, W. 1989. Rapid solidification of Al-Cu eutectic alloy by laser remelting. *Acta Metallurgica* 37, 3305-3313.

[88] Hoadley, A.F.A., Rappaz, M. and Zimmermann, M. 1991. Heat-flow simulation of laser remelting with experimental validation. *Metallurgical Transactions B (Process Metallurgy)* 22B, 101-109.

[89] Fathi, A., Toyserkani, E., Khajepour, A. and Durali, M. 2006. Prediction of melt pool depth and dilution in laser powder deposition. *Journal of Physics D (Applied Physics)* 39, 2613-2623.

[90] Kurz, W., Giovanola, B. and Trivedi, R. 1986. Theory of microstructural development during rapid solidification. *Acta Metallurgica* 34, 823-830.

[91] Trivedi, R. and Kurz, W. 1986. Morphological stability of a planar interface under rapid solidification conditions. *Acta Metallurgica* 34, 1663-1670.

[92] Liu, Y., Long, Z., Wang, H., Du, Y. and Huang, B. 2006. A predictive equation for solute diffusivity in liquid metals. *Scripta Materialia* 55, 367-370.

[93] Gaeumann, M., Trivedi, R. and Kurz, W. 1997. Nucleation ahead of the advancing interface in directional solidification. In *Materials Science & Engineering A (Structural Materials: Properties, Microstructure and Processing),* vol. A226-228, pp.763-769.

[94] Hunt, J.D. 1984. Steady state columnar and equiaxed growth of dendrites and eutectic. *Materials Science and Engineering* 65, 75-83.

[95] Kurz, W., Bezençon, C. and Gäumannpresent, M. 2001. Columnar to equiaxed transition in solidification processing. *Science and Technology of Advanced Materials* 2, 185-191.

[96] Krane, M.J.M., Johnson, D.R. and Raghavan, S. 2009. The development of a cellular automaton-finite volume model for dendritic growth. *Applied Mathematical Modelling* 33, 2234-2247.

[97] Langer, J.S. and Muller-krumbhaar, H. 1978. Theory of dendritic growth-II. Instabilities in the limit of vanishing surface tension. *Acta Metallurgica* 26, 1689-1695.

[98] Jacot, A., Meidani, H. and Felberbaum, M. 2009. Phase-field simulation of micropores constrained by a solid network. *Transactions of the Indian Institute of Metals* 62, 305-308.

[99] Meidani, H. and Jacot, A. 2011. Phase-field simulation of micropores constrained by the dendritic network during solidification. *Acta Materialia* 59, 3032-3040.

[100] Huang, S. and Glicksman, M.E. 1981. Overview 12: Fundamentals of dendritic solidification—II development of sidebranch structure. *Acta Metallurgica* 29, 717-734.

[101] Esaka, H. and Kurz, W. Columnar dendrite growth: Experiments on tip growth. *Journal of Crystal Growth* 72, 578-584.

[102] Temkin, D.E. 1962. Kinetics of growth of a crystal needle in a supercooled binary melt. *Kristallografiya* 7, 446-450.

[103] Chen, S., Merriman, B., Osher, S. and Smereka, P. 1997. A Simple Level Set Method for Solving Stefan Problems. *Journal of Computational Physics* 135, 8-29.

[104] Brackbill, J.U., Kothe, D.B. and Zemach, C. 1992. A continuum method for modeling surface tension. *Journal of Computational Physics* 100, 335-354.

Appendix I

A1. Modelling of dendritic growth in rapid solidification of superheated melts

The principles of the KGT (Kurz-Giovanola-Trivedi) model [90] based on IMS (Ivantsov-marginal stability), which is the most commonly used method of dendrite growth modelling in rapid solidification, are presented in this section.

A1.1. Dendrite tip radius (*R(V,G)* - KGT model)

It is shown that dendrite tips grow closely to a state called marginally stable [97]. It is therefore assumed by Kurz *et al.* [90]:

$$R = \lambda_{\mathrm{s}} \tag{64}$$

where λ_{s} is the critical wavelength of the solid/liquid interface at the limit of stability and it is assumed that the dendrite is growing at steady state. Since the instability wavelength of a sphere and of a planar interface are very close to each other, Huang and Glicksman [100] and Kurz *et al.* [90] used λ_{s} for a planar interface for simplicity. Mullins and Sekerka [85] calculated the wavelength of the marginally stable plane front as

$$\omega^2\Gamma = m_l G_{\mathrm{c}} \xi_{\mathrm{c}} - G \tag{65}$$

with

$$\omega = 2\pi/\lambda_{\mathrm{s}} \tag{66}$$

$$\xi_{\mathrm{c}} = 1 - \frac{2k}{\{1+[4\pi D_L/(\lambda_{\mathrm{s}} V_s)]^2\}^{1/2} - 1 + 2k} \tag{67}$$

Γ is the Gibbs-Thomson parameter defined as the ratio of the specific liquid/solid interface energy to the melting entropy and D_l is the liquid interdiffusion coefficient.

Equation (65) has been derived for the limit of small thermal Peclet numbers. However, in metals, the thermal peclet number is much smaller than the solutal peclet number by a factor of D_l/α (~ 10^{-2}-10^{-4}). By defining the solutal peclet number as

$$P = RV_{\mathrm{s}}/2D_l \tag{68}$$

it is shown by Kurz *et al.* (KGT model) [90] that:

$$\xi_{\mathrm{c}} = 1 - \frac{2k}{\{1+[2\pi/P]^2\}^{\frac{1}{2}} - 1 + 2k} \tag{69}$$

$$R = 2\pi \left[\frac{\Gamma}{m_l G_{\mathrm{c}} \xi_{\mathrm{c}} - G}\right]^{\frac{1}{2}} \tag{70}$$

At high peclet numbers ($P > \pi^2/\sqrt{k}$), equation (69) reduces to

$$\xi_{\mathrm{c}} = \frac{\pi^2}{kP^2} \tag{71}$$

Combining equations (65) and (71), with the assumption that $G = 0$, the absolute stability condition can be obtained.

To solve equation (70), G and G_{c} must be known. G in directional solidification is determined by external heat flow. G_{c} can be calculated through a heat flux balance at the dendrite tip, considering negligible effect of G on the diffusion field around the tip (which is more reliable at low growth rates). Kurz and Fisher [1] showed that G_{c} can be approximated as follow

$$G_{\mathrm{c}} = -\frac{V_{\mathrm{s}}}{D_l} c_{\mathrm{l}}^{*}(1-k) \tag{72}$$

Following the above approach of Kurz and Fisher [1] and applying the Ivantsov solution for the transport problem by Esaka and Kurz [101] (as indicated by equation (80), Kurz *et al.* [90] obtained the following solution:

$$V_{\mathrm{s}}{}^2 A + V_{\mathrm{s}} B + C = 0 \tag{73}$$

with

$$A = \frac{\pi^2 \Gamma}{P^2 D_l{}^2} \tag{74}$$

$$B = \frac{m_l c_0 (1-k) \xi_{\mathrm{c}}}{D_l[1-(1-k)\mathrm{Iv}(P)]} \tag{75}$$

$$C = G \tag{76}$$

$$\mathrm{Iv}(P) \equiv P\exp(P) E_1(P) \tag{77}$$

It should be noted that either average or temperature dependent values of k, m_l and D_l must be used in the above equations. The average values are usually determined by linear interpolation between the melting temperature of the pure component and the eutectic point.

A1.2. Dendrite tip temperature ($T_t(R,V_{\mathrm{s}})$ – KGT model)

The supersaturation by definition is

$$\Omega = \frac{c_{\mathrm{l}}^{*} - c_0}{c_{\mathrm{l}}^{*}(1-k)} \tag{78}$$

where c_l^* is the liquid composition at the dendrite tip. The transport problem around a paraboloid of revolution can be solved using Ivantsov's function

$$\Omega = \mathrm{Iv}(P) \tag{79}$$

Therefore,

$$c_l^* = \frac{c_0}{1-(1-k)\mathrm{Iv}(P)} \tag{80}$$

The tip temperature for the case of positive *G* values (i.e. superheated melts) is given by

$$T_{\mathrm{t}} = g(c_{\mathrm{l}}^{*}) - \Delta T_R \tag{81}$$

and $g(c_{\mathrm{l}}^{*})$ defines the liquidus line in the phase diagram. If m_l and *k* are constants, liquidus and solidus lines are straight and one can write

$$g(c_{\mathrm{l}}^{*}) = T_{\mathrm{f}} + m_l c_{\mathrm{l}}^{*} \tag{82}$$

where T_{m} is the melting temperature of the pure component. So, Kurz *et al.* [90] came up with

$$T_{\mathrm{t}} = T_{\mathrm{m}} + m_l c_{\mathrm{l}}^{*} - \frac{2\Gamma}{R} \tag{83}$$

Appendix II

A2. Equiaxed growth of dendrites (ahead of the columnar interface)

During directional growth, a constitutionally undercooled region may exist (always the case for dendritic growth) ahead of the interface. Therefore, a driving force for nucleation exists in this zone, which could lead to the formation of equiaxed grains suspended in the melt ahead of the columnar interface. Unlike constrained growth where the latent heat of fusion is transported through the solid, it has to be dissipated through the liquid during the free growth of the dendrites. In other words, free dendritic grains require an undercooled melt acting as a sink for the released latent heat thus helping their growth. The growth direction, in the case of equiaxed grains nucleated ahead of the columnar front, should be towards the columnar front (i.e. the direction with negative G value). Therefore, the following additional thermal undercooling should be added to the total tip undercooling [93]:

$$\Delta T_{\mathrm{t}} = Iv(P_{\mathrm{t}}) L_{\mathrm{f}} / c_{\mathrm{p}} \tag{84}$$

where L_{f} is the latent heat, c_{p} is the specific heat and P_{t} the thermal Peclet number which is defined as

$$P_{\mathrm{t}} = V_s R / 2\alpha \tag{85}$$

where α is the thermal diffusivity. Therefore, the total tip undercooling is given as

$$\Delta T = \Delta T_{\mathrm{c}} + \Delta T_R + \Delta T_{\mathrm{k}} + \Delta T_{\mathrm{t}} \tag{86}$$

where

$$\Delta T_{\mathrm{c}} = m_l (C_0 - C_{\mathrm{l}}^*) \tag{87}$$

$$\Delta T_{\mathrm{R}} = -2\Gamma / R \tag{88}$$

and ΔT_{k} is the kinetic undercooling which becomes important only at very high solidification rates.

In metals with high thermal diffusivity, thermal undercooling is often negligible compared to the effect of other contributors to the total tip undercooling. However, to calculate the dendrite tip radius, the temperature gradient (which is negative in the case of free growth or equiaxed) is required. But, again, the effect of temperature gradient compared to that of the solutal gradient is negligible. Thus, it seems reasonable to use the same model for both cases [93].

The liquid composition profile for one dendrite tip with a parabolic shape is obtained by Ivantsov's solution [102]:

$$c_{\mathrm{l}}[z] = c_0 + (c_{\mathrm{l}}^* - c_0) E_{\mathrm{l}}[P_{\mathrm{c}}(2z + R)/R] / E_{\mathrm{l}}[P_{\mathrm{c}}] \tag{89}$$

where E_l is the exponential integral and z is the distance from the tip of the dendrite along the dendrite axis. Assuming a linear phase diagram in the freezing range, the temperature profile in the liquid can be correspondingly calculated as

$$T[z] = T_\mathrm{l} + \left(T_\mathrm{eq} - T_\mathrm{l}\right)E_\mathrm{l}[P_\mathrm{c}(2z + R)/R]/E_\mathrm{l}[P_\mathrm{c}] \tag{90}$$

where T_l is the equilibrium liquidus temperature at composition c_0 and T_eq is the equilibrium liquidus temperature at the tip composition c_l^*:

$$T_\mathrm{l} = T_\mathrm{m} + m_l c_0 \tag{91}$$

$$T_\mathrm{eq} = T_\mathrm{m} + m_l c_\mathrm{l}^* \tag{92}$$

For simplicity, it is assumed that the temperature and composition profiles are the same along the whole dendritic front as those of the tips. On the other hand, the local liquid temperature is determined by the heat dissipation through the solid which is given by

$$T_\mathrm{q}[z] = T_\mathrm{t} + Gz \tag{93}$$

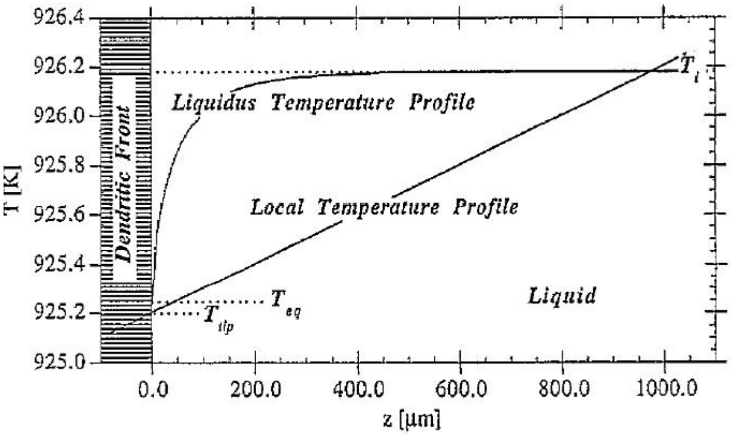

Fig. 41 Equilibrium liquidus and local temperature profile in front of the moving interface for Al-3wt.%Cu, V_s = 32 μm s^{-1}, G = 1000 K m^{-1} [93].

The local undercooling profile ahead of the moving solid-liquid interface can be determined as follow

$$\Delta T[z] = T[z] - T_\mathrm{q}[z] \tag{94}$$

Constitutionally undercooled zone ahead of the interface is schematically shown in Fig. 42. In this region nucleation may occur if the maximum growth undercooling is greater than the undercooling required for nucleation.

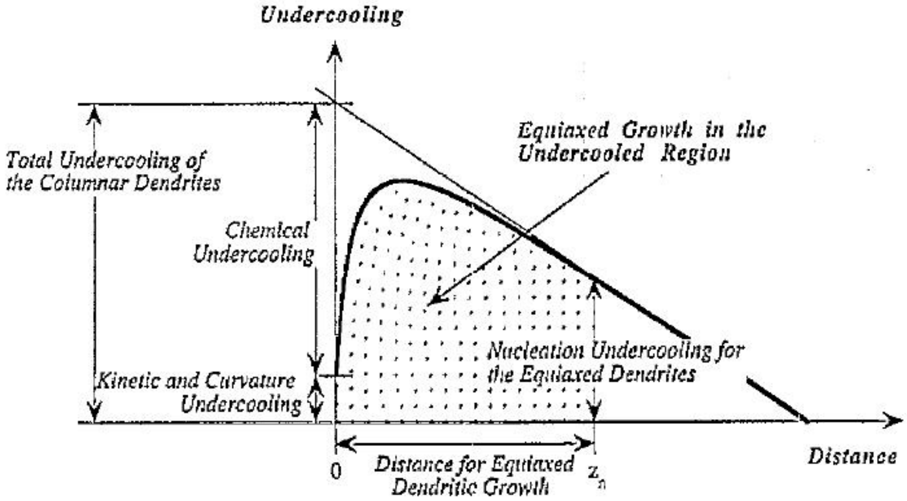

Fig. 42 Sketch of the undercooled region ahead of the moving solidification interface [93].

Appendix III

A3. Phase Field formulation for a dilute binary alloy

In this section the free energy functional of a dilute binary alloy will be developed incorporating a solid-liquid order parameter field $\phi(\vec{x})$, a concentration field $c(\vec{x})$ and a temperature field $T(\vec{x})$. The evolution of these fields will be determined by global minimization of the free energy functional which provides the driving force for non-equilibrium phase transformations in alloys.

A3.1 Free Energy Functional

The complete energy functional ΔF, which incorporates the effect of chemical and temperature contributions of the bulk phases as well as the effect of interface energy due to both the compositional and the crystal order gradients is given by

$$\Delta F = \int_V \left\{ \frac{|\epsilon_c \nabla c|^2}{2} + \frac{|\epsilon_\phi \nabla \phi|^2}{2} + f(\phi, c, T) \right\} dV \tag{95}$$

$\epsilon_c \equiv \sqrt{\mathrm{H}} W_c$ and $\epsilon_\phi \equiv \sqrt{\mathrm{H}} W_\phi$ are constants that scale the energy associated with the compositional boundary and solid-liquid interface, respectively. H is the nucleation barrier, while W_c and W_ϕ define the length scales of the compositional boundary and solid-liquid interface. In most cases, ϵ_c is negligible since ϵ_ϕ can be determined so as to account for the total surface energy.

A3.2 Choice of $\boldsymbol{f(\phi, c, T)}$

The bulk free energy density $f(\phi, c, T)$ in Eq. (95) is separated into two terms: the barrier term $Hg(\phi)$ depending only on phase, and a bulk free energy part $\bar{f}_{AB}^{mix}(\phi, c, T)$ depending on c, ϕ and T. Thus, generally speaking, $f(\phi, c, T)$ is given by

$$f(\phi, c, T) = Hg(\phi) + \bar{f}_{AB}^{mix}(\phi, c, T) \tag{96}$$

where function $g(\phi) = \phi^2(1-\phi)^2$ is used to interpolate the barrier term over the solid-liquid boundary. Using the characteristics of the equilibrium phase diagram for an ideal dilute binary alloy $\bar{f}_{AB}^{mix}(\phi, c, T)$ is expressed as [42]

$$\bar{f}_{AB}^{mix}(\phi, c, T) = \frac{R_g T_m}{\Omega_{\mathrm{v}}}[c \ln c - c] + f^A(T_m) - \Delta T \left[s_L - \frac{L_f}{T_m} \tilde{g}(\phi) \right] + [\epsilon_L + \Delta\epsilon \bar{g}(\phi)]c \tag{97}$$

where $T_m \equiv T_A$ is the melting temperature of species A, $\Delta T = T - T_m$, R_g the gas constant and Ω_{v} the molar volume of the alloy, s_L the entropy of liquid, ϵ_L (ϵ_S) the internal energy of the liquid (solid),

$\Delta\epsilon = \epsilon_S - \epsilon_L$, $f^A(T_m)$ the free energy of species A and L_f is the latent heat of fusion. $\tilde{g}(\phi) = \phi^3(6\phi^2 - 15\phi + 10)$ is a function interpolating entropy between solid and liquid. It returns a value of 0 for solid ($\phi = \phi_S$), a value of 1 for liquid ($\phi = 0$) and $0 < \tilde{g}(\phi) < 1$ for other values of ϕ. The function $\bar{g}(\phi) = \frac{1}{\ln k}\ln[1 - (1 - k)\tilde{g}(\phi)]$ is designed to have the same limits as $\tilde{g}(\phi)$, where k is the partition coefficient of the dilute binary alloy.

A3.3 Dynamical equations

Since the heat diffusion at normal solidification rates (not rapid) occurs much more rapidly than solute diffusion in a binary alloy, the temperature change is negligible in the time scale of the mass transfer. Therefore, it is reasonable to consider only the equations of phase field dynamics and solute diffusion.

A3.3.1 Phase field dynamics

Based on the hypothesis of dissipative dynamics and taking into account that order parameter in solidification is a non-conserved quantity, the evolution of the order parameter is simply constructed using the variational form of Eq. (95) so as to represent the driving force of the phase transformation. Thus,

$$\tilde{\tau}(\theta)\frac{\partial\phi}{\partial t} = -\frac{1}{H}\frac{\delta F[\phi,c,T]}{\delta\phi} + \eta'(\vec{x},t) \tag{98}$$

$$= \left(\frac{1}{2}\right)\left|\widetilde{W}(\theta)\nabla\phi\right|^2 - \frac{dg(\phi)}{d\phi} - \frac{1}{H}\frac{\partial\bar{f}_{AB}^{mix}(\phi,c,T)}{\partial\phi} + \eta'(\vec{x},t)$$

$$= \nabla.\left(\widetilde{W}^2(\theta)\nabla\phi\right) - \partial_x\left[\widetilde{W}(\theta)\widetilde{W}'(\theta)\partial_y\phi\right] + \partial_y\left[\widetilde{W}(\theta)\widetilde{W}'(\theta)\partial_x\phi\right] - \frac{dg(\phi)}{d\phi}$$

$$-\frac{1}{H}\frac{\partial\bar{f}_{AB}^{mix}(\phi,c,T)}{\partial\phi} + \eta'(\vec{x},t)$$

where M is a mobility constant related to the time scale for atomic rearrangement from the disordered phase to the ordered one, $\tau = 1/(MH)$, $\eta' = \eta/(MH)$, η a stochastic noise term that emulates the effect of thermal and compositional fluctuations. $\widetilde{W}'(\theta)$ describes the derivative of $\widetilde{W}(\theta)$ with respect to θ. The following equations describe the effect of anisotropy of surface tension.

$$\widetilde{W}(\theta) = W_\phi A(\theta) \tag{99}$$

$$\tilde{\tau}(\theta) = \tau A^2(\theta)$$

where the function $A(\theta)$ represents the effect of anisotropy of the interface width and interface kinetic time. A widely used equation for square anisotropy is given by

$$A(\theta) = 1 + \epsilon_4 \cos(4\theta) \tag{100}$$

where ϵ_4 denotes the degree of the anisotropy of the surface tension (i.e. $\epsilon_4 = 0$ describes the isotropic condition).

Re-expressing $\partial \bar{f}_{AB}^{mix}(\phi, c, T) / \partial\phi$ using the characteristics of equilibrium phase diagram of a dilute binary alloy [42],

$$\frac{1}{H}\frac{\partial \bar{f}_{AB}^{mix}(\phi,c,T)}{\partial\phi} = \bar{\lambda}\Delta c_F(e^u - 1)\tilde{g}'(\phi) \tag{101}$$

where

$$\Delta c_F = (1-k)c_0^l$$

$$\bar{\lambda} = \frac{R_g T_m}{\Omega_{\mathrm{v}} H}$$

$$u = ln\left(\frac{2c}{c_0^l[1-(1-k)\tilde{g}(\phi)]}\right)$$

A3.3.2 Solute diffusion

The variations of the solute concentration, as a conserved quantity, is controlled by the mass conservation equation

$$\frac{\partial c}{\partial t} = -\nabla.\vec{J} \tag{102}$$

$$\vec{J} = -M(\phi, c)\nabla\mu \tag{103}$$

where $\vec{J}$ denotes the flux of solute, $M(\phi, c)$ is the mobility and $\mu \equiv \delta F/\delta c$ is a generalized inter-diffusion potential. For ideal alloys, $M(\phi, c)$ is defined as

$$M(\phi, c) = D_l q(\phi, c) = D_l\left(\frac{\Omega_{\mathrm{v}}}{R_g T_m}\right) Q(\phi)c(1-c) \tag{104}$$

where D_l is the diffusivity of the liquid phase and the function $Q(\phi)$ interpolates the diffusion across the interface from the solid phase to the liquid phase. The mass conservation equation thus becomes

$$\frac{\partial c}{\partial t} = \nabla.(D_l q(\phi, c)\nabla\mu) \tag{105}$$

$$u = \frac{\Omega_{\mathrm{v}}}{R_g T_m}(\mu - \mu_E) \tag{106}$$

where $\mu_E = \mu_s^{eq} = \mu_L^{eq}$. Therefore, the mass conservation equation can be written in terms of the dimensionless chemical potential, u, as follows

$$\frac{\partial c}{\partial t} = \nabla.\left(D_l Q(\phi) c \nabla u\right) \tag{107}$$

A3.3.3 The final set of equations

The set of equations to be solved for the evolution of the order parameter and concentration fields is expresses as follow

$$\begin{gathered}\tilde{\tau}(\theta)\frac{\partial \phi}{\partial t} = \nabla.\left(\widetilde{W}^2(\theta)\nabla\phi\right) - \partial_x\left[\widetilde{W}(\theta)\widetilde{W}'(\theta)\partial_y\phi\right] + \partial_y\left[\widetilde{W}(\theta)\widetilde{W}'(\theta)\partial_x\phi\right] - \frac{\partial g(\phi)}{\partial \phi} - \\ \bar{\lambda}\Delta c_F(e^u - 1)\tilde{g}'(\phi) + \eta'(\vec{x}, t)\end{gathered} \tag{108}$$

$$\frac{\partial c}{\partial t} = \nabla.\left(D_L Q(\phi) c \nabla u\right) \tag{109}$$

$$u = ln\left(\frac{2c}{c_0^l[1-(1-k)\tilde{g}(\phi)]}\right) \tag{110}$$

A3.4 Corrections for a diffuse interface

The phase field model presented through Eqs. (108)-(110) is mathematically modified so as to closely map the dynamics of a diffuse interface model onto those of a sharp interface model [41]. In this effort several correction terms (i.e. $\Delta F, \Delta H$ and ΔJ), or so-called *anti-trapping* current, are introduced to the mass transport equations through the corresponding flux conservation and Gibbs-Thompson conditions. The final set of equations to solve for the phase and concentration fields is then expressed as below:

$$\begin{gathered}\tilde{\tau}(\theta)\frac{\partial \phi}{\partial t} = \nabla.\left(\widetilde{W}^2(\theta)\nabla\phi\right) - \partial_x\left[\widetilde{W}(\theta)\widetilde{W}'(\theta)\partial_y\phi\right] + \partial_y\left[\widetilde{W}(\theta)\widetilde{W}'(\theta)\partial_x\phi\right] - \frac{\partial g(\phi)}{\partial \phi} - \\ \bar{\lambda}\Delta c_F(e^u - 1)\tilde{g}'(\phi) + \eta'(\vec{x}, t)\end{gathered} \tag{111}$$

$$\frac{\partial c}{\partial t} = \nabla.\left(D_L Q(\phi) c \nabla u\right) + \nabla.\left(W_\phi a(\phi) U(\phi, c)\frac{\partial \phi}{\partial t}\frac{\nabla\phi}{|\nabla\phi|}\right) \tag{112}$$

$$u = ln\left(\frac{2c}{c_0^l[1+k-(1-k)h(\phi)]}\right) \tag{113}$$

In above equations the added flux source, $\vec{J}_a = W_\phi a(\phi) U(\phi, c)\frac{\partial \phi}{\partial t}\frac{\nabla\phi}{|\nabla\phi|}$, is a correction for the effects of diffuse interface. In the definition of chemical potential, $\tilde{g}(\phi)$ is replaced by $h(\phi)$ with the same limits.

Also, ϕ is rescaled to a range from -1 to 1. Therefore, a new order parameter is defined as $\phi_{new} = 2\phi_{old} - 1$ (where, $0 \leq \phi_{old} \leq 1$). So, the previous interpolation functions are modified as below:

$$g(\phi) = -\frac{\phi^2}{2} + \frac{\phi^4}{4} \tag{114}$$

$$\tilde{g}(\phi) = \frac{15}{16}\left(\phi - \frac{2\phi}{3} + \frac{\phi^5}{5}\right) \tag{115}$$

Finally, the rest of the functions are defined as

$$h(\phi) = \phi \tag{116}$$

$$Q(\phi) = \frac{(1-\phi)}{[1+k-(1-k)\phi(x)]} \tag{117}$$

$$U(\phi, c) = (1-k)c_0^l e^u \tag{118}$$

$$a(\phi) = a_t \equiv \frac{1}{2\sqrt{2}} \tag{119}$$

A3.5 Corrections for directional solidification

It is shown that Eqs. (111)-(113) can be modified for directional solidification through the following substitution [41]

$$e^u \rightarrow e^u + \frac{(z-V_p t)}{l_T}(1-k) \tag{120}$$

where $l_T = |m_l|(1-k)c_0^l/G$ is the solidification range on the phase diagram representing the thermal length of the alloy, m_l the liquidus slop, V_p the pulling speed of the sample through a thermal gradient *G,* and *z* the distance on the sample, along the direction of a fixed *G,* from a reference temperature, i.e., the temperature of steady state growth of dendrites according to the phase diagram. In this way, the additional driving force for directional solidification imposed by a moving thermal gradient, is scaled by the ratio of the distance from the location of a reference temperature and the thermal length of the alloy.

Appendix IV

A4. Numerical procedure for CA method

Following the algorithm shown in Fig. 26, the numerical scheme of the cellular automaton method consists of the solution for the heat and mass transfer equations for the entire domain, as well as the solution for the parameters associated with the SL interface such as the curvature, orientation, normal velocity, solid fraction and capturing of new cells. The numerical scheme used for each of these properties are presented as follows.

A4.1 Heat transfer

A constant temperature gradient *G* is imposed on the simulation domain which is being moved in the direction of solidification at a constant velocity V_{p}. To account for this in each time step, the imposed temperature at each cell is reduced by a value based on the solidification velocity, time interval and the gradient values as follows:

$$T_{ij}^{t+\Delta t} = T_{ij}^{t} - G.V_{\mathrm{p}}.\Delta t \tag{121}$$

A4.2 Mass transfer

The composition discontinuity at the S/L interface in the solute diffusion equation is treated by introducing a potential Π, consisting of an equivalent composition at every point throughout the domain. In other words, the entire simulation domain is treated as a single phase when dealing with the diffusion equation [32, 35, 36]. The potential Π is defined as follows:

$$\text{For the liquid phase, } \Pi = c_l \tag{122}$$

$$\text{For the solid phase, } \Pi = c_s/k \tag{123}$$

$$\text{For the interface, } \Pi = c_l^* \tag{124}$$

Therefore, Eq. (47) becomes:

$$\frac{\partial \Pi}{\partial t} = \overline{D}\left(\frac{\partial^2 \Pi}{\partial x^2}\right) + \overline{D}\left(\frac{\partial^2 \Pi}{\partial y^2}\right) \tag{125}$$

The value of $\overline{D}$ is calculated for each cell using the following procedure [32, 35, 36]: if either cell *i* or cell *i+1* which are involved in the discretization is completely solid,

$$\overline{D}_{i,i+1} = D_s \tag{126}$$

otherwise,

$$\overline{D}_{i,i+1} = \frac{f_s^i D_s + (1-f_s^i)D_l + f_s^{i+1}D_s + (1-f_s^{i+1})D_l}{2} \tag{127}$$

Central finite differences with an explicit scheme are used to discretize Eq. (125) over the entire domain, as follows:

$$\Pi_{i,j}^{t+\Delta t} = \Pi_{i,j}^{t} + \frac{\Delta t}{a^2}\left(\overline{D}_{i,i-1}\left(\Pi_{i-1,j}^{t} - \Pi_{i,j}^{t}\right) + \overline{D}_{i,i+1}\left(\Pi_{i+1,j}^{t} - \Pi_{i,j}^{t}\right) + \overline{D}_{j,j-1}\left(\Pi_{i,j-1}^{t} - \Pi_{i,j}^{t}\right) + \overline{D}_{j,j+1}\left(\Pi_{i,j+1}^{t} - \Pi_{i,j}^{t}\right)\right) \tag{128}$$

A4.3 Curvature and orientation calculation

For a two dimensional curve, the mean curvature can be defined as the magnitude of variation of unit tangent vector along the curve [36]:

$$\bar{\kappa} = \left\|\frac{\Delta\vec{T}}{\Delta s}\right\| \tag{129}$$

It can be also defined using the unit normal vector as follow:

$$\bar{\kappa} = \left\|\frac{\Delta\vec{n}}{\Delta s}\right\| \tag{130}$$

The local curvature is then defined as:

$$\bar{\kappa} = \left\|\frac{d\vec{n}}{ds}\right\| \tag{131}$$

In a CA formulation, since the solid fraction defines the contour of the SL interface, the unit normal to the interface can be represented as:

$$\vec{\mathbf{n}} = -\frac{\nabla f_s}{\|\nabla f_s\|} \tag{132}$$

The unit normal vector in 2D Cartesian coordinates can be written as:

$$\vec{\mathbf{n}} = -\left[\left(\frac{\partial f_s}{\partial x}\right)^2 + \left(\frac{\partial f_s}{\partial y}\right)^2\right]^{-0.5}\frac{\partial f_s}{\partial x}\vec{\imath} - \left[\left(\frac{\partial f_s}{\partial x}\right)^2 + \left(\frac{\partial f_s}{\partial y}\right)^2\right]^{-0.5}\frac{\partial f_s}{\partial y}\vec{\jmath} \tag{133}$$

The variation of the unit normal along the line of constant solid fraction, as schematically illustrated in Fig. 43, determines the local curvature of the SL interface. The unit tangent determines the direction of the line of constant solid fraction within the interface cell. Therefore, the variation of the unit normal along the SL interface is calculated through a directional derivative in the direction of the unit tangent. There are two possible unit tangents for the unit normal, only one of which is selected:

$$\vec{T} = T_x.\vec{\imath} + T_y.\vec{\jmath} = \left[\left(\frac{\partial f_s}{\partial x}\right)^2 + \left(\frac{\partial f_s}{\partial y}\right)^2\right]^{-0.5} \frac{\partial f_s}{\partial y}\vec{\imath} - \left[\left(\frac{\partial f_s}{\partial x}\right)^2 + \left(\frac{\partial f_s}{\partial y}\right)^2\right]^{-0.5} \frac{\partial f_s}{\partial x}\vec{\jmath} \qquad (134)$$

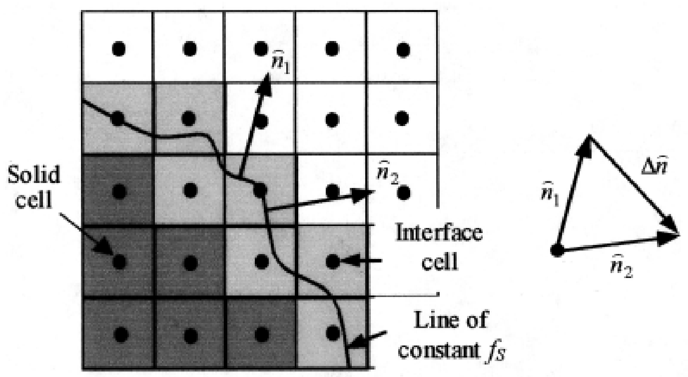

Fig. 43 Determination of curvature at the interface cell based on the variation of unit normal along the virtual SL interface defined by constant solid fractions within the cells [36].

Following the definition of directional derivative, the variation of the unit normal along the tangent can be written as follows:

$$\mathbf{D}_{\vec{T}}\vec{\mathbf{n}} = T_x \frac{\partial \vec{n}}{\partial x}\,\vec{\imath} + T_y \frac{\partial \vec{n}}{\partial y}\,\vec{\jmath} \qquad (135)$$

Therefore, the local curvature at the interface cell is expressed as:

$$\bar{\kappa} = \left\|D_{\vec{T}}\vec{n}\right\| \qquad (136)$$

The sign of the curvature is determined according to the direction of the variation of unit normal, i.e., the direction of vector $D_{\vec{T}}\vec{n}$, and the tangent. The interface is convex, i.e., with a positive curvature, if both vectors are in the same direction, and vice versa. As illustrated in Fig. 44, the sign can be assigned using the projection of the vector $D_{\vec{T}}\vec{n}$ on the unit tangent:

$$\cos\emptyset = \frac{D_{\vec{T}}\vec{n}\,.\,\vec{T}}{\|D_{\vec{T}}\vec{n}\|\,\|\vec{T}\|} \qquad (137)$$

Combining equations (136), (137) and (133), and also performing simplifications, the curvature in 2D Cartesian coordinates is expressed as:

$$\bar{\kappa} = \cos \emptyset \left\| \frac{\frac{\partial f_s}{\partial x}\left(\frac{\partial f_s}{\partial y}\right)^2 \frac{\partial^2 f_s}{\partial y \partial x} - \frac{\partial^2 f_s}{\partial x^2}\left(\frac{\partial f_s}{\partial y}\right)^3 - \left(\frac{\partial f_s}{\partial x}\right)^2 \frac{\partial f_s}{\partial y}\frac{\partial^2 f_s}{\partial y^2} + \frac{\partial f_s}{\partial x}\left(\frac{\partial f_s}{\partial y}\right)^2 \frac{\partial^2 f_s}{\partial x \partial y}}{\left[\left(\frac{\partial f_s}{\partial x}\right)^2 + \left(\frac{\partial f_s}{\partial y}\right)^2\right]^2}\vec{\imath} + \frac{\frac{\partial f_s}{\partial x}\left(\frac{\partial f_s}{\partial y}\right)^2 \frac{\partial^2 f_s}{\partial x^2} - \left(\frac{\partial f_s}{\partial x}\right)^2 \frac{\partial f_s}{\partial y}\frac{\partial^2 f_s}{\partial y \partial x} - \left(\frac{\partial f_s}{\partial x}\right)^2 \frac{\partial f_s}{\partial y}\frac{\partial^2 f_s}{\partial x \partial y} + \frac{\partial^2 f_s}{\partial y^2}\left(\frac{\partial f_s}{\partial x}\right)^3}{\left[\left(\frac{\partial f_s}{\partial x}\right)^2 + \left(\frac{\partial f_s}{\partial y}\right)^2\right]^2} \right\| \tag{138}$$

This equation takes the following simple form [37, 103, 104]:

$$\bar{\kappa} = \left[\left(\frac{\partial f_s}{\partial x}\right)^2 + \left(\frac{\partial f_s}{\partial y}\right)^2\right]^{-\frac{3}{2}} \left[2\frac{\partial f_s}{\partial x}\frac{\partial f_s}{\partial y}\frac{\partial^2 f_s}{\partial x \partial y} - \left(\frac{\partial f_s}{\partial x}\right)^2 \frac{\partial^2 f_s}{\partial y^2} - \left(\frac{\partial f_s}{\partial y}\right)^2 \frac{\partial^2 f_s}{\partial x^2}\right] \tag{139}$$

The orientation of the normal to the interface can be defined as:

$$\varphi = \cos^{-1}\left\{\left[\left(\frac{\partial f_s}{\partial x}\right)^2 + \left(\frac{\partial f_s}{\partial y}\right)^2\right]^{-0.5} \frac{\partial f_s}{\partial x}\right\} \tag{140}$$

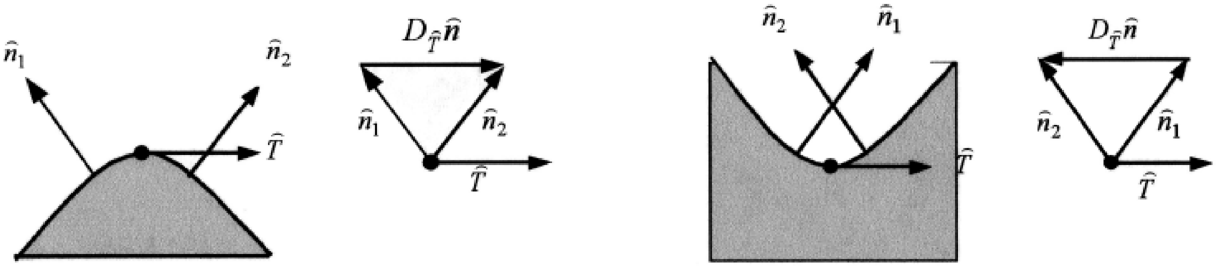

Fig. 44 Variation of the unit normal along the tangent; The one at left is the direction of the vector for Convex interface and the one at right for the concave interface [36].

<u>Numerical solution for equations (139) and (140):</u>

A second order centered finite difference scheme is used to discretize equations (139) and (140) over the solution domain, i.e.,

$$\left.\frac{\partial f_s}{\partial x}\right|_I^{i,j} = \frac{-f_s^{i+2,j} + 8f_s^{i+1,j} - 8f_s^{i-1,j} + f_s^{i-2,j}}{12a} \tag{141}$$

$$\left.\frac{\partial f_s}{\partial y}\right|_I^{i,j} = \frac{-f_s^{i,j+2} + 8f_s^{i,j+1} - 8f_s^{i,j-1} + f_s^{i,j-2}}{12a} \tag{142}$$

$$\left.\frac{\partial^2 f_s}{\partial x^2}\right|_I^{i,j} = \frac{-f_s^{i+2,j} + 16f_s^{i+1,j} - 30f_s^{i,j} + 16f_s^{i-1,j} - f_s^{i-2,j}}{12a^2} \tag{143}$$

$$\left.\frac{\partial^2 f_s}{\partial y^2}\right|_I^{i,j} = \frac{-f_s^{i,j+2} + 16f_s^{i,j+1} - 30f_s^{i,j} + 16f_s^{i,j-1} - f_s^{i,j-2}}{12a^2} \tag{144}$$

The term $\frac{\partial^2 f_s}{\partial x \partial y}$ at the interface cell is approximated using equations (141) and (142):

$$\frac{\begin{array}{c} f_s^{i+2,j+2} - 8f_s^{i+1,j+2} + 8f_s^{i-1,j+2} - f_s^{i-2,j+2} - 8f_s^{i+2,j+1} + 64\, f_s^{i+1,j+1} - 64\, f_s^{i-1,j+1} + 8f_s^{i-2,j+1} + \\ 8f_s^{i+2,j-1} - 64f_s^{i+1,j-1} + 64f_s^{i-1,j-1} - 8f_s^{i-2,j-1} - f_s^{i+2,j-2} + 8f_s^{i+1,j-2} - 8f_s^{i-1,j-2} + f_s^{i-2,j-2} \end{array}}{144a^2} \tag{145}$$

A4.4 Interface velocity

The solute balance at the interface can be expressed as follows:

$$V_n c_l^*(1-k) = \left[-D_l \frac{\partial c_l}{\partial \vec{\mathbf{n}}} \Big|_{\text{interface}} + D_s \frac{\partial c_s}{\partial \vec{\mathbf{n}}} \Big|_{\text{interface}}\right] \tag{146}$$

The derivative of composition with respect to the unit normal is equivalent to its directional derivative in the direction of the normal:

$$\frac{\partial c_i}{\partial \vec{\mathbf{n}}} = D_{\vec{\mathbf{n}}} c_i \tag{147}$$

Therefore, the normal velocity can be written as:

$$V_n = \frac{1}{c_l^*(1-k)}\left[-D_l(D_{\vec{\mathbf{n}}} c_l) \Big|_{\text{interface}} + D_s(D_{\vec{\mathbf{n}}} c_s) \Big|_{\text{interface}}\right] \tag{148}$$

The directional derivative can then be obtained by projection of the vector of composition variation on the unit normal:

$$D_{\vec{\mathbf{n}}} c_i = \vec{\mathbf{n}}.\nabla c_i \tag{149}$$

$$\nabla c_i = \frac{\partial c_i}{\partial \mathrm{x}}\vec{\mathbf{i}} + \frac{\partial c_i}{\partial \mathrm{y}}\vec{\mathbf{j}} \tag{150}$$

Therefore, combining equations (133), (149) and (150) [37]:

$$D_{\vec{\mathbf{n}}} c_i = \frac{\partial c_i}{\partial \mathrm{x}}\cos\varphi + \frac{\partial c_i}{\partial \mathrm{y}}\sin\varphi \tag{151}$$

$$V_n = \frac{1}{c_l^*(1-k)}\left[-D_l\left(\frac{\partial c_l}{\partial x}\cos\varphi + \frac{\partial c_l}{\partial y}\sin\varphi\right) + D_s\left(\frac{\partial c_s}{\partial x}\cos\varphi + \frac{\partial c_s}{\partial y}\sin\varphi\right)\right] \tag{152}$$

where,

$$\cos\varphi = \left|\left[\left(\frac{\partial f_s}{\partial x}\right)^2 + \left(\frac{\partial f_s}{\partial y}\right)^2\right]^{-0.5} \frac{\partial f_s}{\partial x}\right| \tag{153}$$

$$\sin\varphi = \left|\left[\left(\frac{\partial f_s}{\partial x}\right)^2 + \left(\frac{\partial f_s}{\partial y}\right)^2\right]^{-0.5} \frac{\partial f_s}{\partial y}\right| \tag{154}$$

The interface velocity in *x* and *y* directions can be obtained as follows:

$$V_x = \frac{1}{c_l^*(1-k)}\left[-D_l \frac{\partial c_l}{\partial x}\Big|_{\text{interface}} + D_s \frac{\partial c_s}{\partial x}\Big|_{\text{interface}}\right] \tag{155}$$

$$V_y = \frac{1}{c_l^*(1-k)}\left[-D_l \frac{\partial c_l}{\partial y}\Big|_{\text{interface}} + D_s \frac{\partial c_s}{\partial y}\Big|_{\text{interface}}\right] \tag{156}$$

<u>Numerical solution for derivatives of composition:</u>

The following expressions are obtained through discretization with forward and backward differences of second-order accuracy with respect to the interface cell [36]:

$$\frac{\partial c_l}{\partial x}\Big|_{\text{interface (right−hand side)}} = \frac{c_l(i+2,j)-c_l^*(i,j)}{2a} + \frac{c_l(i+1,j)-c_l^*(i,j)}{a} - \frac{c_l(i+2,j)-c_l(i+1,j)}{a} \tag{157}$$

$$\frac{\partial c_l}{\partial x}\Big|_{\text{interface (left−hand side)}} = \frac{c_l(i-2,j)-c_l^*(i,j)}{2a} + \frac{c_l(i-1,j)-c_l^*(i,j)}{a} - \frac{c_l(i-2,j)-c_l(i-1,j)}{a} \tag{158}$$

$$\begin{aligned}\frac{\partial c_l}{\partial x}\Big|_{\text{interface}} &= \frac{\partial c_l}{\partial x}\Big|_{\text{interface (right−hand side)}}.F\big(f_l(i+1,j), f_l(i+2,j)\big)\\ &\quad + \frac{\partial c_l}{\partial x}\Big|_{\text{interface (left−hand side)}}.F\big(f_l(i-1,j), f_l(i-2,j)\big)\end{aligned} \tag{159}$$

Therefore,

$$\begin{aligned}\frac{\partial c_l}{\partial x}\Big|_{\text{interface}} &= \left(\frac{-3c_l^*(i,j) + 4c_l(i+1,j) - c_l(i+2,j)}{2a}\right).F\big(f_l(i+1,j), f_l(i+2,j)\big)\\ &\quad + \left(\frac{-3c_l^*(i,j) + 4c_l(i-1,j) - c_l(i-2,j)}{2a}\right).F\big(f_l(i-1,j), f_l(i-2,j)\big)\end{aligned} \tag{160}$$

$$\begin{aligned}\frac{\partial c_s}{\partial x}\Big|_{\text{interface}} &= \left(\frac{-c_s^*(i,j) + 4c_s(i+1,j) - c_s(i+2,j)}{2a}\right).F\big(f_s(i+1,j), f_s(i+2,j)\big)\\ &\quad + \left(\frac{-3c_s^*(i,j) + 4c_s(i-1,j) - c_s(i-2,j)}{2a}\right).F\big(f_s(i-1,j), f_s(i-2,j)\big)\end{aligned}$$

(161)

In the discretization scheme, it is vital to account for the presence of the gradient in the derivative direction. The function $F(f_1, f_2)$ is then used to determine on which side of the interface the relevant gradient (i.e. the solid or liquid) exists. The function output is 0 if either f_1 or f_2 is 0. In any other cases, it returns a value of 1. Similar expressions may be written for the y component of the gradients. The equilibrium liquid composition at the interface cell, $c_l^*(i,j)$, is calculated using Eq. (49) in which the temperature is obtained from the imposed thermal field. The equilibrium solid composition is calculated based on Eq. (54) as follow:

$$c_s^*(i,j) = kc_l^*(i,j) \tag{162}$$

A4.5 Solid fraction increment

Assuming the interface with motions in x and y directions as a planar front is not physically true and imposes overestimation in calculation of the actual solid fraction. Since the interface velocity is estimated based on the mass balance, and also taking into account that the solute balance is valid only at the limit of the vanishing thickness of the SL interface, the only realistic velocity that can be calculated in this way is not the components but the normal velocity. Thus, the solid fraction increment is calculated based on the motion along the normal to the SL interface, as illustrated in Fig. 45, [37]:

$$\Delta f_s = \frac{V_n \Delta t}{L_\varphi}(1 + \eta(1 - 2p)) \tag{163}$$

L_φ represents the distance to be traveled by a point on the interface along the normal so that one cell becomes completely solid. According to Fig. 45, this length is to be normalized with the interface normal direction so as to minimize the effect of the mesh anisotropy on the solid fraction increment. The following expression is then used in the numerical procedure:

$$L_\varphi = \sqrt{2}\,\mathrm{a} \,.\cos\left|\frac{\pi}{4} - \varphi\right| \tag{164}$$

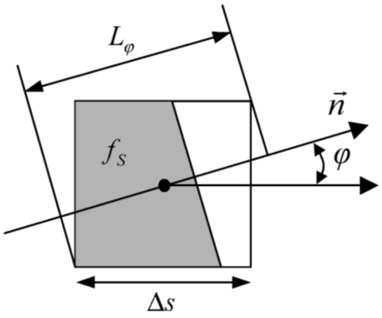

Fig. 45 Estimation of solid fraction increment by the motion of flat interface along the normal [37].

A4.6 Virtual interface tracking

Proposed by Sanchez and Stefanescu [37], virtual interface tracking is the most efficient method of cell capturing in CA simulations which significantly reduces the artificial mesh anisotropy. In this method, each interface cell introduces a virtual location representing a point on the sharp S/L interface. As illustrated in Fig. 46 (a), the location of each interface point is determined by a line drawn from the cell center along the interface normal with the length $L_{\varphi} \times f_s$. The virtual interface is found by interpolation between the interface points, as schematically drawn in Fig. 46 (b). After obtaining the new solid fraction values at each time step, the liquid cells are scanned and those with centers lying inside the area surrounded by the sharp S/L interface will be captured. The neighbourhood of the newly captured interface cells shall also comply with the condition that at least one of their eight closest neighbouring cells is solid [58]. Using the same approach, another way of capturing new interface cells is represented by Michellic et al [59] which is simpler for numerical implementation. As shown in Fig. 47, the liquid cell can be captured if its center falls within the defined triangle between two neighbouring interface points and either cell centers.

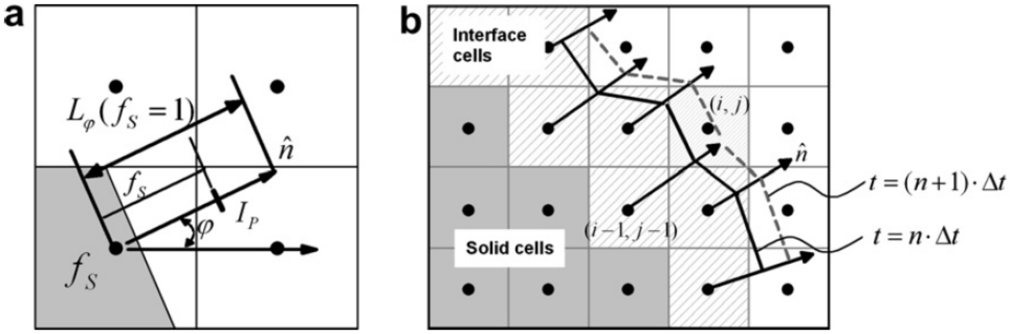

Fig. 46 Illustration of (a) the determination of the position of sharp S/L interface points, and (b) capturing method for liquid cells [58].

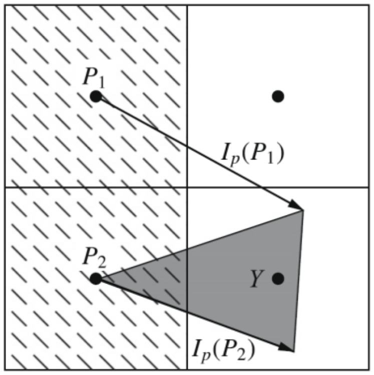

Fig. 47 Virtual front-tracking scheme [59].

It should be noted that, using virtual interface tracking method, the solid fraction increment calculated for each interface cell has to be spread among all interface cells in the neighbourhood to avoid numerical instability in the solution of the diffusion field around the interface and the subsequent calculation of interface velocity. This is done through application of the transition rules and rejection of solute at the end of each time step.

A4.7 Transition rules and solute rejection

After calculation of the solid fraction increment for the captured interface cells, a simple set of transition rules are applied in order to update the solid fraction of interface cells during a time step. This is done in a way to maintain continuity in the solid and liquid at the interface. Accordingly, after time step Δt, the following criteria applies for each interface cell:

- If $f_{i,j}^{t} + \Delta f_{i,j}^{t+\Delta t} \geq 1$, then $f_{i,j}^{t+\Delta t}$ is set to 1.
- If $f_{i,j}^{t} + \Delta f_{i,j}^{t+\Delta t} \leq 0$, then $f_{i,j}^{t+\Delta t}$ is set to 0.
- Otherwise, $f_{i,j}^{t+\Delta t} = f_{i,j}^{t} + \Delta f_{i,j}^{t+\Delta t}$

where $f_{i,j}^{t}$ is the solid fraction of the interface cell (i,j) at time t, $f_{i,j}^{t+\Delta t}$ is the solid fraction of the interface cell (i,j) at time $t+\Delta t$ and $\Delta f_{i,j}^{t+\Delta t}$ is the calculated solid fraction increment in the interface cell (i,j) at time $t+\Delta t$.

Having set the solid fraction value at time $t+\Delta t$, the solute shall be rejected from the solid into the remaining liquid, so the overall composition is kept constant in each individual interface cell. The new liquid composition (or the new potential value) at the interface cell is then calculated as follows:

$$\Pi_{i,j}^{t+\Delta t} = \Pi_{i,j}^{t} + \Pi_{i,j}^{t}(1-k)(f_{i,j}^{t+\Delta t} - f_{i,j}^{t}) \tag{165}$$

The following modifications must be taken into consideration once the new potential value is obtained for each interface cell:

- If $f_{i,j}^{t} = 1$ & $f_{i,j}^{t+\Delta t} < 1$, then $\Pi_{i,j}^{t+\Delta t} = \Pi_{i,j}^{t+\Delta t}/k$
- If $f_{i,j}^{t} < 1$ & $f_{i,j}^{t+\Delta t} = 1$, then $\Pi_{i,j}^{t+\Delta t} = \Pi_{i,j}^{t+\Delta t} * k$